

**Exciton polaritons in semiconductor
microcavities: from polariton
condensation in magnetic field to Bloch
oscillations in modulated structures**



Magdalena Durska
Department of Physics and Astronomy
University of Sheffield

Thesis submitted for the degree of
Doctor of Philosophy
February 2015

Abstract

This work concerns experimental investigation of the microcavity polaritons in GaAs based structures.

First, the growth-related in-plane disorder present in the microcavity samples is studied. This disorder occurs naturally due to the lattice mismatch between components and results in strain relaxation, which strongly modifies polaritons propagation. In this work we demonstrate that reducing content of aluminium in distributed Bragg reflectors and reducing indium content in the quantum wells leads to suppression of strain relaxation.

The next part of this thesis is focused on studying magnetophotoluminescence spectra from a GaAs microcavity. The experimental results show that the magnitude of the Zeeman splitting depends on the polariton density, and it is suppressed above the threshold for parametric oscillation. The experimental results are explained in terms of the phase synchronization of spin-up and spin-down polarized polariton condensates, resulting from a nonlinear coupling via the coherent pump state.

Finally, polaritons confined into one-dimensional system are investigated. Photoluminescence spectra from modulated wires with energy gradient introduced either by lateral change of the width or by the excitonic reservoir are studied. The experimental results show that Bloch oscillations can be observed in 1D polaritonic structures, as well as Wannier-Stark ladder and Landau-Zener tunnelling. A theoretical model allowing calculating the trajectories of polaritons in studied structures is also proposed.

Acknowledgements

First and foremost, I owe my deepest gratitude to my supervisor Dr. Dmitry Krizhanovskii for giving me the unique opportunity to study for my PhD at Sheffield and for his support and guidance throughout the entire process.

I would also like to thank the head of the LDS group, Prof. Maurice Skolnick, whose dedication to research and caring attitude are inspiring.

I am also thankful to Dr. Paul Walker and Dr. Dipankar Sarkar for introducing me to the lab and for their assistance. My thanks also go to Kuru and Lloyd - my experimental colleagues whom I have worked with on several projects and to Romain for valuable discussions over coffee.

I express my sincere thanks to Prof. Jacqueline Bloch from LPN-CNRS for hosting and supervising me during my PhD secondment and to Dimitrii Tanese for his help and fruitful collaboration in the lab.

I would like to take this opportunity to thank my viva examiners - Dr. Paulo Santos and Dr. Grzegorz Sęk, for their very helpful comments and suggestions.

I would also like to thank administrative and technical staff for dealing with my queries in a fast and efficient way.

I owe my thanks to all my fellow PhD students and everyone in the LDS group who contributed to the progress of my studies.

I gratefully acknowledge the funding towards my PhD from the EU under the Marie Skłodowska-Curie initial training network FP7 “Clermont4” (235114).

Finally, I would like to thank my family and friends for being supportive, motivating and for believing in me, no matter the distance.

Magdalena Durska



List of Publications

"Suppression of Zeeman splitting of the energy levels of exciton-polariton condensates in semiconductor microcavities in an external magnetic field", P. Walker, T.C.H. Liew, D. Sarkar, M. Durska, A.P.D. Love, M.S. Skolnick, J.S. Roberts, I.A. Shelykh, A.V. Kavokin, and D.N. Krizhanovskii, Phys. Rev. Lett, 106, 257401 (2011)

"Spontaneous vortices in optically shaped potential profiles in semiconductor microcavities", K. Guda, M. Sich, D. Sarkar, P. M. Walker, M. Durska, R. A. Bradley, D. M. Whittaker, M. S. Skolnick, E. A. Cerda-Méndez, P. V. Santos, K. Biermann, R. Hey, D. N. Krizhanovskii, Phys. Rev. B, 87, 081309R (2013)

"Optical microscopy with super-resolution by liquid-immersed high-index microspheres", A. Darafsheh, N.I. Limberopoulos, J.S. Derov, D.E. Walker Jr., M. Durska, D.N. Krizhanovskii, D.M. Whittaker, and V.N. Astratov, Proc. of SPIE, Vol. 8594, 85940C (2013)

"Exciton polaritons in semiconductor waveguides", P. M. Walker, L. Tinkler, M. Durska, D. M. Whittaker, I. J. Luxmoore, B. Royall, D. N. Krizhanovskii, M. S. Skolnick, I. Farrer, D. A. Ritchie, Appl. Phys. Lett., 102, 012109 (2013)

"Design and characterization of high optical quality InGaAs/GaAs/AlGaAs-based polariton microcavities", L. Tinkler, P. M. Walker, E. Clarke, D. N. Krizhanovskii, F. Bastiman, M. Durska, M. S. Skolnick, Appl. Phys. Lett., 106, 021109 (2015)



Contents

Abstract	i
Acknowledgements	iii
List of Publications	v
List of Figures	xii
List of Tables	xiii
1 Introduction	1
2 Background	3
2.1 Quantum well excitons	3
2.2 Microcavities	5
2.2.1 Distributed Bragg reflectors (DBRs)	8
2.2.2 Cavity	10
2.3 Microcavity polaritons	12
2.3.1 Eigenenergies and dispersion of polariton states	16
2.3.2 Polariton dispersion	19
2.4 Bose-Einstein Condensation	22
2.4.1 Equilibrium BEC	22
2.4.2 Non-equilibrium BEC - modern approach	27
2.4.3 Observation of Bose-Einstein condensate	30
2.5 Non-equilibrium condensate of polaritons	32
2.5.1 Non-resonant and resonant (OPO) polariton condensate excitation	33
2.5.2 Superfluidity	39
2.5.3 Vortices and Solitons	41

2.6	Confining polaritons in 0D and 1D systems	45
3	Experimental techniques	53
3.1	Imaging	55
3.1.1	Real space imaging	56
3.1.2	k-space imaging	56
3.2	Time resolved measurements	57
4	Suppression of cross-hatching disorder in GaAs/AlAs microcavities	59
4.1	Background	59
4.1.1	Impact of microcavity QWs on the disorder phenomenon	66
4.1.2	Disorder in polaritonic systems	67
4.2	Experiment	70
4.2.1	AlAs/GaAs microcavity structures	70
4.2.2	AlGaAs/GaAs microcavity structures with reduced aluminium content	74
4.3	Conclusions	78
5	Suppression of Zeeman splitting in non-equilibrium polariton condensate	79
5.1	Background	79
5.1.1	Spin Meissner effect in equilibrium BEC of polaritons	80
5.2	Experiment	83
5.2.1	Sample structure and experimental setup	83
5.2.2	Magnetophotoluminescence spectra in OPO configuration	84
5.3	Theoretical model	86
5.4	Conclusions	90
6	Bloch oscillations of microcavity polaritons	93
6.1	Background	93
6.1.1	Wannier-Stark ladder	100
6.1.2	Landau-Zener tunnelling	101
6.1.3	Bloch oscillations in different systems	102
6.2	Structures	107
6.2.1	Wannier-Stark ladder	109
6.3	Observation of the polariton Bloch oscillations	111
6.3.1	Bloch oscillations in systems with varying potential period	115
6.3.2	Landau-Zener tunnelling	117

6.4 Conclusions	118
Summary	121
Bibliography	123

List of Figures

2.1.1 Energy states of a Wannier exciton	5
2.2.1 Schematic structures of optical microcavities.	8
2.2.2 Schematic diagram of a microcavity with three quantum wells	11
2.3.1 Strong coupling reflection spectra	15
2.3.2 Phase diagram of GaAs based microcavities	17
2.3.3 Dispersions of exciton-polaritons for different detunings and corresponding Hopfield coefficients.	20
2.4.1 Condensate fraction	25
2.4.2 Bogoliubov dispersion of elementary excitations in He	30
2.4.3 Bose-Einstein condensation of ^{87}Rb atoms and photons	31
2.5.1 Bose-Einstein condensate of polaritons	33
2.5.2 Scheme of the non-resonant and resonant polariton excitation	35
2.5.3 Optical bistability in strongly coupled microcavities	38
2.5.4 Bogoliubov dispersion of elementary excitations in exciton-polaritons	40
2.5.5 Formation of vortices	43
2.5.6 Formation of dark and bright solitons	45
2.6.1 Polaritons confinement using SAW	47
2.6.2 Spatial trapping of polaritons in microcavities with cavity layer mesa pattern	48
2.6.3 1D polariton condensate in a microwire	50
2.6.4 0D polariton condensate in a micropillar	51
3.1.1 Imaging of real and k-space	57
3.2.1 Scheme of the streak camera	58
4.1.1 Scheme of the GaAs, AlAs and AlGaAs cubic cells	61
4.1.2 Scheme of the geometry of a 60° dislocation	63

4.1.3 RRS ring from GaAs/AlAs disordered sample	68
4.2.1 Nomarski microscope images of the strain relaxed samples	72
4.2.2 Resonant transmission images from samples with photonic potential disorder	73
4.2.3 Nomarski microscope surface imaging of the $Al_{0.85}Ga_{0.15}As/GaAs$ samples .	76
4.2.4 OPO condensate images of relaxed and unrelaxed microcavities	77
5.1.1 Polarization of optical transitions in zinc-blend semiconductor quantum wells	80
5.1.2 Phase diagram of a gas of interacting exciton-polaritons	81
5.2.1 Spectra of polariton emission at $k \sim 0$ in two circular polarizations	85
5.2.2 Dependences of Zeeman splitting on pump power	86
5.3.1 Time dependence of the relative phase for $\sigma-$ and $\sigma+$ polarized signal com- ponents	89
6.1.1 Bloch oscillations - dependence on the width of momentum distribution . . .	99
6.1.2 Wannier-Stark ladder and Landau-Zener tunnelling	102
6.1.3 Bloch oscillations of polaritons - theoretical results	106
6.2.1 Microwire polariton structures for the Bloch oscillations studies	108
6.2.2 Emissions from the Bloch oscillator structures	110
6.3.1 Real space propagation of non-resonantly excited polaritons along the wire .	112
6.3.2 Bloch oscillations in the modulated wire $P = 2.7\mu m$	113
6.3.3 Analysis of the Bloch oscillations parameters	116
6.3.4 Bloch oscillations in the modulated wire $P = 2.1\mu m$	117
6.3.5 Landau-Zener tunnelling	118

List of Tables

4.1	Lattice constants and thermal expansion coefficients of studied semiconductors	61
4.2	Cross-hatching suppression experiment structures	77

Chapter 1

Introduction

Semiconductor microcavity exciton-polaritons are half-light half-matter composite quasiparticles, arising due to the strong coupling between photons and excitons. Since 1992, when they were experimentally observed for the first time by Weisbuch et al. [1], they have been centre of attraction for many researchers. Over the past 20 years a huge development has been achieved in the field of microcavity exciton-polaritons, both in theory and in experiment. A rich physics of these particles has been explored, including condensation of polaritons [2], superfluidity [3], presence of vortices [4] and solitons [5] or optical parametric oscillation (OPO) [6, 7, 8].

The aim of this thesis is twofold. First, we investigate a growth-related disorder in microcavity samples and propose a way to suppress it. Then, we explore two physical phenomena: the Zeeman splitting in planar microcavity and Bloch oscillations in microcavity wires.

The second chapter introduces the basic concepts of semiconductor microcavity physics, relevant to the studies presented in this thesis. It describes the microcavity structure and explains how and when exciton-polaritons do form. A short introduction to Bose-Einstein condensation is given and the difference between ideal equilibrium BEC and non-equilibrium polariton condensate is explained. Different methods of producing polariton condensate through either resonant (OPO) or non-resonant excitation are presented and basics of the superfluidity and phenomenon are briefly described. Finally, concepts of confining microcavity polaritons in 0D and 1D systems are given.

The third chapter describes experimental techniques used for optical measurements. This includes imaging of the real and momentum space luminescence signals and their evolution in time.

In chapter 4 experiments on GaAs/AlAs microcavities with low in-plane disorder are described. The samples grown with varying parameters are studied via optical measurements. We show that reducing aluminium content in DBR mirrors and reducing indium content in the quantum wells leads to the suppression of strain relaxation.

[Published in Appl.Phys.Lett. 106, 021109 (2015) [9]]

In chapter 5 we study the magnetophotoluminescence spectra of a semiconductor microcavity in the optical parametric oscillation (OPO) configuration. We show that the Zeeman splitting depends on the polariton density and that above the threshold for parametric oscillation the Zeeman splitting is fully quenched. In this chapter theoretical explanation of the Zeeman splitting suppression is also presented. Proposed model was developed by A.V. Kavokin and T.C.H. Liew and is based on the phase synchronization of spin-up and spin-down polarized polariton condensates.

[Published in Phys. Rev. Lett., 106, 257401 (2011) [10]]

Chapter 6 describes the experiment that was conducted in Laboratoire de Photonique et de Nanostructures (LPN) CNRS in Marcoussis (France) under supervision of Jacqueline Bloch. All the data presented in this chapter were measured, analysed and discussed with Dimitrii Tanese. In this chapter we investigate photoluminescence from the 1D modulated polaritonic structures, expected to reveal Bloch oscillations. We observe Wannier-Stark ladder, Bloch oscillations and Landau-Zener tunnelling. Moreover, we propose a theoretical model allowing calculating the trajectories of polaritons in studied structures.

Chapter 2

Background

2.1 Quantum well excitons

Absorption of light in semiconductors gives a rise to creation of free electron and a hole. Due to the Coulomb interaction they form a quasiparticle, similar to the hydrogen atom, called exciton. Excitonic photoemission lines were first observed by A. Kronenberger and P. Pringsheim [11] and I. Obreimov and W. de Haas [12] in late 1920s and then interpreted and named by Frenkel [13, 14] few years later. The size of the excitons varies from angstrom up to hundreds of angstroms and by this reason, the excitons can be studied in two limiting cases: Frenkel excitons, with binding energy being typically of the order of 100-300 meV, and Wannier-Mott [15, 16] excitons, discovered at the end of 1930s, with binding energy of the order of few meV. Whereas the Frenkel excitons are localized to a single lattice site, the latter, which are typical for most semiconductors, span many lattice sites due to the screening of Coulomb interaction by the electrons in the valence band via the large dielectric constant [17].

It is easier to think about the system by decomposing the exciton motion into two parts: a centre-of-mass (CM) motion and a relative electron-hole motion in the exciton.

For isotropic and parabolic conduction and valence bands, with extrema in the middle of the Brillouin zone, energy dispersion is given by:

$$\begin{aligned} E_e(k_e) &= E_g + \frac{\hbar^2 k_e^2}{2m_e} \\ E_h(k_h) &= \frac{\hbar^2 k_h^2}{2m_h} \end{aligned} \quad (2.1.1)$$

for electrons and holes respectively, where E_g is the bandgap and m_e (m_h) is effective mass of electron (hole).

The binding energy of the ground exciton state is:

$$E_B = \frac{\mu e^4}{2\hbar^2(4\pi\epsilon\epsilon_0)^2} \quad (2.1.2)$$

where μ is the reduced mass, ϵ is a dielectric constant and ϵ_0 is the zero-frequency dielectric constant.

Similarly to the hydrogen atom, the exciton has a series of excited states above the ground state. Due to the small effective mass and large dielectric permittivity ($\epsilon > 10$) for majority of bulk inorganic semiconductors, exciton binding energies are much smaller than kT at room temperature and thus excitons exist only at low temperatures. In nanostructures, due to space limits, electrons and holes in excitons are bounded much stronger than in case of bulk semiconductors, which results in much smaller size of excitons. Smaller size of excitons is accompanied by higher energy of the binding; hence exciton phenomena are much stronger in nanostructures than in bulk semiconductors. For the excitons in two-dimensional systems, such as quantum wells, the binding energy is four times higher than in case of bulk semiconductors [18].

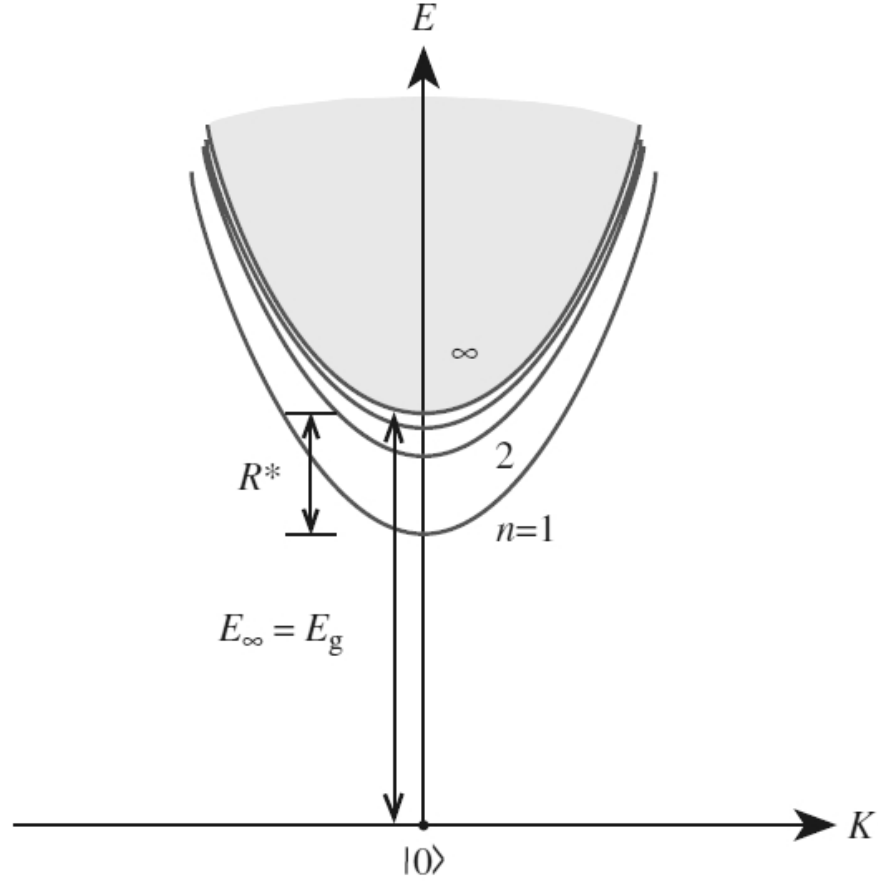


Figure 2.1.1: Energy states of a Wannier exciton, showing its bound states $n=1$ to 3 as well as the continuum states (source: [17]).

2.2 Microcavities

An optical cavity is a system consisting of optical elements aligned in the way that the light can be confined through a resonant circulation between two mirrors. It can be designed for different ranges of wavelengths, depending on the purpose. In this thesis we are interested in optical cavities, where the optical distance between two mirrors is of the order of light wavelength, called microcavities. In microcavities light is confined to very small volumes, which gives rise to quantum effects that can be observed, like strong coupling between light and matter, control of spontaneous emission and enhancement of spontaneous emission due to Purcell effect [19, 20], and has a wide range

of applications in optoelectronics. Depending on the method of confinement, optical microcavities can be categorized into one of the following types:

- Fabry-Perot microcavities
- whispering gallery microcavities
- photonic crystal microcavities

In Fabry-Perot microcavities confinement is obtained via recirculation of light between two highly reflective mirrors. Confinement in whispering gallery microcavities relies on the total internal reflection in disk made of material with a high refractive index or spherical structures surrounded by material with a low refractive index. Finally, in photonic crystals it is based on employment of periodic patterning, which results in confining the light to a small volume around a defect in a photonic lattice [21, 22]. There are two critical parameters, characterizing a microcavity structure: quality factor (or finesse) and volume of the mode. The quality factor (Q-factor) measures the efficiency of trapping the light inside the cavity - the higher the quality factor is, the longer photons stay in the cavity. It is defined as:

$$Q = 2\pi \frac{\text{stored energy}}{\text{energy loss per optical cycle}} \quad (2.2.1)$$

Since the energy density $u(t)$, assuming a Lorentzian distribution, can be written as:

$$u(t) \propto e^{-2\Gamma t} \quad (2.2.2)$$

the energy loss is given by:

$$-\frac{du(t)}{dt} \propto -2\Gamma e^{-2\Gamma t} \quad (2.2.3)$$

where Γ is the decay rate and it is equal to half of the cavity mode linewidth at half maximum (FWHM) $\delta\omega$ ($\Gamma = \frac{\delta\omega}{2}$), and optical period is given by:

$$T = \frac{2\pi}{\omega_0} \quad (2.2.4)$$

where ω_0 is a resonant cavity frequency. The quality factor can be then written in terms of frequencies:

$$Q = \frac{\omega_0}{2\Gamma} = \frac{\omega_0}{\delta\omega} \quad (2.2.5)$$

Finesse F is quite similar to quality factor, except that instead of time of optical cycle T , the time of a round trip t_r is considered, which is given by:

$$t_r = T \frac{\lambda_0}{\Delta\lambda} \quad (2.2.6)$$

where $\Delta\lambda$ ($\Delta\omega$) is a measure of free spatial range, defining the wavelength (frequency) spacing between adjacent resonances, hence:

$$F = 2\pi \frac{\text{stored energy}}{\text{energy loss per round trip}} = \frac{\Delta\omega}{\delta\omega} = Q \frac{T}{t_r} \quad (2.2.7)$$

The second characteristic measure of microcavities is mode volume V , which defines the volume occupied by the optical mode - the smaller mode volume is, the stronger the spatial confinement.

In case of 3D microcavities, most desirable are microcavities with a high quality factor and very low mode volume, where the light is confined to dimensions of the order of microcavity wavelength - with a high value of Q/V ratio. Maximising the Q/V ratio in such microcavities is required to observe Purcell effect or strong coupling between a single emitter (for example quantum dot or impurity) and a cavity mode, which may lead to many applications inter alia in quantum information processing, micro lasers or optical filters [23, 24, 25, 26]. The schematic structures as well as values of characteristic quantities: Q-factor and volume V are presented in figure 2.2.1. In case of planar microcavities, which we study in this thesis, photons may freely propagate in the plane of the cavity and this implies that the mode volume is large. However, since we are looking at 2D excitons and 2D photons, they can interact with each other, forming polaritons. In planar microcavities it is thus not the mode volume, but the

spacing between the mirrors which plays the role in coupling 2D excitons with 2D cavity photons.

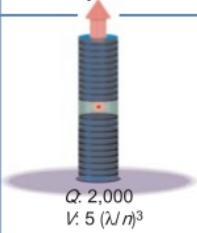
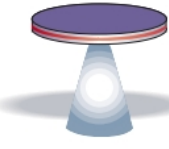
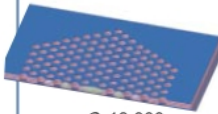
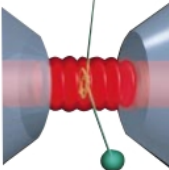
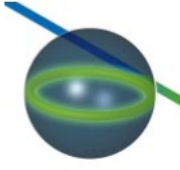
	Fabry-Perot	Whispering gallery	Photonic crystal
High Q	 $Q: 2,000$ $V: 5 (\lambda/n)^3$	 $Q: 12,000$ $V: 6 (\lambda/n)^3$	 $Q_{III-V}: 7,000$ $Q_{Poly}: 1.3 \times 10^5$
Ultrahigh Q	 $F: 4.8 \times 10^5$ $V: 1,690 \mu\text{m}^3$	 $Q: 8 \times 10^9$ $V: 3,000 \mu\text{m}^3$	 $Q: 10^8$

Figure 2.2.1: Schematic structures of optical microcavities arranged by the type of the microcavity and achievable Q factors. Values of mode volume V and Q -factor or finesse F achieved for presented microcavities are indicated below each image (source: [21]).

2.2.1 Distributed Bragg reflectors (DBRs)

Fabry – Perot (FP) cavity is one of the optical resonators, consisting of two plane mirrors separated by a dielectric layer, forming a sort of optical trap. The mirrors should be highly reflective and in semiconductor microcavities are present in the form of distributed Bragg reflectors (DBRs). Contrary to metallic mirrors, they consist of only non-absorbing dielectric materials and as the name suggests, in distributed Bragg reflectors the reflectivity is distributed over many interfaces. In this thesis we study 2D planar optical microcavities, where the light is trapped in only one dimension. They can be designed to have very high reflectivity at a chosen wavelength range, which can be obtained by careful selection of the materials and the thickness of the layers.

The most common DBR is a periodic structure formed by multiple layers of alternating high and low indices materials, designed to be of optical thickness $\lambda/4$, where $\lambda = \lambda_{vacuum}/n$ is the wavelength in the layer material, n is the refractive index of the material. The flat maximum reflection, called the photonic stop-band corresponds to a situation when the, so called, Bragg condition is fulfilled - optical thicknesses of the layers are equal to a quarter of the Bragg wavelength λ_0 :

$$\lambda_0/4 = d_L n_L = d_H n_H \quad (2.2.8)$$

where d_L (d_H) and n_L (n_H) are thickness and refractive index of low (high) refractive index layer. If the condition 2.2.8 is satisfied, then the partial reflection at the interface of wave traveling from material with high refractive index to material with low refractive index leads to a π phase shift. Due to the path difference, the wave reflected at each interface experiences additional phase change, resulting in constructive interference of reflected light. Reflectivity of the DBR in the stop-band is approximately constant and depends on the refractive indices of the layers, as well as on the number of pairs of layers and is defined as [27]:

$$R = 1 - 4 \frac{n_{ext}}{n_c} \left(\frac{n_L}{n_H} \right)^{2N} \quad (2.2.9)$$

where N is the number of pairs of layers, and n_{ext} , n_c , n_L and n_H are refractive indices of external medium, cavity material and low and high-index layers respectively. The bandwidth as N approaches infinity is given by:

$$\Delta\lambda = \frac{4\lambda_B}{\pi} \arcsin \left(\frac{n_2 - n_1}{n_2 + n_1} \right) \quad (2.2.10)$$

It can be easily seen from eq. 2.2.9 that enhancing the reflectivity can be obtained either by increasing number of pairs of layers or by choosing materials with higher index contrast. This equation also shows, that from a theoretical point of view, it is not possible to achieve structure with 100% reflectivity us-

ing a finite number of layers - it is, however, possible to fabricate mirrors with $R > 99\%$, considered as a very good result. The actual value of the reflectivity is lower than the one obtained from eq. 2.2.9, since fabricated DBRs are not ideal and the roughness at the layers interface can decrease the reflectivity coefficient.

2.2.2 Cavity

As already mentioned in the previous section, the microcavity can be realized by growing two mirrors placed at distance L_c apart from each other. Since the propagation of light into the DBRs takes place, in order to obtain more accurate calculations, the cavity length should be replaced by the effective length, which is the sum of the cavity length L_c and the phase penetration length L_{DBR} [28]:

$$L_{eff} = L_c + L_{DBR} \quad (2.2.11)$$

where

$$L_{DBR} = \frac{\lambda}{2n_c} \frac{n_L n_H}{n_H - n_L} \quad (2.2.12)$$

The phase penetration length can be illustrated by imaginary expansion of the existing structure and by placing a fixed-phase mirror at depth L_{DBR} [29], as long as the phase of the original and replaced mirrors is the same at the centre wavelength λ_0 . Due to the high reflectivity, and hence low transmission T ($R + T = 1$), photons inside the cavity bounce back and forth between two mirrors a large number of times before escaping the cavity. If during a round trip the phase changes an integer number of 2π , the constructive interference occurs and the cavity is in resonance. Such a situation occurs when the spacing

L_c between reflectors is a multiple number n of half-wavelengths $\lambda/2$:

$$L_c = n \frac{\lambda}{2} \quad (2.2.13)$$

The phase properties depend on wavelength – for the centre of the mirror stop-band both dispersion and the reflection delay are minimal and they enhance with increasing detuning [29, 30].

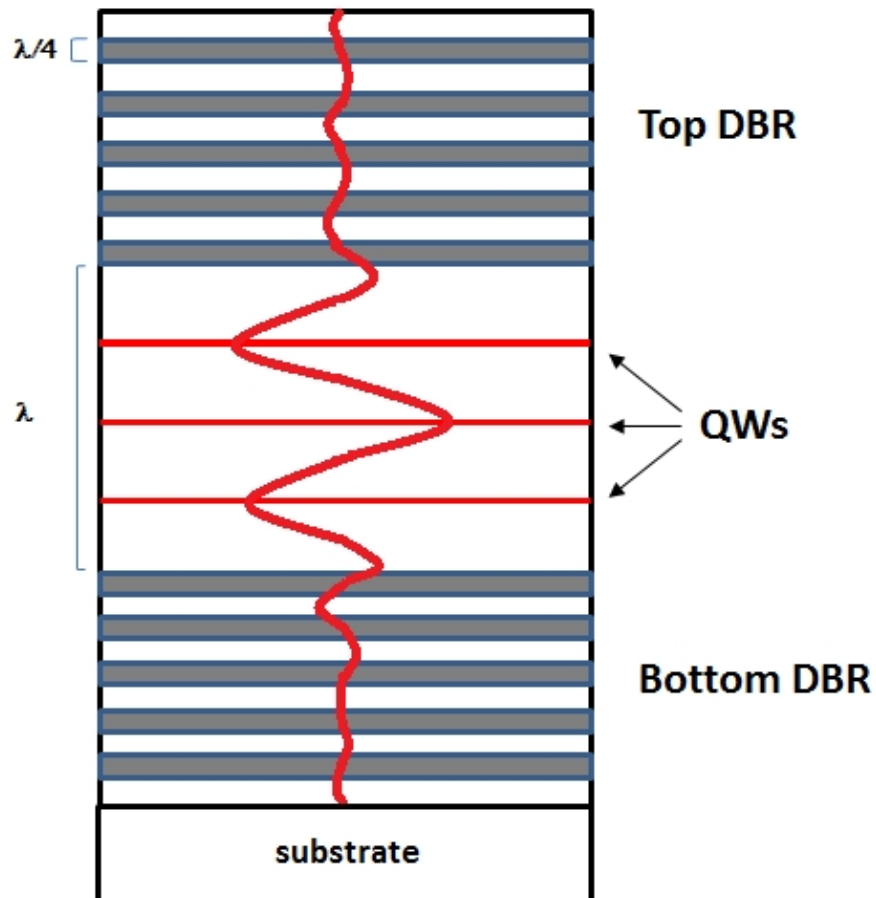


Figure 2.2.2: Schematic diagram of a microcavity with three quantum wells embedded in a λ cavity.

2.3 Microcavity polaritons

If the system is in the strong coupling regime excited emitter and empty cavity ($|1, 0\rangle$) and emitter in a ground state and photon in the cavity ($|0, 1\rangle$) are no longer eigenvalues of the system – they become replaced by entangled exciton-photon states, being the linear combination of the above ($(|0, 1\rangle \pm |1, 0\rangle)/\sqrt{2}$) and giving a rise to new quasi-particles called polaritons. Exciton-polaritons are quasiparticles, obeying the bosonic statistics and are formed as a result of the strong coupling between excitons and photons. Due to the fact that polaritons are composite particles, they inherit the properties of their components. Thanks to the photonic fraction, polaritons have very small effective mass and, what is one of the most important properties, they can be excited optically and optically measured, which allows studying polariton systems without destroying quantum mechanical interference. Participation of excitons in the process of forming polaritons allows them to interact with each other.

Strong and weak coupling regimes

Let us consider a GaAs-based cavity with embedded quantum wells (could be either InGaAs or GaAs). If the exciton transition is in resonance with the photon mode, then the strong exciton-photon coupling may occur. As a result of this coupling new hybrid light-matter states are formed, which are called exciton-polaritons. The minimum splitting between the exciton and cavity modes is called the vacuum Rabi splitting and is an important characteristic of the microcavity, being the measure of the coupling strength. Its relation to the strength of the coupling V is straightforward and can be written as $\Omega = 2V$. The Rabi splitting depends on the free exciton radiative width $\hbar\Gamma_0$, number of quantum wells N_{QW} and on the effective length of the cavity. In the high reflectivity limit, where $1 - R \ll 1$ the Rabi splitting is given by: [28]:

$$\hbar\Omega \sim 2\hbar\sqrt{\frac{2\Gamma_0 c N_{QW}}{n_c L_{eff}}} \quad (2.3.1)$$

In reality, considering the polariton dispersion, we should take into account linewidths of the exciton (γ_X) and the cavity photon (γ_c). Close to the resonance the polariton dispersion can be written as:

$$E(k_{\parallel}) = \frac{E_X(k_{\parallel}) + E_c(k_{\parallel}) - i(\gamma_X + \gamma_c)}{2} \pm \frac{1}{2}\sqrt{V^2 + \frac{1}{4}[E_X(k_{\parallel}) - E_C(k_{\parallel}) - i(\gamma_c - \gamma_X)]^2} \quad (2.3.2)$$

where $V = \sqrt{\frac{1+\sqrt{R}}{\sqrt{R}} \frac{c\Gamma_0}{n_c L_{eff}}}$ and $\gamma_c = \frac{1-\sqrt{R}}{\sqrt{R}} \frac{c}{n_c L_{eff}}$, R-reflectivity.

When $E_X(k_{\parallel}) = E_c(k_{\parallel})$ we can distinguish two regimes, which are dramatically different in terms of peculiarity of occurring physical phenomena:

- $2V < |\gamma_c - \gamma_X|$ - the square root is purely imaginary and the system is operating in the weak coupling regime
- $2V > |\gamma_c - \gamma_X|$ - the square root becomes real and the system is in the strong coupling regime

for the latter case the Rabi splitting becomes:

$$\Omega = 2\sqrt{V^2 - \frac{1}{4}(\gamma_X - \gamma_c)^2} \quad (2.3.3)$$

which shows that the Rabi splitting depends on the γ_X and γ_c .

In a microcavity operating within the weak coupling regime, the coupling between the exciton and cavity mode is very weak compared to the cavity losses, so the probability of photon re-absorption is very low and after excitation emitter decays to the ground state with no Rabi oscillation. This situation corresponds to a typical vertical cavity surface emitting laser (VCSEL).

We say about strong coupling regime if the vacuum Rabi splitting is by far larger than exciton and cavity linewidths. In microcavities with high Q factor photons emitted by excitons remain in the cavity for so long before escaping, that it is very likely that they will be reabsorbed. As a result, periodical energy exchange between the emitter and the cavity occurs and is called Rabi oscillations. In such a system, the quantum well exciton and the cavity photon can be described in terms of two harmonic oscillators coupled via the light-matter interaction, which are analogous to the resonant atomic two-level system. Since the crystal is translationally invariant in the plane of quantum well, the exciton in-plane wave vector is a good quantum number and must be equal to the wave vector of photon during optical transition. As a consequence, exciton has well defined in-plane wave vector and interacts only with one cavity mode [1]. The strong coupling regime in semiconductor microcavities was observed for the first time in 1992 by Weisbuch [1] (figure 2.3.1), starting the new era of research on exciton-polaritons.

Due to the confinement of the excitons in a quantum well, the degeneracy of the heavy- and light-hole excitons vanishes, resulting in only double spin degeneration of lower (LPB) and upper (UPB) polariton branches [31]. As a result of the sharp dispersion of cavity polariton modes, their effective mass is reasonably small (of the order of 10^{-4} times the free electron mass and 10^{-9} times rubidium atom mass). According to the theoretical predictions, it should be possible to obtain Bose-Einstein Condensation-like many-body coherent state much easier than for the atomic gas system, since the condensate is expected to occur at lower particle density and at a higher temperature [2].

Considering excitons, we cannot forget that they are not pure bosons. They are formed of two fermions and hence they are, so called, composite bosons, which bring some consequences. Whereas the commutation relation of creation

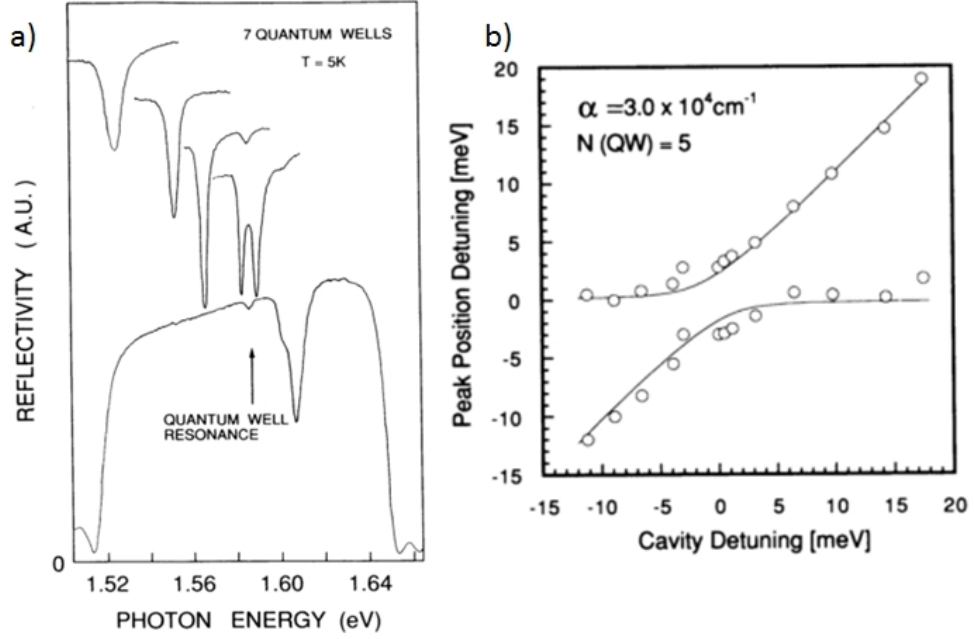


Figure 2.3.1: a) strong coupling regime reflection spectra from a 7QWs microcavity structure at various detunings. b) reflectivity peak position as a function of cavity detuning (source: [1]).

and annihilation operators of a perfect boson is equal to 1: $[b_s, b_s^\dagger] \sim 1$, in case of excitons it has to be corrected by adding an additional term:

$$[b_s, b_s^\dagger] \sim 1 - O(na_B^d) \quad (2.3.4)$$

where n is the exciton density and a_B^d is the Bohr radius of exciton in d -dimensional system.

From equation 2.3.4, we can see that the value of this commutator decreases with increased excitons density. This behaviour means, that only at low densities excitons can be approximately treated as bosons. It has been shown, that in the dilute limit ($na_B^d \ll 1$) excitons behave like weakly interacting boson and in a high density system ($na_B^d \gg 1$) they are analogous to Cooper pairs, called excitonic insulator [32]. In concert with increasing the carrier density, electron and hole pairs become more and more fermionic, up to the critical density $n_M \sim 1/a_B^d$, called Mott density, when no bound electron-hole state can

be stable anymore and the crossover to a metallic electron-hole plasma occurs. Accompanying renormalization of the exciton oscillator strength leads to the reduction of the light-matter coupling strength V . This results in reduction of the Rabi splitting (eq.2.3.3). By decreasing the strength of the exciton-photon interaction, the energy dispersions of the upper and lower polariton states become more and more photonic- or excitonic-like, finally synchronizing with bare photonic and excitonic modes for the situation with no exciton-photon coupling. This transition is called cross-over from the strong to weak coupling regime [33, 34, 35].

In case of InGaAs/GaAs quantum wells with 4% – 6% In content (as in quantum wells studied in this thesis), the Bohr radius is equal to $\sim 11nm$ [36], which gives us the Mott density $n_M \approx 1/a_B^3 \approx 8 \times 10^{11}cm^{-3}$.

Another possibility of transition from the strong to weak coupling regime is increase of the temperature above the exciton ionization temperature, which causes thermal exciton dissociation [37]. Figure 2.3.2 presents the phase diagram of GaAs based microcavity, showing the limits of strong coupling regime depending on the critical concentration and temperature.

2.3.1 Eigenenergies and dispersion of polariton states

In order to describe dispersion of polaritons, we can start with recalling that photons in a vacuum have linear dispersion given by:

$$E(k) = \hbar c |k|, \quad (2.3.5)$$

where c is the velocity of the light and $|k| = \sqrt{k_x^2 + k_y^2 + k_z^2}$ is the wave vector. Taking into account confinement in the cavity direction (k_z) as well as the fact

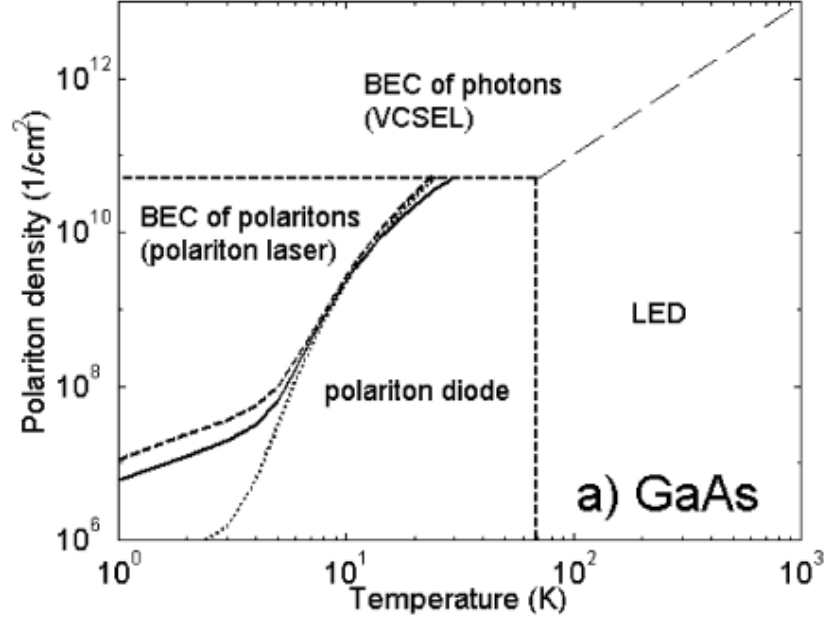


Figure 2.3.2: Phase diagram of GaAs based microcavities. Vertical and horizontal lines indicate limits of the strong coupling regime. Solid line shows the critical concentration versus temperature of the polariton KT phase transition. Dotted and dashed lines indicate the critical concentration for quasi condensation in $100\mu m$ and in one meter lateral size systems, respectively (source: [38]).

that cavity has a certain refractive index n_c , dispersion of the cavity mode becomes:

$$E_c(k) = \frac{\hbar c}{n_c} \sqrt{\left(\frac{2\pi}{L_c}\right)^2 + k_{\parallel}^2} \quad (2.3.6)$$

where L_c is the cavity thickness. By using the Taylor expansion, equation 2.3.6 can be approximated to the first order as:

$$E_c(k) \approx \frac{\hbar c}{n_c} \left(\frac{2\pi}{L_c}\right) \left[1 + \frac{k_{\parallel}^2}{2} \left(\frac{L_c}{2\pi}\right)^2\right] \quad (2.3.7)$$

This, in turn, can be expressed as:

$$E_c(k_{\parallel}) \approx E_{c0} + \frac{\hbar^2 k_{\parallel}^2}{2m_c^*} \quad (2.3.8)$$

where $E_{c0} = \frac{2\pi\hbar c}{L_c n_c}$ is the photon energy at $k_{\parallel} = 0$, as the result of the quantised momentum $k_{\perp} = \frac{2\pi}{L_c}$ and $m_c^* \approx \frac{\hbar m_c}{c L_c}$ is the effective mass of the cavity photon.

The dispersion of quantum well excitons also can be written using an effective mass of the exciton m_X^* and energy of the exciton at $k_{\parallel} \approx 0$ E_{X0} :

$$E_X(k) \approx E_{X0} + \frac{\hbar^2 k_{\parallel}^2}{2m_X^*} \quad (2.3.9)$$

Formation of the polaritons can be thus expressed in terms of a simplified model of two oscillators. The Hamiltonian of the strongly coupled exciton-photon system is then given by:

$$H_0 = \sum_k E_c(k_{\parallel}) a_k^{\dagger} a_k + \sum_k E_X(k_{\parallel}) b_k^{\dagger} b_k + \sum_k \hbar\Omega (a_k^{\dagger} b_k + b_k^{\dagger} a_k) \quad (2.3.10)$$

where $\hbar\Omega$ stands for the coupling energy and $a_k^{\dagger} a_k$ and $b_k^{\dagger} b_k$ are the operators of creation and annihilation of photons and excitons respectively.

This Hamiltonian can be also written in the form of matrix:

$$H = \begin{bmatrix} E_X(k_{\parallel}) & \hbar\Omega \\ \hbar\Omega & E_c(k_{\parallel}) \end{bmatrix} \quad (2.3.11)$$

The eigenvalues of the matrix 2.3.11 give us the dispersions of lower and upper polariton branches:

$$E_{UPB}(k_{\parallel}) = \frac{E_c(k_{\parallel}) + E_X(k_{\parallel})}{2} + \frac{1}{2} \sqrt{(E_c(k_{\parallel}) - E_X(k_{\parallel}))^2 + 4\hbar^2\Omega^2} \quad (2.3.12)$$

$$E_{LPB}(k_{\parallel}) = \frac{E_c(k_{\parallel}) + E_X(k_{\parallel})}{2} - \frac{1}{2} \sqrt{(E_c(k_{\parallel}) - E_X(k_{\parallel}))^2 + 4\hbar^2\Omega^2}$$

and have physical meaning of the energies of the upper ($E_{UPB}(k_{\parallel})$) and lower ($E_{LPB}(k_{\parallel})$) branches of the polariton state.

Squares of the Hopfield coefficients [39] used in order to diagonalise this Hamiltonian are given by:

$$\begin{aligned} |X(k_{\parallel})|^2 &= \frac{1}{2} \left(1 + \frac{\Delta E(k_{\parallel})}{\sqrt{(\Delta E(k_{\parallel}))^2 + 4\hbar^2 \Omega^2}} \right) \\ |C(k_{\parallel})|^2 &= \frac{1}{2} \left(1 - \frac{\Delta E(k_{\parallel})}{\sqrt{(\Delta E(k_{\parallel}))^2 + 4\hbar^2 \Omega^2}} \right) \end{aligned} \quad (2.3.13)$$

where $|X(k_{\parallel})|^2 + |C(k_{\parallel})|^2 = 1$ and determine the fraction of excitons ($|X(k_{\parallel})|^2$) and photons ($|C(k_{\parallel})|^2$) in polariton wavefunctions. $\Delta E(k_{\parallel}) = E_c(k_{\parallel}) - E_X(k_{\parallel})$ is the energy difference between cavity and exciton modes at $k_{\parallel} = 0$.

Effective mass of polaritons can be defined as the weighted harmonic mean of the effective mass of photon and exciton forming the polariton [40]:

$$\begin{aligned} \frac{1}{m_{LPB}^*} &= \frac{|X|^2}{m_X^*} + \frac{|C|^2}{m_c^*} \\ \frac{1}{m_{UPB}^*} &= \frac{|C|^2}{m_X^*} + \frac{|X|^2}{m_c^*} \end{aligned} \quad (2.3.14)$$

As the effective mass of the photon is much smaller at $k_{\parallel} \approx 0$ than the effective mass of the exciton $m_c^* \ll m_X^*$, equations 2.3.14 can be approximated by:

$$\begin{aligned} m_{LPB}^*(k_{\parallel} \approx 0) &\simeq \frac{m_c^*}{|C|^2} \sim 10^{-4} m_X^* \\ m_{UPB}^*(k_{\parallel} \approx 0) &\simeq \frac{m_c^*}{|X|^2} \end{aligned} \quad (2.3.15)$$

2.3.2 Polariton dispersion

The difference between the energy of the cavity and the energy of the exciton is called detuning $\Delta E(k_{\parallel}) = E_c(k_{\parallel}) - E_X(k_{\parallel})$ and if $\Delta E = 0$, then in the ground state polaritons are composed of 50% excitons and 50% photons. Detuning can be easily changed by fabricating samples with varying length of the cavity.

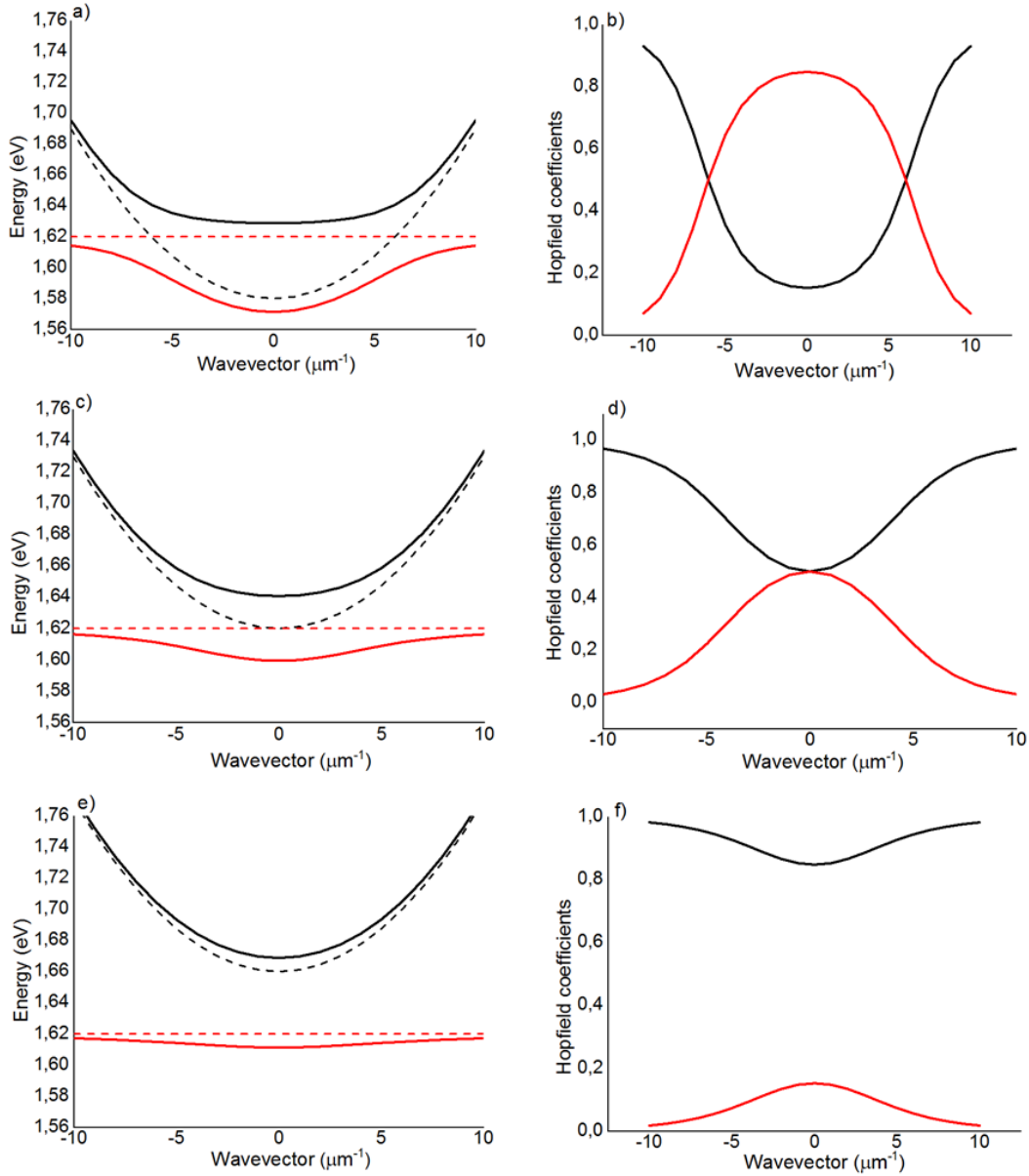


Figure 2.3.3: Dispersions of polariton branches for different exciton-photon detunings. Images show energies of exciton-polaritons vs. wavevectors at a) negative ($\Delta E = -40\text{meV}$), c) zero ($\Delta E = 0$) and e) positive ($\Delta E = 40\text{meV}$) detuning between photon and exciton modes (black and red solid lines are UPB and LPB, black and red dotted lines are bare cavity and exciton, respectively), as well as corresponding Hopfield coefficients b), d) and f) respectively (black line: $|X(k_{\parallel})|^2$, red line: $|C(k_{\parallel})|^2$).

Figure 2.3.3 depicts simulated energy dispersions of the polaritons versus the

wave vectors of a typical GaAs microcavity for three different detunings (negative $\Delta E < 0$, zero $\Delta E = 0$ and positive $\Delta E > 0$) as well as corresponding Hopfield coefficients. It is straightforward that the shape of the dispersion strongly depends on the detuning ΔE between photonic and excitonic modes. Whereas the upper polariton branch can be approximated by a quadratic function for positive detuning, the lower polariton branch is strongly non-parabolic for any ΔE and has a point of inflection, where the effective polariton mass changes from positive to negative value. The more positive the detuning ΔE is, the more excitonic character lower polariton branch has, with clearly seen inflection points. Figures presenting the dependence of Hopfield coefficients versus the k-vector show strong relation between the fraction of excitons and photons forming the polaritons and the wave vector. With increase of the wave vector the LPB branch becomes more exciton-like, whereas the UPB branch becomes more photon-like. Such behaviour implies that the exciton-photon coupling is effective only at small k-vectors. It is also worth noticing how peculiar are shapes of the Hopfield coefficients fractions versus k-vector functions for different detuning ΔE . During the MBE growth usually the cavity thickness varies across the sample, which enables us to study polariton states with different exciton-photon detunings.

2.4 Bose-Einstein Condensation

2.4.1 Equilibrium BEC

From the indistinguishability of particles in the quantum mechanical approach, interchanging of two coordinates in an N-particle state function should result with the same physical state, different from the original one by a factor α

$$\begin{aligned} \psi(r_1, \dots, r_j, \dots, r_k, \dots, r_N) &= \alpha \psi(r_1, \dots, r_k, \dots, r_j, \dots, r_N) = \\ &\alpha^2 \psi(r_1, \dots, r_j, \dots, r_k, \dots, r_N) \end{aligned} \quad (2.4.1)$$

It is obvious that α can take only two possible values, square roots of 1: $\alpha = \mp 1$. Depending on the transformation of the wave function, under exchange of any pair, we can distinguish two species of particles: of integral spin - bosons, which transform symmetrically ($\alpha = 1$), obeying Bose-Einstein statistics and half-integral spin fermions, transforming anti-symmetrically ($\alpha = -1$), which obey Fermi-Dirac statistics

$$\begin{aligned} \psi(r_1, \dots, r_j, \dots, r_k, \dots, r_N) &= +\psi(r_1, \dots, r_k, \dots, r_j, \dots, r_N) \text{ (bosons)} \\ \psi(r_1, \dots, r_j, \dots, r_k, \dots, r_N) &= -\psi(r_1, \dots, r_k, \dots, r_j, \dots, r_N) \text{ (fermions)} \end{aligned} \quad (2.4.2)$$

By putting $r_j = r_k$ we can now clearly see that the minus sign in equation for fermions results in the Pauli exclusion principle, meaning that one state can be occupied by no more than one particle, contrary to the bosons, which not only are free to condense in one state, but also with a probability of boson's transition into state with N bosons proportional to $N + 1$. This means that the more bosonic particles occupy one state, the more likely is transition of other bosons into that state, leading to the macroscopic occupation of one energetic state. This is the mechanism leading to the Bose-Einstein condensation.

We can consider a system of non-interacting bosons in a trap in the grand canonical ensemble description, where the system can exchange both energy and particles with the environment.

The probability of the single microstate n_0, n_1, \dots is given by :

$$\rho = \frac{e^{-(E-\mu N)/k_B T}}{Z} \quad (2.4.3)$$

where temperature T and chemical potential μ are control parameters, $E = \sum_{i=0}^{\infty} n_i E_i$ - eigen energies, $N = \sum_{i=0}^{\infty} n_i$ - number of particles, Z - grand partition function

It is now easy to calculate the average occupation number $\langle n_i \rangle$ of particles in a given energy state E_i and it is equal to:

$$\langle n_i \rangle = \frac{1}{e^{(E_i - \mu)/k_B T} - 1} \quad (2.4.4)$$

In order to avoid negative average occupation number of the particles in the ground state, the chemical potential μ must be lower than the energy of the ground state $\mu < E_0$

BEC in 3D systems

We can now consider an ideal Bose gas in the box of volume L^3 with the average number of particles $\langle N \rangle$. Assuming that their energy is high, compared to the distance between the neighbouring occupied energy levels, we can use classical approximation and evaluate the sum over the states with continuous function, hence the average number of particles in the box can be written as

$$\begin{aligned}
 \langle N \rangle &= \sum_{i_x, i_y, i_z} \langle n_i \rangle = \sum_{i_x, i_y, i_z} \frac{1}{e^{(E_i - \mu)/k_B T} - 1} \\
 &\simeq \int \frac{di_x di_y di_z}{e^{(E_i - \mu)/k_B T} - 1} = 4\pi \int_0^\infty \frac{i^2 di}{e^{(E_i - \mu)/k_B T} - 1} \\
 &= \int_0^\infty \frac{g(E) dE}{e^{(E_i - \mu)/k_B T} - 1}
 \end{aligned} \tag{2.4.5}$$

where the density of states $g(E) = \frac{L^3}{4\pi^2} \left(\frac{2m}{\hbar^2}\right)^2 \sqrt{E}$, which after short calculations gives us the result:

$$\langle N \rangle = L^3 \left(\frac{mk_B T}{2\hbar^2 \pi}\right)^{3/2} \sum_{l=1}^\infty \frac{e^{l\mu/k_B T}}{l^{3/2}} \tag{2.4.6}$$

Equation (2.4.6) shows the dependence of the average density of particles in the box $d = \langle N \rangle / L^3$ on the chemical potential and temperature. It is easy to observe from this equation that in order to keep the constant density with lowering the temperature, the chemical potential μ must increase, reaching the energy of the ground state $E_0 = 0$ at temperature $T_c > 0$. This leads to the formula for the critical temperature T_c

$$T_c = \frac{2\pi\hbar^2}{mk_B} \left(\frac{d}{\zeta\left(\frac{3}{2}\right)}\right)^{2/3} \tag{2.4.7}$$

Where $\zeta(x) = \sum_{l=1}^\infty \frac{1}{l^x}$ is the Riemann zeta function and $\zeta\left(\frac{3}{2}\right) \simeq 2.612$

The T_c is the temperature below which the Bose-Einstein condensation takes place, i.e. a macroscopic number of particles starts occupying the ground state of the system. The chemical potential μ at T_c is equal to the energy of the ground state, hence further decrease of the temperature will not affect it. This means that there will remain excited particles in the cloud and their number is:

$$\langle N_e \rangle = L^3 \left(\frac{mk_B T}{2\pi\hbar^2}\right)^{3/2} \zeta\left(\frac{3}{2}\right) \tag{2.4.8}$$

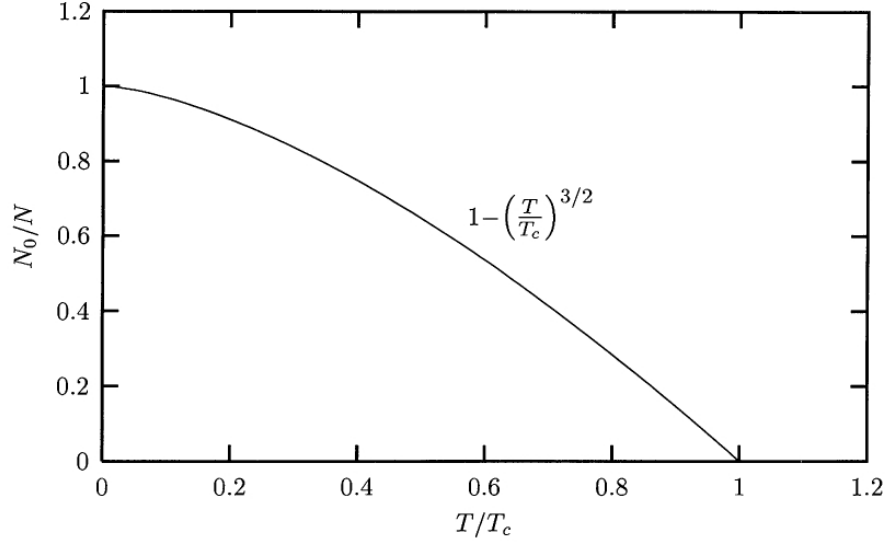


Figure 2.4.1: Condensate fraction N_0/N as a function of temperature in case of a uniform ideal Bose gas. The condensate fraction is different from zero below T_c , where the Bose-Einstein condensation takes place (source: [41])

By combining equations (2.4.6), (2.4.7) and (2.4.8) and we can calculate the average number of particles in the ground state at $T < T_c$:

$$\langle N_0 \rangle = \langle N \rangle - \langle N_e \rangle = L^3 \left(\frac{mk_B T_c}{2\pi\hbar^2} \right)^{3/2} \zeta\left(\frac{3}{2}\right) \left[1 - \left(\frac{T}{T_c} \right)^{3/2} \right] = \langle N \rangle \left[1 - \left(\frac{T}{T_c} \right)^{3/2} \right] \quad (2.4.9)$$

and the ratio of condensed particles to uncondensed particles is

$$\frac{N_0}{N} = 1 - \left(\frac{T}{T_c} \right)^{3/2} \quad (2.4.10)$$

BEC in 2D and 1D systems

Let now consider systems with lower than $d=3$ dimensionalities and see how densities of states, associated with them, influence the fraction of condensed

particles.

In 2D box of size L^2 the density of states does not depend on the energy and has a constant value:

$$g^{2D} = \frac{mL^2}{4\pi\hbar^2} = \text{const} \quad (2.4.11)$$

The average number of particles can be hence expressed as:

$$\langle N^{2D} \rangle \sim \sum_{l=1}^{\infty} \left[e^{\frac{l\mu}{k_B T}} \int_0^{\infty} \left(e^{\frac{-lE}{k_B T} \frac{mL^2}{4\pi\hbar^2}} \right) dE \right] = \frac{mL^2 k_B T}{4\pi\hbar^2} \sum_{l=1}^{\infty} \frac{e^{\frac{l\mu}{k_B T}}}{l} \quad (2.4.12)$$

by putting $\mu = 0$ we obtain $\sum_{l=1}^{\infty} \frac{1}{l}$, which diverges for temperatures higher than 0K, showing that condensate does not occur in 2D systems at finite temperatures.

In case of 1D box of size L, the density of states depends on the energy as $g^{1D}(E) \sim \sqrt{E}^{-1}$:

$$g^{1D}(E) = \frac{L\sqrt{2m}}{8\pi\hbar} \frac{1}{\sqrt{E}} \quad (2.4.13)$$

leading to the average number of particles:

$$\langle N^{1D} \rangle \sim \sum_{l=1}^{\infty} \left[e^{lk_B T \mu} \int_0^{\infty} \left(e^{\frac{-lE}{k_B T} \frac{L\sqrt{2m}}{8\pi\hbar} \frac{1}{\sqrt{E}}} \right) dE \right] = \frac{L}{4\pi} \sqrt{\frac{mk_B T}{\pi}} \sum_{l=1}^{\infty} \frac{e^{\frac{l\mu}{k_B T}}}{l^{1/2}} \quad (2.4.14)$$

and again, it is not possible to obtain a macroscopic number of particles in one state at temperature above absolute zero.

2.4.2 Non-equilibrium BEC - modern approach

Description of the condensate proposed by Einstein is applicable only to systems with a constant number of non-interacting particles that remain in thermodynamic equilibrium, which is far from the real-life conditions. The possibility of observing a condensate in a non-equilibrium state led to a new definition of the BEC criterion. The modern approach to the Bose-Einstein condensate describes it in terms of the off-diagonal long range order, spontaneous symmetry breaking and macroscopic phase coherence, with no need for fulfilling the equilibrium criterion.

To start with this modern definition of BEC, we can consider the one-body density matrix written in a diagonalised form [41]:

$$n^{(1)}(r, r') = \langle \hat{\Psi}^\dagger(r) \hat{\Psi}(r') \rangle \quad (2.4.15)$$

where $\hat{\Psi}^\dagger(r)$ and $\hat{\Psi}(r)$ are the creation and annihilation field operators in the state r , respectively, and they obey the commutation relations:

$$[\hat{\Psi}(r), \hat{\Psi}^\dagger(r')] = \delta(r - r'), \quad [\hat{\Psi}(r), \hat{\Psi}(r')] = 0, \quad [\hat{\Psi}^\dagger(r), \hat{\Psi}^\dagger(r')] = 0 \quad (2.4.16)$$

By setting $r = r'$ in (2.4.15) we can find the diagonal density of the system $n(r)$, momentum distribution and the total number of particles N , which can be obtained through integrating $n(r)$ over r :

$$n(r) = n^{(1)}(r, r), \quad (2.4.17)$$

$$n(p) = \langle \hat{\Psi}^\dagger(p) \hat{\Psi}(p) \rangle, \quad (2.4.18)$$

$$N = \int dr n^{(1)}(r, r), \quad (2.4.19)$$

and $\hat{\Psi}(p) = (2\pi\hbar)^{(-3/2)} \int dr e^{[ipr/\hbar]} \hat{\Psi}(r)$ is the field operator in momentum representation.

Bogoliubov proposed an approximation, allowing describing the condensed system purely in terms of classical physics [42] by a wavefunction Ψ_0 . Ψ_0 , being simply a Schrodinger wavefunction of the single-particle state of the condensation, is known as the condensate wavefunction and has a physical sense of an order parameter, which is characterized by a modulus and a phase:

$$\Psi_0(r) = |\Psi_0(r)|e^{i\Phi(r)} \quad (2.4.20)$$

The order parameter is a quantity characterizing the Bose-Einstein condensed phase and it vanishes above the critical temperature T_c . It determines the degree of order in the system ranging from 0 in case of fully disordered system to 1 for ordered one. The modulus in this equation describes the contribution of the condensate to the diagonal density, whereas the phase $\Phi(r)$ characterizes the coherence and superfluid phenomena.

A very important characteristic of the condensate, showing the link between BEC and superfluidity, is that the velocity of the condensate flow $v_s(r)$ is proportional to the gradient of the phase of the order parameter (eq. 2.4.20):

$$V_s(r) = \frac{\hbar}{m} \nabla \phi(r) \quad (2.4.21)$$

The most important property, following from this relation, is that in any closed contour path in a simply-connected condensate given by Ψ , the phase ϕ can change only by a multiple of 2π to remain Φ single-valued along this path. For ϕ changing by allowed value, at least one point (2D) or a line (3D) has to exist inside this path, where the phase takes any value between 0 and 2π . The system copes with the appearance of such a phase singularity by forming quantized vortices with the unit of circulation $\oint v dl = 2\pi\hbar/m = h/m$, which is equivalent to the vanishing of Φ at this point or line. Equation 2.4.21 also implies that away from phase singularities $\nabla \times v_s = 0$ and therefore, the con-

densate flow is irrotational as proposed by Landau, and can be described in terms of classical irrotational hydrodynamics [70].

Bogoliubov excitation spectrum of an interacting Bose gas is defined as:

$$\epsilon(p) = \left[\frac{gn}{m} p^2 + \left(\frac{p^2}{2m} \right)^2 \right]^{1/2} \quad (2.4.22)$$

where gn is an interaction energy between two particles in the condensate and p is momentum. Depending on the value of momentum, we can distinguish two different regimes of this dispersion. In case of small momentum, when $p \ll mc$, we can rewrite the dispersion law of quasi-particles in a phonon-like form:

$$\epsilon(p) = cp \quad (2.4.23)$$

where $c = \sqrt{gn/m}$ is the sound velocity. According to the Bogoliubov theory, for an interacting Bose gas, the long wavelength excitations are sound waves. In turn for momentum $p \gg mc$ the dispersion law can be approximated with the free particle dispersion:

$$\epsilon(p) \simeq \frac{p^2}{2m} + gn \quad (2.4.24)$$

The transition between these two regimes takes place when $p^2/2m \simeq gn$ and by substituting $p^2/2m = gn$ with $p = \hbar/\xi$, we can obtain formula characterizing the interaction length, called the healing length:

$$\xi = \sqrt{\frac{\hbar^2}{2mgn}} \quad (2.4.25)$$

where g is the coupling constant. This length characterizes the distance over which the interactions between condensed particles tend to remove the density

and phase fluctuations in the condensate and is an important measure in superfluidity phenomenon [43]. The healing length is also used in description of quantized vortices, whose size is of the order of ξ [41].

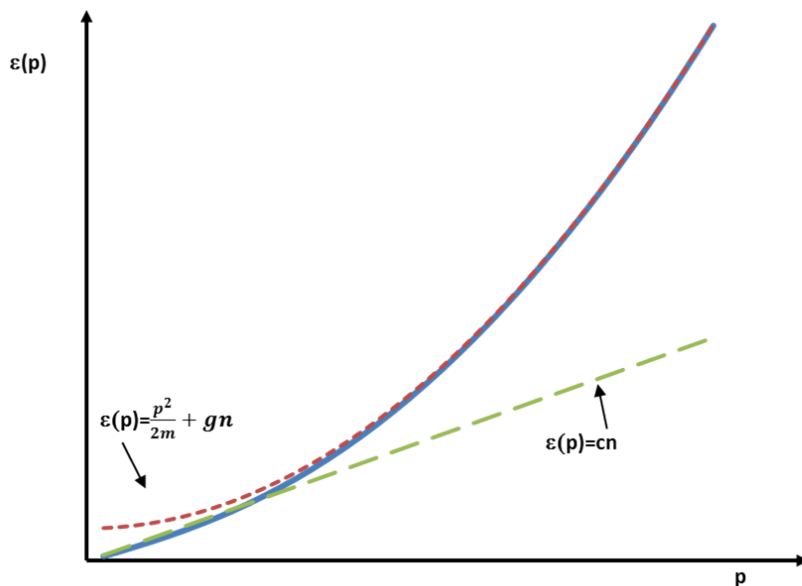


Figure 2.4.2: Bogoliubov dispersion of elementary excitations showing transition between the phonon (cp) and the free particle ($p^2/2m$) regimes.

2.4.3 Observation of Bose-Einstein condensate

Although the Bose-Einstein condensate was predicted in 1924 [44, 45], we had to wait until 1995 for the experimental evidence of this phenomenon. BEC was observed for the first time in the gas of ^{87}Rb atoms in group of Eric Cornell and Carl Wieman [46], which was followed by detection of the BEC in other atomic systems: ^7Li [47] and ^{23}Na [48] in the same year. All these measurements were taken at ultralow temperatures due to the relatively large mass of the atoms, which rather limits the potential application of atomic BEC in industry. On the other end of the mass scale we can place photons, which were expected to

reveal BEC behaviour at room temperature. Indeed, in 2010 the observation of photonic BEC in an optical microcavity was reported by Klaers et al. [49].

Due to the much smaller effective mass and thus higher temperatures of observations, bosonic quasiparticles were seen as good candidates to observe BEC at temperatures accessible with liquid helium, even although such systems are not in thermal equilibrium. In 1999 the Bose-Einstein condensation was observed in solids with magnons in the antiferromagnet $TlCuCl_3$ at much higher temperatures $\sim 14K$, which was possible thanks to the smaller mass of magnons[50], [51]. A few years later the BEC of magnons was detected at room temperature [52]. Another quasiparticle claimed to be a good candidate for BEC measurements was exciton. Many attempts of showing condensate of excitons were taken and various features of BEC were demonstrated [53, 54, 32, 55]

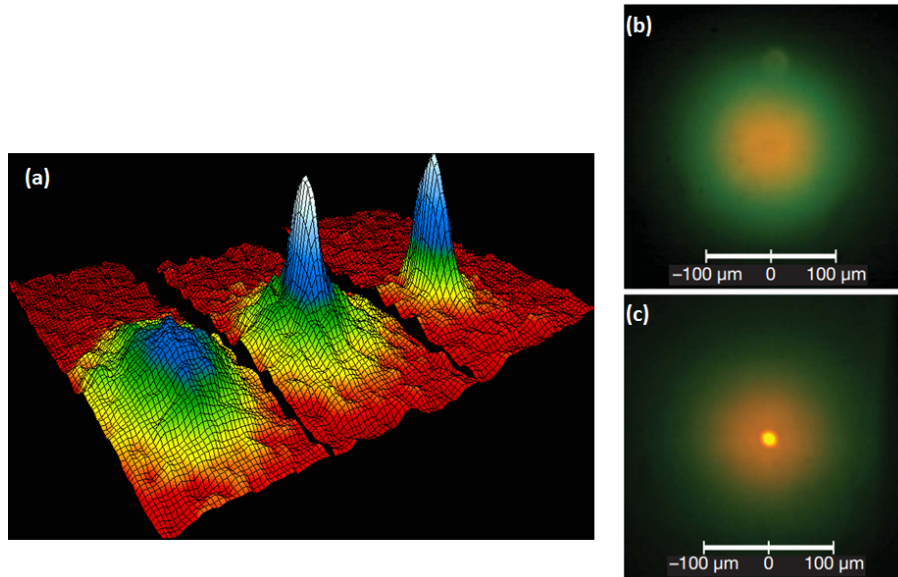


Figure 2.4.3: a) Image of the ^{87}Rb atoms distribution in the cloud before the appearance of the Bose-Einstein condensation (left), at the start of condensation (middle) and after further condensation (right) (source: [56]). Spatial images of the photon gas in the optical microcavity, showing radiation distribution transmitted through cavity mirror below (b) and above (c) critical power level, when transverse ground mode TEM_{00} is macroscopically occupied a(source: [49])

2.5 Non-equilibrium condensate of polaritons

Due to the small effective mass of polaritons (10^9 times smaller than mass of atoms and 10^4 times smaller than a bare exciton mass) they were considered as a system where a Bose-Einstein condensation could take place. In 1996 Imamoglu [57] first came with the theoretical proposition of polariton condensation, which initiated the race for the experimental confirmation of this effect. First attempts of observing condensation were made with GaAs based microcavity samples with a low number of quantum wells, which made the observations difficult due to transition into weak coupling before condensation, caused by a high electron-hole density in a single QW [31, 58, 7, 6].

The condensation of polaritons was for the first time clearly observed by Kasprzak et al. in CdTe sample, containing 16 QWs and having a Rabi splitting of 26meV [2]. They observed condensation of the particles to the ground state and the build-up of a long range spatial coherence and increase of the temporal coherence below temperature $T = 19K$. Two years later the condensation of polaritons in GaN based microcavity at room temperature was reported [8]. In such a structure excitons have high binding energy (28 meV) and hence strong coupling can be sustained at high electron-hole density. In 2009 a polariton condensate in a planar GaAs microcavity was also observed [59]. It is, however, important to point out that BEC in polaritonic systems, unlike the ideal BEC, is not in equilibrium and consists of several condensates emitting at different energies, which was shown experimentally [60, 61]. Figure 2.5.1 shows the condensate density in the reciprocal space, measured at three different pump powers, presenting formation of the sharp peak with increasing the excitation power. Since in this condensate the dynamic equilibrium between pump and polaritons decay is established, the size of the condensate is determined by the size of the pump spot and hence the long range spatial coherence does not extends to infinity as expected for the equilibrium case.

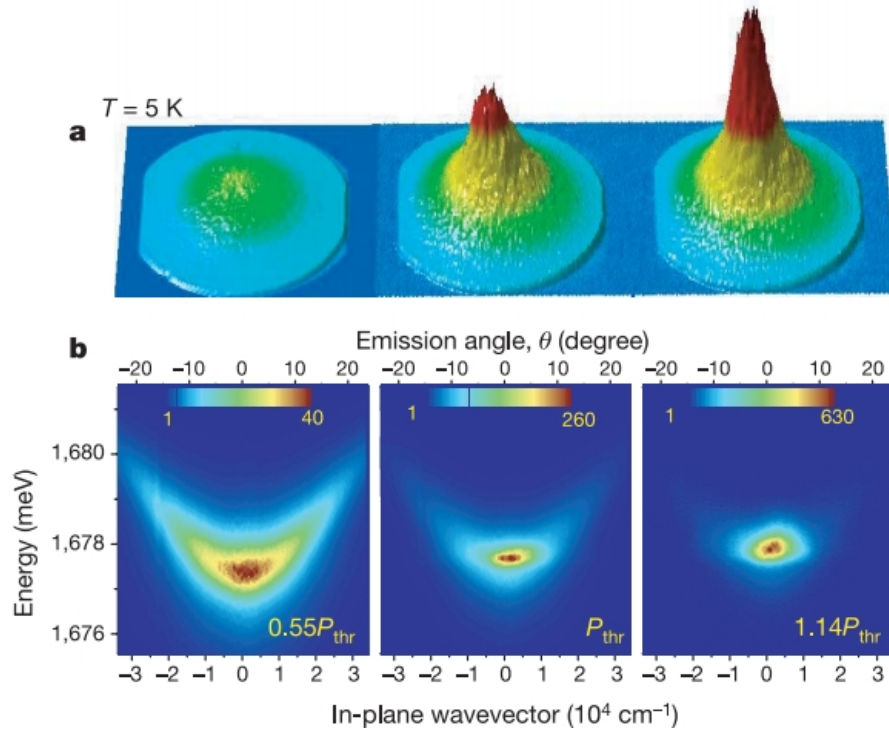


Figure 2.5.1: Bose-Einstein condensation of polaritons. a) 3D images of the far-field emission at angles between $\pm 23^\circ$ and b) the corresponding data resolved in energy, revealing the formation of the condensation in the ground state along with increasing the pump power (source: [2])

2.5.1 Non-resonant and resonant (OPO) polariton condensate excitation

Depending on the energy of excitation in regard to the energy of the lower polariton branch, there are two ways of exciting polariton condensate with external laser: non-resonant and resonant excitations, schematically imaged in figure 2.5.2.

Non-resonant excitation

In non-resonant laser excitation, free carrier states of the quantum well are excited at energies higher than upper polariton branch, which then relax to the bottom of the lower polariton branch through acoustic and optical phonon interaction [2]. At large k-vectors the lifetime of the particles is long, density of states is large and dispersion curve is very gradual, since it is almost excitonic. In this part of the branch polaritons relax towards the lower energy states efficiently due to the scattering mediated by acoustic phonons. This relaxation process is fast compared to the particles lifetime.

The situation changes when polaritons arrive at the inflection point, where the strongly coupled part of the branch begins. In this region polaritons are photonic-like and thus dispersion curve is very steep (depending on the detuning between photon and exciton modes), effective mass is drastically reduced, hence the density of states is decreased as well, and lifetime of polaritons is also much shorter (1-10ps) than in excitonic part. Polaritons at the inflection point still have a few meV way to go towards the ground state. They interact with 3D acoustic phonons, which have a wavevector $\sim 1/\text{size of the quantum well}$ and energy $\sim 1\text{meV}$, but since the required energy transfer is larger than available energy of the acoustic phonons, the relaxation process slows down and can take longer than the polariton lifetime, preventing them to relax to the ground state at $k = 0$. Instead, polaritons accumulate at the inflection point, giving a rise to a phenomenon called the bottleneck effect, which was first reported by Tassone et al. in 1997 [62] and observed experimentally by Tartakovskii et al. [63].

The bottleneck effect, called the ineffective relaxation with phonons, can be easily overcome by increasing the polariton density. At higher excitation power inter-particle scattering becomes important and polariton-polariton, polariton-exciton and exciton-exciton scattering leads to suppression of the bottleneck.

Polariton scattering induced by exciton-exciton collisions can follow one of two likely scenarios. First possibility is that one of the excitons can be scattered into the free-particle state and the other one into the strongly coupled regime. The other one is that first exciton can be scattered to the upper polariton branch and the second one to the lower polariton branch close to the $k = 0$ [63]. The opening of this additional relaxation channel at high densities facilitates the polaritons relaxation to the ground state and makes it more efficient than in case of only acoustic phonons mediated scattering at low densities. Presence of disorder in the microcavity is seen as another factor giving rise to more efficient elastic scattering, hence making the relaxation process easier.

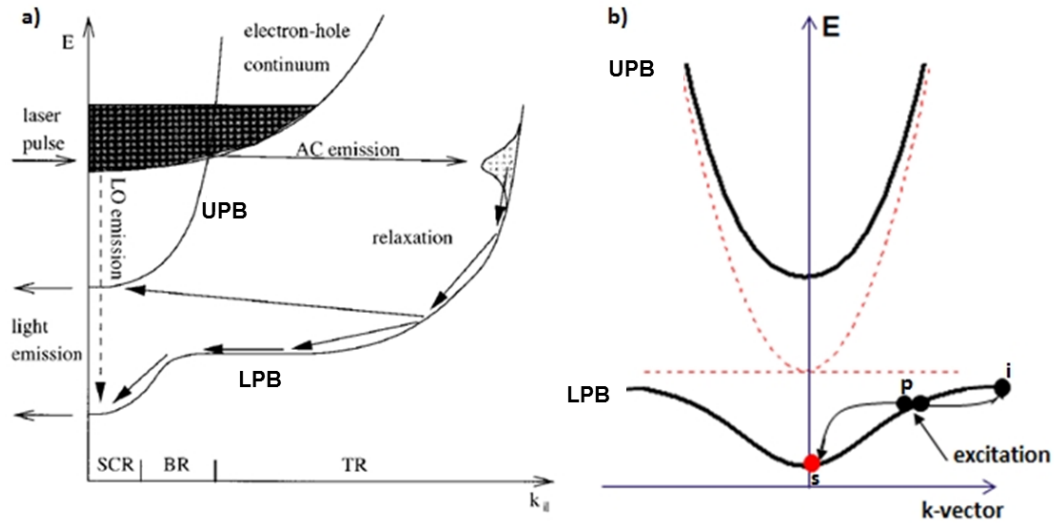


Figure 2.5.2: a) Schematic representation of the non-resonant polariton formation process from the free-carrier thermal reservoir, scattering processes by acoustic-phonon (AC) emission or absorption, and radiative recombination. where SCR-strong-coupling region; BR-bottleneck region; TR-thermal region; LPB and UPB - lower and upper polariton branch, respectively (source: [62]). b) Scheme of the resonant excitation with pump (p), signal (s) and idler (i).

Resonant excitation - Optical Parametric Oscillation (OPO)

Alternative way of creating a polariton condensate at $k = 0$ is resonant excitation into the lower polariton branch, which leads to optical parametric oscillation. In general, resonant excitation relies on tuning the laser to the polariton energy at a given k -vector. Compared to the non-resonant excitation, resonant excitation helps to avoid the bottleneck effect, since the injection takes place at lower part of the dispersion curve.

A very interesting and important effect, occurring under carefully adjusted conditions of resonant excitation was demonstrated in 2000 by two groups [6] [7] [64]. It was discovered, that polaritons injected through coherent pumping with continuous wave (cw) laser tuned to be in resonance with LPB, at angles close to the point of inflection can undergo a stimulated scattering process: OPO. At a sufficiently high pump power, two polaritons can scatter into two different states – into zero momentum and higher momentum (called respectively “signal” and “idler”), in such a way, that the polariton energy and momentum are conserved:

$$2E(k_p) = E(k = 0) + E(2k_p) \tag{2.5.1}$$

$$2k_{pump} = k_{signal} + k_{idler}$$

A stimulated scattering process occurs due to the bosonic character of the polaritons and allows formation of the $k = 0$ final state populations close to unity through polariton-polariton interactions. This behaviour is much different than under non-resonant excitation, where the population of excitons and polaritons with high momentum is significant, since only a small fraction of polaritons can reach the minimum of the LPB. It has been experimentally shown that phase of the pump polaritons do not influence the phases of the signal nor idler polaritons, hence the created condensate is independent from the pump and only condition that $\phi_{signal} + \phi_{idler} = 2\phi_{pump}$ has to be fulfilled. Since in OPO only

the pump mode is determined by the laser and both the signal and the idler phases are chosen spontaneously, formation of the spontaneous coherence can be observed. The presence of long-range spatial and temporal coherence of the OPO signal was predicted to occur by Carusotto and Ciuti [65] and shortly after experimentally confirmed [66], [67].

The spontaneous macroscopic occupation of the single state in OPO, accompanied by appearance of the polariton field coherence, is a kind of condensation and resembles the conventional Bose-Einstein condensation. However, we cannot forget that the polariton condensate is not only a low dimensional system, but it is also far from equilibrium and has to be distinguished from a pure equilibrium BEC. It has been also shown that condensate always arises at $k = 0$ and does not depend on the k_{pump} , which is due to the self-organization of polariton-polariton scattering, since the coupling between three states – pump signal and idler leads to the renormalization of the lower polariton branch [68].

When the lower polariton branch becomes macroscopically occupied, shifting of polaritons towards higher energies occurs, which is due to polariton-polariton interactions and it is proportional to the population of polaritons. This effect is called blueshift.

Moreover, bistable behaviour of the pump polariton population vs. laser power is expected to occur and this bistability threshold is usually the same as the OPO threshold [68].

Bistable behaviour in strongly coupled microcavities was first observed by Baas et al. in 2004 [69]. The relative difference between the energy of the laser and the energy of the bare polariton allows us to distinguish two possible behaviours. If the energy of the laser is smaller than the bare polariton energy, then the occurring blueshift results in reduction of the pump light absorption. In turn, when the energy of the laser is higher than the bare polariton energy,

then the blueshift brings the polaritons towards resonance, which enhances the absorption. Depending on the pumping power, the pump mode can have either low occupation accompanied by a small blueshift or high occupation, and thus larger blueshift. This means that the same pump energy and intensity can result in polaritons being in one of two possible states, characterized by different polariton density and energy. The threshold between these two states is called bistable threshold. The mean polariton number as a function of input intensity is presented in figure 2.5.3 and it exhibits the hysteresis cycle when changing the pump intensity.

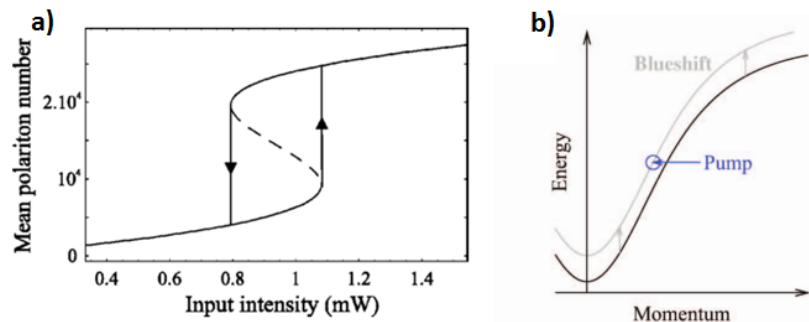


Figure 2.5.3: a) Bistable behaviour of the mean polariton population as a function of input intensity (source: [69]), b) Scheme of the blue-shift driven bistability (source: [70]).

2.5.2 Superfluidity

Superfluidity is a phenomenon closely related to the Bose-Einstein condensation and describes the behaviour of fluids with zero shear viscosity, that can flow through narrow capillaries or slits without dissipating energy - superfluids. Whereas in BEC superfluidity exists as a natural consequence of the phase homogeneity in direct space, in general, superfluidity can exist without a strict BEC, since it can occur with only two points in space being connected by a phase coherent path. Therefore, the mixed state of normal and superfluid phase is possible in a polariton condensate and it is expected to take place below a critical temperature, known as the Berezinskii-Kosterlitz-Thouless transition temperature T_{BKT} . This physical effect was independently discovered in 1938 by Kapitza [71] and by Allen and Misner [72]. Few years later, in 1941 Landau formulated a superfluidity theory consisting of few postulates [73]. The most important one says that under certain criteria, the particle moving inside the liquid with velocity smaller than the critical velocity

$$V_c = \left[\frac{\epsilon(p)}{p} \right]_{min} \quad (2.5.2)$$

does not experience any dissipation. This criterion is not sufficient in determining whether the liquid is in the superfluid regime or not - existence of the phase coherence and long range order are considered to be more relevant to study superfluidity.

Theoretical studies of non-equilibrium Bose-Einstein condensate of microcavity polaritons [74] led to a mean-field theory of its dynamics and allowed understanding the dispersion of the elementary excitations in the condensate, which is given by:

$$\omega_{\pm}(k) = -i\Gamma/2 \pm \sqrt{[\omega_{Bog}(k)]^2 - \Gamma^2/4} \quad (2.5.3)$$

where

$$\omega_{Bog} = [\omega_k(\omega_k + 2gn)]^{1/2} \quad (2.5.4)$$

with $\omega_k = \hbar k^2/2m_{LPB}$ being the Bogoliubov dispersion of equilibrium dilute Bose gases, gn - interaction energy between two particles in the condensate and Γ - the effective relaxation rate. Bogoliubov excitations in polariton condensate were later experimentally observed [75] and are presented in figure 2.5.4. Polariton superfluidity has been observed in 2009 [3] in the resonant excitation regime as the motion of quantum fluid around the defect without scattering above some critical polariton density.

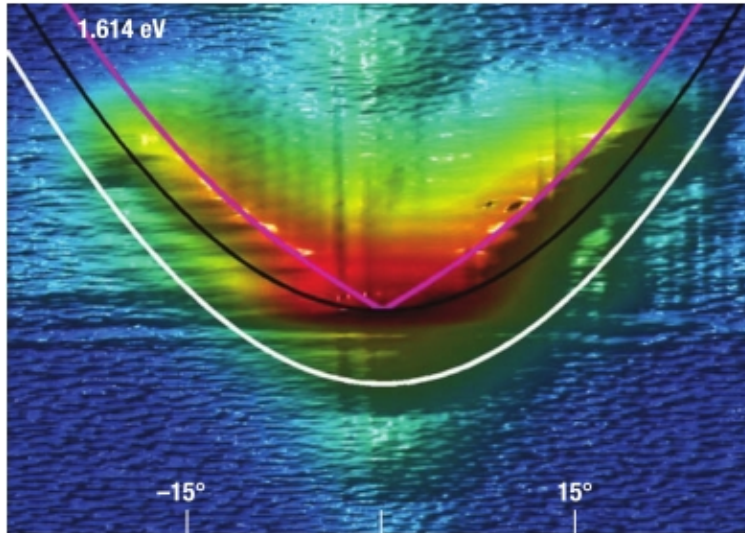


Figure 2.5.4: Bogoliubov dispersion of elementary excitations in exciton polaritons with detuning $\Delta = 1.6meV$ and pump rate $P = 6P_{th}$. Theoretical lines represent: pink line - Bogoliubov excitation energy according to homogeneous model, black line - the quadratic dispersion curve of lower polariton branch, starting from the condensate energy, white line - the quadratic dispersion curve of lower polariton branch without interaction (source: [75]).

2.5.3 Vortices and Solitons

The optical non-linearity of microcavity polaritons originates mainly from the interaction effects and arises from strong exciton-exciton interactions. Nonlinear character of the polariton condensate gives rise to many interesting effects like, already described in this thesis, power-dependent blueshift, parametric scattering and bistability or vortices and solitons, which will be described below.

Vortices

The polariton condensate is a non-equilibrium system, in which spontaneous currents moving polaritons from gain-dominated to loss-dominated areas occur. Due to the interplay of these currents and the potential landscape, caused by disorder or defects, vortices can be spontaneously formed. Vortices in superfluids are characterized by rotation of the phase around the vortex by $2\pi n$, where n -integer, and by vanishing of the superfluid population at their core. The vortex radius is given by the healing length ξ (equation 2.4.25).

Experimental confirmation of the vortex creation requires two signatures to be observed. First, a strong change of the polariton spatial distribution with a polariton intensity drop, corresponding to the vortex core, has to be observed. Then, the interfered luminescence signal with its retro-reflected image has to be measured. If the interference pattern reveals two fork-like dislocations, a vortex with a 2π phase winding around its core is present [4].

Spontaneous formation of pinned quantized polariton vortices was observed for the first time in incoherently pumped system in 2008 by Lagoudakis et al. [4] (figure 2.5.5a,b). Two years later creation of vortices in the OPO regime of

the polariton condensate has been experimentally demonstrated [76]. In this experiment vortices were formed with a weak external imprinting beam, carrying orbital angular momentum (OAM). It was observed that the vortex core radius depends on the strength of the polariton-polariton interactions, since it decreases with increasing polariton density. Later, we showed experimentally, that the vortex core size decreases up to a certain pump power. At sufficiently high powers, it is more favourable for the system to adopt next higher double charged vortex state with OAM $M = 2$ (figure 2.5.5c). This is due to the limited size of the potential profile, which means, that at high enough polariton density, M has to be increased. It can be seen by equating the kinetic term with the interaction energy of the system: $\frac{\hbar^2}{2m\xi^2}M^2 = \alpha N$, where α - interaction constant of polaritons, N -number of polaritons. Such a situation can be observed as an abrupt increase of the vortex core size, appearing in concert with an additional fork arm. The experiment also proved theoretical predictions that the OAM is conserved in the parametric scattering process [77]. This phenomenon manifests itself via creation of an antivortex with opposite OAM in the idler, when a vortex is imprinted onto the OPO signal. Hence, due to the polariton-polariton scattering a vortex-antivortex pair arises. Later, spontaneous formation of vortices in an OPO polariton condensate has been also observed [78].

Solitons

Solitons are solitary waves whose shape is conserved during propagation in a dispersive medium. They are a non-linear effect and can exist thanks to the compensation of dispersion by non-linearities in the system. We can distinguish two types of solitons: dark solitons and bright solitons, which can be formed depending on the sign of the polariton effective mass. If the condensate has a positive effective mass, then dark solitons may appear [5], whereas for negative effective mass bright solitons can be formed [79]. Bright solitons are

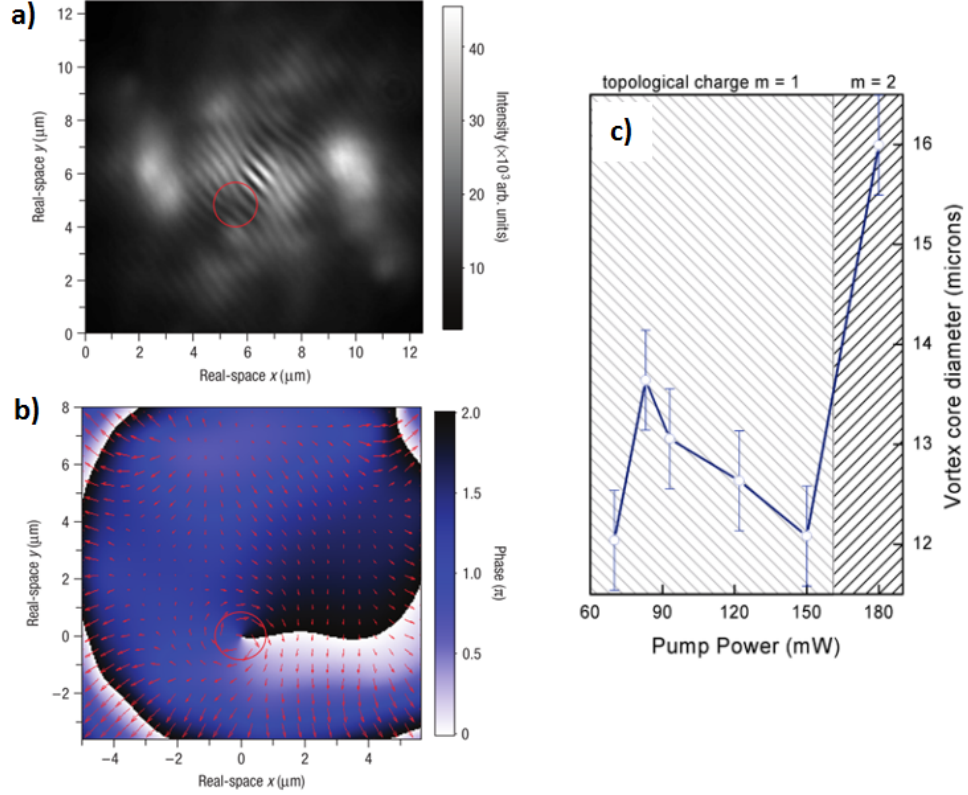


Figure 2.5.5: a) Interferogram with vortex with fork-like dislocation indicated by the red circle, b) theoretical phase profile in the presence of a disorder potential (source: [4]), c) vortex core diameter measured as a function of the pump power, with huge jump of the core diameter at 180 mW, corresponding to transition from the vortex state with topological charge $m = 1$ to the vortex state with $m = 2$.

characterized as a localized intense peak above a continuous wave background in contrast to dark solitons, being formed from a localized intense dip [80]. Figure 2.5.6a shows an image of two propagating oblique dark solitons, generated spontaneously by the photonic defect. Scheme of the bright solitons excitation can be seen in figures 2.5.6b and c. While a CW pump beam, focused to a large spot ($70\mu\text{m}$), compensates polaritons losses, a picosecond writing beam, focused into much smaller area ($7 - 15\mu\text{m}$) triggers formation of bright solitons. Both of them are incident along x-direction. Figures 2.5.6e-h show trajectories of bright solitons, recorded by a streak camera under different excitation conditions. The experiment shows that the velocity of the soliton does not depend

on the writing beam transverse momentum k_{wb} and the size of the soliton is independent of the size of writing beam [79].

As already mentioned, the most striking property of superfluid state is frictionless flow and the absence of excitations when the fluid at flow velocity v_f , smaller than critical velocity v_c , encounters an obstacle. Depending on the size of potential barrier and the flow velocity, propagation of the polariton condensate differs. For small obstacles polaritons can flow almost unperturbed around the obstacle in case of small flow velocity or exhibit Cherenkov scattering at higher flow velocity in the supersonic regime. The situation changes drastically when the size of the obstacle exceeds the healing length of the fluid. Large obstacle induces high flow velocities around it and modulates the condensate density, which may lead to formation of topological excitations like vortices or solitons. The healing length ξ determines the size of solitons and together with the size of the obstacle d they define the number of formed solitons. For $d/\xi \approx 4$ one pair of solitons will be created and for larger defect, when $d/\xi \approx 8$, two pairs of solitons can be observed [81].

Recently, formation of gap solitons in 1D periodic potentials [82] and 2D lattices [83] has been observed. 1D gap solitons arise in the mini-gap, created due to the periodically modulated width of the microwires and resulting periodic potential. 2D lattices are formed by surface acoustic waves, changing the excitonic band gap and creating mini Brillouin zones, separated by mini gaps. In these energy gaps gap solitons can arise, similarly to 1D case. Gap solitons both in 1D periodic wires and in 2D lattices result from the interplay between inter-particle repulsion and negative effective mass at the edges of the first Brillouin zone.

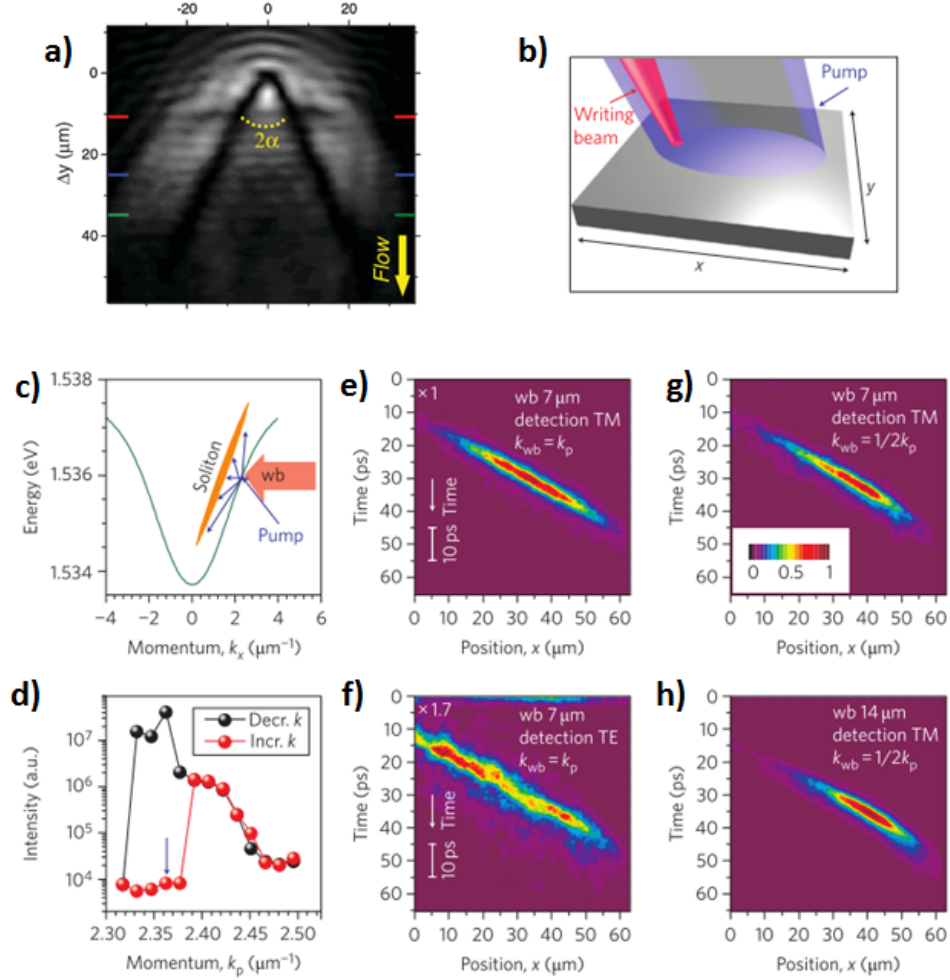


Figure 2.5.6: a) Real space image of the dark soliton doublet nucleated at the defect (source: [5]). b)-h) Bright solitons: b) scheme of bright soliton excitation, c) dispersion of the LPB with schematic representation of the soliton spectrum and excitation scheme, d) bistability of the polariton density vs. pump momentum, e-h) Streak camera measurements of the soliton trajectories along the x -direction under different excitation conditions, where wb-writing beam (source: [79])

2.6 Confining polaritons in 0D and 1D systems

Recently, studying highly confined structures became an important part of polariton physics. The absence of translational invariance in such structures lifts the conservation of wave-vector selection rules during polariton scattering, thus enabling efficient polariton relaxation and build-up of macroscopic occupancy in the low energy states. Confining polaritons into zero- or one-dimensional

structures is seen as direction towards realization of polariton devices.

In the past, many methods have been employed in order to lower the dimensionality of the system. They were either based on modulating the polariton energy or on lateral confinement.

In the first case polariton energy can be modified, *inter alia*, by applying mechanical stress, which induces a potential trap through local change of the bandgap [84, 85].

Another way of introducing a potential barrier and to confine polaritons in lower dimensionality states is to use surface acoustic waves (SAWs) (Figure 2.6.1). SAWs are acoustic waves propagating along the surface of an elastic material, producing a mechanical stress that leads to the formation of the periodic modulation. Their presence influences both polariton components, resulting in lowering the dimensionality of the system. At high phonon density, the periodic modulation creates band gaps in the polariton dispersion and results in formation of the polariton superlattice with a period given by the phonon wavelength. When the amplitude of the SAW induced energy modulation is larger than the energy width of the polariton branch, we can observe transition from 2D into 1D system [86, 87].

The second approach of confining polaritons into 1D or 0D states relies on lateral confining of photonic part of polaritons [88, 89, 90]. Lai et al. showed that 1D polaritons can be created by depositing periodic stripes of metallic thin film on the surface of microcavity structure. The presence of this grating structure modifies the boundary condition of the top DBR, leading to the increase of the cavity photon resonance energy and trapping lower polaritons.

The alternative method was proposed by Daif [91] and Indrissi Kaitouni [92], which allowed obtaining quantum confinement of both upper and lower polari-

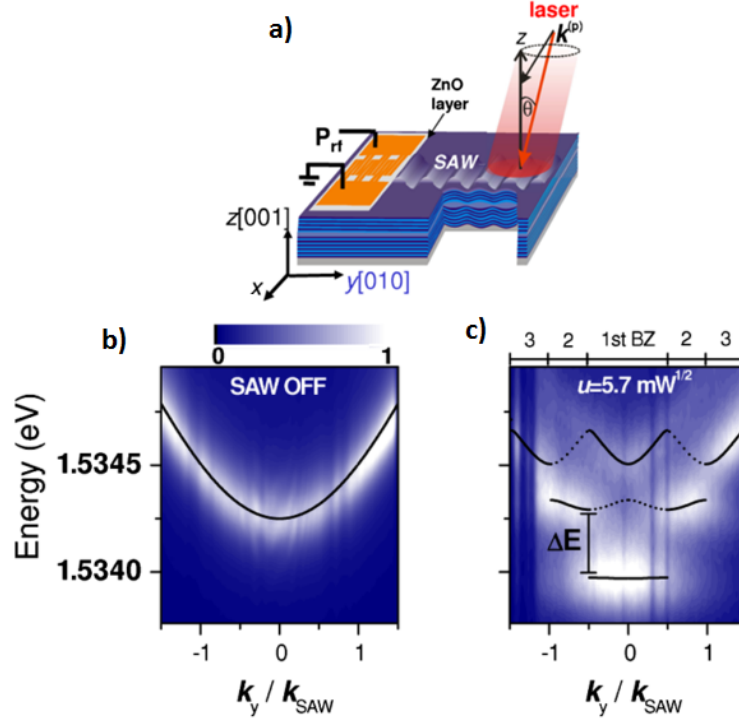


Figure 2.6.1: a) Scheme of the structure with SAWs propagating along the $y = [010]$ direction of the (001) microcavity surface, b) k -space emission from the structure in the absence of SAW and c) in the presence of SAW (source: [87]).

ton modes (Figure 2.6.2). They created localized photonic boxes by etching mesas on the spacer layer, before depositing top DBRs. These etched mesas extend the cavity, which results in lowering the cavity mode and creating a potential trap confining photons. By using photolithography and etching processes any shape and size of the trap can be fabricated, allowing investigating polaritons in 2D, 1D and 0D as well as their interactions.

Finally, the photon mode can be confinement by full etching of the 2D cavity into 1D [93, 94] or 0D [95, 96] structures. Polariton condensates in fully etched GaAs based samples both in 0D (micropillars) [97, 98] and 1D (microwires) [99] were demonstrated in group of Jacqueline Bloch. Since this method of confinement was used to fabricate the microwire structures studied in Chapter 6 of this thesis, it will be described in more details.

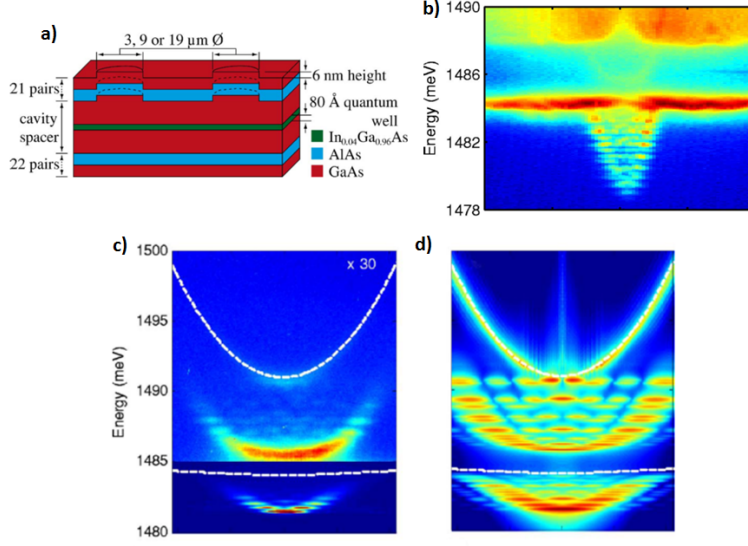


Figure 2.6.2: a) Scheme of the microcavity with shallow mesa pattern etched in the cavity layer, b) spatially resolved photoemission from a $9\mu\text{m}$ mesa, c) k-space polariton emission measured from a $9\mu\text{m}$ mesa and d) corresponding simulated polariton intensity (source: [92]).

Spontaneous formation of 1D polariton condensate has been reported in 2010 by E. Wertz [99]. The 1D microwire structures used in the experiment were obtained by using electron-beam lithography and reactive ion etching from the high quality GaAs microcavity sample. The wires are long in one direction, whereas their width is very small ($200\mu\text{m}$ long and $2 - 4\mu\text{m}$ wide in experiment [99]), what makes them an intermediate case between planar cavities and fully quantized zero-dimensional structures (figure 2.6.3a).

In such structures, the in-plane translational invariance of polaritonic states disappears, leading to the lateral quantum confinement of polaritons and formation of 1D sub-bands [93, 94]. Although the lateral size of the wires is very small, it is still much larger than the exciton Bohr radius, which implicates that excitons remain described by a two dimensional density of states and do not undergo lateral quantum confinement. Only light is laterally confined, hence 1D discretized photon modes are coupled to the 2D excitonic states and resulting polaritons have the same dimensionality as the photon modes.

The 1D polariton condensate was generated by a non-resonant excitation. At low excitation powers polaritons were detected along many 1D branches, however, polariton population looked much different at higher excitation powers. Above the threshold, the spontaneous build-up of the polariton condensate at the lowest energy polariton sub-band, close to $k = 0$ occurs. High density excitation results in formation of the dense exciton cloud in the small region of optical pumping. The repulsive interaction of condensed polaritons with this excitonic cloud induces a local blueshift in the area of the excitation spot. Since excitons are generated only in small area and they do not propagate outside the excitation spot due to their relatively large masses, there are no photogenerated excitons apart from the excitation area. The spatially limited excitons and thus spatially restricted blueshift, serves as a source of a force expelling polaritons from the excitation spot. Due to the energy difference between the bottom of the LPB in the area of the excitation and out of it, polaritons get accelerated, gain kinetic energy and can freely propagate along the wire (figure 2.6.3b). The measurements of the interference patterns above the pump threshold revealed formation of a spatial coherence of the polariton condensate, which extends along the whole wire. Moreover, the microwire is excited near its end, the wire end acts as an infinite potential barrier, which, together with the potential barrier formed by the excitation spot gives a rise to formation of the trap with 0D polariton condensate (figure 2.6.3c) [99, 100].

Similarly, by etching square micropillars with sizes reduced in both planar directions, polariton confinement into 0D state can be obtained.

It has been shown [100] that the excitonic reservoir forming in the area of the non-resonant excitation spot induces a local potential maximum. Contrary to the microwires described above, where repulsive interactions lead to the prop-

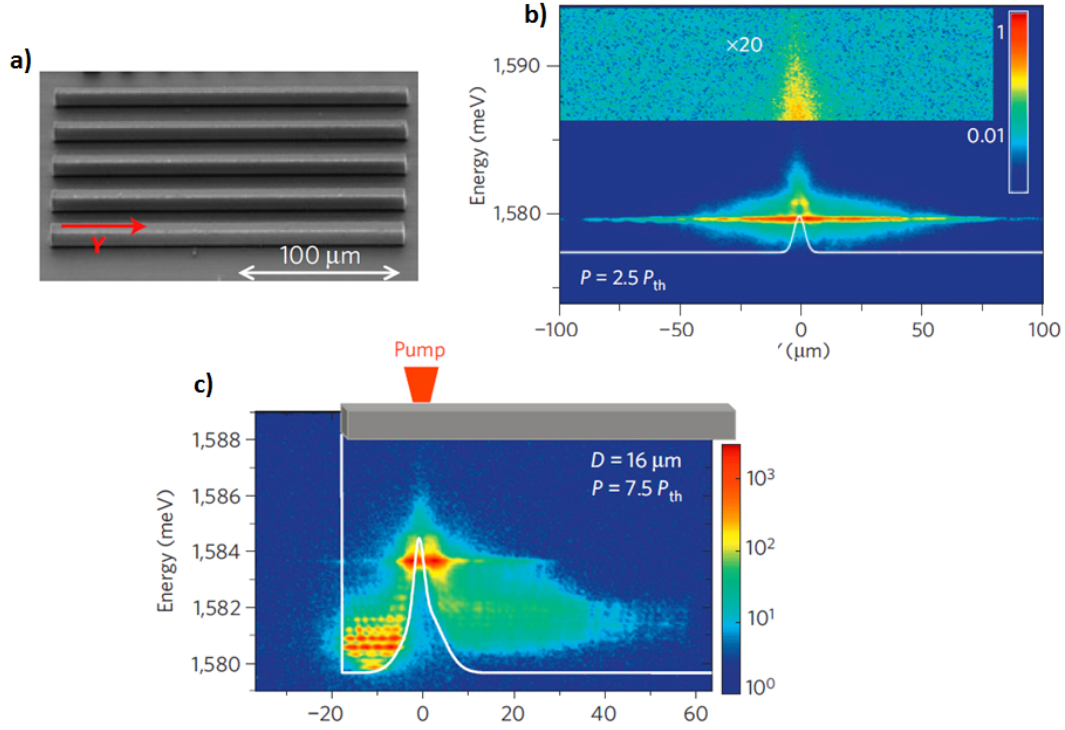


Figure 2.6.3: a) Image of a microwires from a scanning electron microscope, b) Real-space distribution of the intensity along the wire measured at pump power above threshold. The white line shows the resulting potential and the magnified panel at the top shows high-energy exciton reservoir. c) 0D optical trap, forming when the excitation spot is located near the end of the wire - the white line shows the potential (source: [99]).

agation of the condensate along the wire, in 0D case the condensate is pushed away from the centre of the excitation spot and accumulates in four corners of the micropillar. Figures 2.6.4c-e show spatial distribution of the polaritons at different excitation powers. Below the threshold polaritons occupy area around the excitation spot, with the maximum intensity at the centre of the spot. At the threshold polaritons still occupy centre of the pillar, but the polaritons-free hole in the centre of the intensity distribution begins to form. Finally, high above the threshold polaritons are expelled into corners of the micropillar and the condensate wave function vanishes in the centre of the pillar.

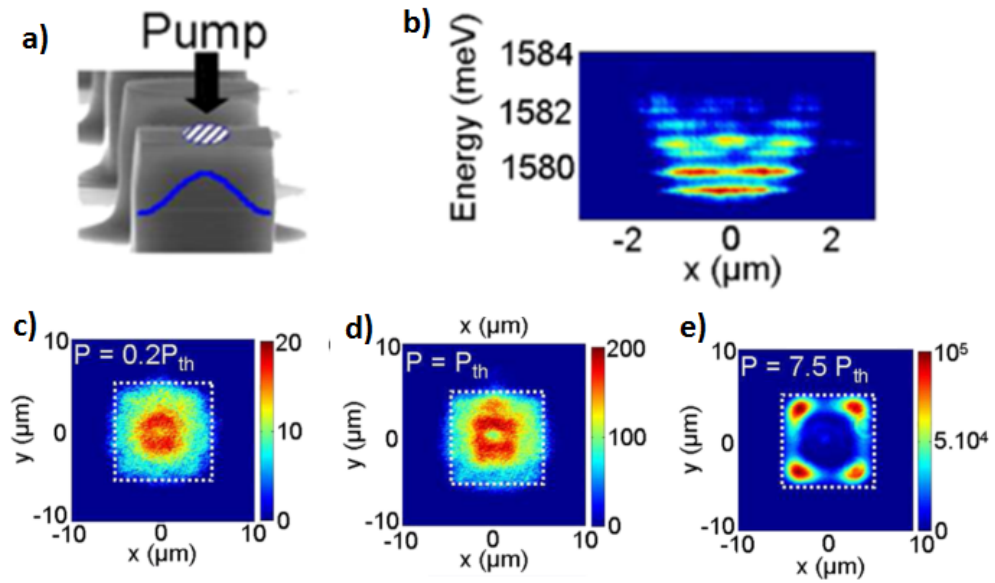


Figure 2.6.4: a) Image of a micropillar from a scanning electron microscope, b) spatially and spectrally resolved photoemission from a $5\mu\text{m}$ micropillar at pumping energy below the threshold, c)-e) spatial distribution of the intensity of the photoemission from a $10\mu\text{m}$ micropillar, measured at powers below threshold, at the threshold and above threshold (source: [100]).

Chapter 3

Experimental techniques

The majority of experiments presented in this thesis rely on the measurement of emission from the microcavity samples and investigating behaviour of polaritons in strong coupling regime. In each of presented experiments different samples were used, and therefore their structures are described in adequate chapters. All these structures differ in the number of DBRs, number of quantum wells and dimensionality, however, what they have in common is that these are all GaAs-based microcavities.

In GaAs-based samples, the strong coupling regime can be observed only at low temperatures, thus all the measurements were carried out in cryostats. There were two kinds of cryostats that we used in our experiments: a continuous flow helium vapour cryostat with optical access and a bath cryostat with magnet cooled by helium. In experiments described in chapters 4 and 6 the first type was used, whereas in experiment from chapter 5 we used a set of two cryostats. In the latter, the sample was placed in a flow cryostat, which was then inserted in the middle of the bath cryostat, where strong magnetic field was created. In our laboratory we have also a bath cryostat with optical access (without a magnet), which I was using during my PhD in experiments on vortices - they are, however, not included in this thesis.

Depending on the character of the experiment, the sample can be measured either in bath or in continuous flow cryostat. Continuous flow cryostat is connected to the liquid helium storage dewar during the experiment and evaporating helium in the cryostat is continuously removed and replaced by new flowing from the dewar, transferred via transport tube. Bath cryostats are very similar to vacuum flasks – they consist of shields, insulating the inside of the cryostat from the room environment to maintain a very low temperature in the main chamber (where the sample or magnet is placed - depending on the type of the cryostat). On top of vacuum shield around the bath chamber, which is widely used in common vacuum flasks, there is an additional shield filled with liquid nitrogen (77K), improving the insulation.

In bath cryostats helium is not replenished during the experiment like in continuous flow cryostats, but the helium shield is filled once a day (in our case) and from there it enters the sample chamber from where it evaporates and is removed from the cryostat via the system of return line. In both cryostats sample is placed on the copper metal sample holder and glued with a latex-based rubber glue.

There are pros and cons of using any of these cryostats. In continuous flow cryostats we can freely change the temperature on the sample from around 4.2 K up to room temperature by adjusting the flow of the liquid helium. They have also much smaller sizes than bath cryostats, since they do not need to store amount of liquid helium required for day long measurements. Liquid helium is stored outside in large storage dewar, which facilitates measurements – it is very quick to cool the sample down and then to heat it up to the room temperature, which is essential when we need to measure many samples the same day. In case of the bath cryostats warming up the sample as well as cooling it down takes much longer time. Operating bath cryostats requires not one but two cryogenic liquids and time consuming pumping of large cryostat in

order to produce a good vacuum inside. It is also much easier to move smaller cryostat in order to change position on the sample of incident light. A continuous flow cryostat is, however, much less stable than a large bath cryostat. The experimental setup is placed on the optical table, which stabilizes everything what is on its surface by damping the ground vibrations. However, in real life the setup is not fully isolated from the surroundings, since both cryostats are connected to pumping devices and to helium return lines, which introduce mechanical vibrations. The smaller, continuous flow cryostat is more vulnerable to these vibrations due to its size and additional source of contact with the outside in the form of helium transfer tube.

3.1 Imaging

Undoubtedly, one of the most significant features of the exciton-polariton system is that all the desired measurements can be performed via use of optical techniques, which not only is an easy way of obtaining information about the system, but it is also a non-invasive technique. All these optical measurements are possible thanks to the relation between the in plane k_{\parallel} vector and the angle of emission with respect to the normal incidence Θ . Photons escaping from the cavity carry the full information about the polariton particle that they formed. The measured intensity corresponds to the density of polaritons, recorded energy is the same as energy of the polaritons, the polarization of the measured photons is the same as the polarization of polaritons and the angle of emission gives the wave-vector of the particles. This means that all we need to do, in order to investigate the polaritons inside the microcavity, is to collect and analyse the emitted light.

There are two ways of imaging the condensate emission, allowing measuring spectral or spatial properties and they are described below.

3.1.1 Real space imaging

The incident laser beam is focused on the sample surface with an objective lens of short focal length, which is also used for collecting the photoluminescence signal. The collected light is then sent through the system of mirrors to the imaging lens, focusing the image of the sample surface on the entrance slit of spectrometer. By using additional lenses, placed on the optical path and operating as a telescope, we can magnify the emitted spot to the size of the CCD. It is sometimes desired to measure photoluminescence only from the selected region of the sample and this is possible through placing a pinhole at the image plane – by choosing its diameter, we can spatially filter emission signal. Illustration of the experimental setup for real space imaging is presented in figure 3.1.1a.

3.1.2 k-space imaging

The k-space image is formed on the back focal plane of the emission collection lens. Imaging the Fourier plane requires one more lens of focal length f , compared to the setup used for the real space imaging, which has to be placed at distance f from the Fourier plane. Schematic picture of this experimental setup is presented in figure 3.1.1b. The imaging of the momentum space of polaritonic system is possible thanks to the in-plane translational symmetry. The in-plane wave vector of photon is the same as the wave vector of recombined polariton and escaping the microcavity it carries the information about the momentum space distribution of polaritons inside the microcavity. Each angle of emission corresponds to a different point in Fourier plane and the relation between the wave vector k_{\parallel} , the energy E and the angle of emitted light is given by:

$$k_{\parallel photon} = k_{\parallel polariton} = \frac{E}{\hbar c} \sin(\Theta) \quad (3.1.1)$$

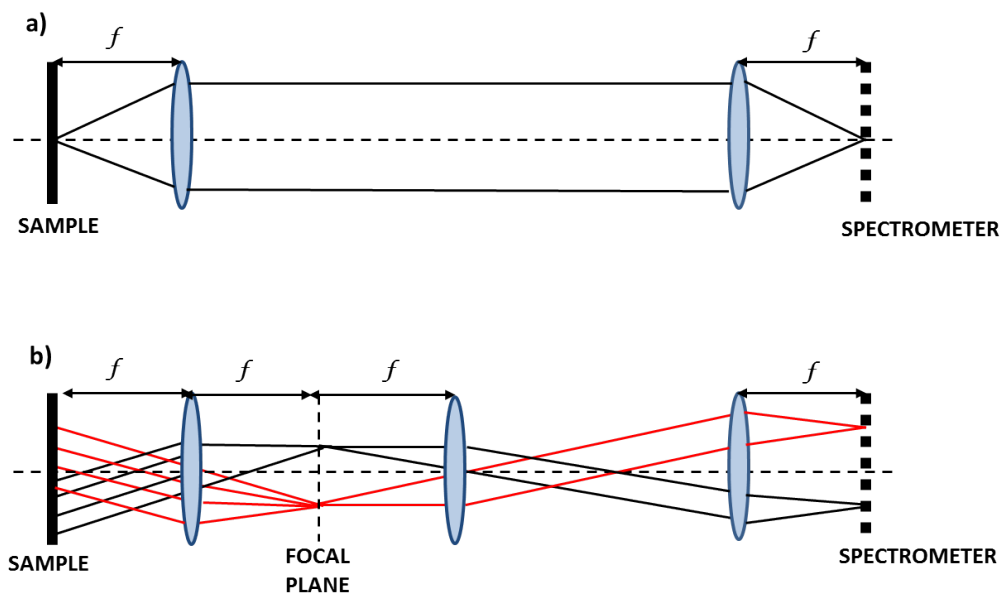


Figure 3.1.1: Imaging of a) real space and b) k-space

3.2 Time resolved measurements

It is not always sufficient to observe only static image of the condensate. In order to observe many physical phenomena like superfluidity, solitons or Bloch oscillations, we need to investigate time evolution of the system. A device allowing us to observe dynamics of the condensate is called streak camera. The incoming light passes through a slit and is focused on the photocathode by lenses, where it is converted into a number of electrons proportional to the intensity of the incident light. They are then accelerated passing through the pair of accelerating electrodes. When the electrons travel between a pair of sweep electrodes, a high voltage, changing in time and synchronized with in-

cident light is applied to the electrodes. As a result of high-speed sweeping, the electrons leaving the sweep electrodes are directed in slightly different angles, depending on the time they arrived at the electrodes. Next they enter the micro-channel plate (MCP), where they are multiplied several thousands of times and such amplified electrons hit a phosphor screen, where they are converted back into light. The image recorded from the phosphor screen with a CCD camera is the spatially and time resolved image of the condensate, with x-axis serving as the position, corresponding to the location of the incident light, and y-axis being the time axis, showing how the emission changes with time (source: Hamamatsu materials).

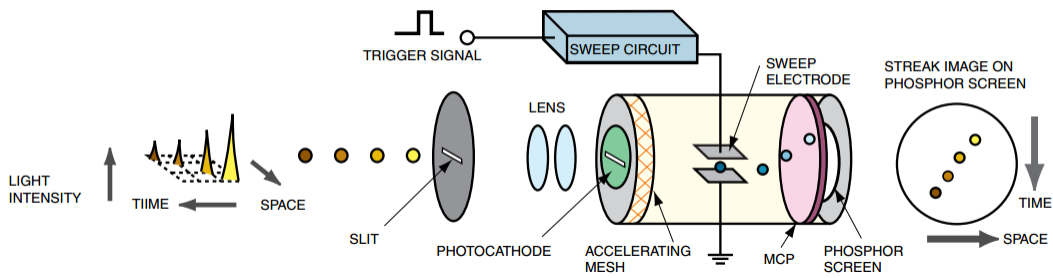


Figure 3.2.1: Scheme of the streak camera (source: Hamamatsu materials)

Chapter 4

Suppression of cross-hatching disorder in GaAs/AlAs microcavities

4.1 Background

The multiplicity of physical phenomena observed in polaritonic systems, like superfluidity or condensation, makes microcavities suitable for the development of devices performing all-optical signal processing [102, 103]. However, the in-plane disorder present in currently available microcavity samples is a major obstacle to devices realization, since it significantly limits length of polariton propagation to a few microns due to localisation. This disorder arises due to the lattice mismatch between components, resulting in strain relaxation. In this chapter we show that fabricating microcavity samples with reduced content of aluminium in the DBRs, and with reduced indium content in quantum wells leads to suppression of strain relaxation.

Invention of molecular beam epitaxy (MBE) in the late 1960s inaugurated the

golden age of device engineering, making possible to grow structures with the precision of one monolayer. The most commonly used materials are $Al_xGa_{1-x}As$ and $GaAs$, both crystalizing in the zinc-blende lattice structure, due to the good lattice match between AlAs and GaAs, being only 0.14% at room temperature, and remaining good for any concentration of the aluminium. On the other hand, the Al concentration strongly influences the band gap of the structure – whereas GaAs has a direct band gap ($E_g(T) = 1,424eV$), the band gap of AlAs is indirect. For Al concentration $x > 0,45$, the band gap of $Al_xGa_{1-x}As$ is indirect, for $x < 0,45$ the band gap is direct and is given by Vegard's law as the function of concentration:

$$E_g = (1,424 + 1,247x)eV^{[101]} \quad (4.1.1)$$

The band gap energy changes with the temperature and this dependence is given by the Varshni equation [104]:

$$E_g = E_g(0) - \frac{\alpha T^2}{\beta + T} \quad (4.1.2)$$

Where $E_g(0)$ denotes band gap energy at $T = 0K$, α and β are material characteristic constants. As the result of different energy gaps between two used materials, the band structure discontinuity occurs at the interface, acting as a barrier.

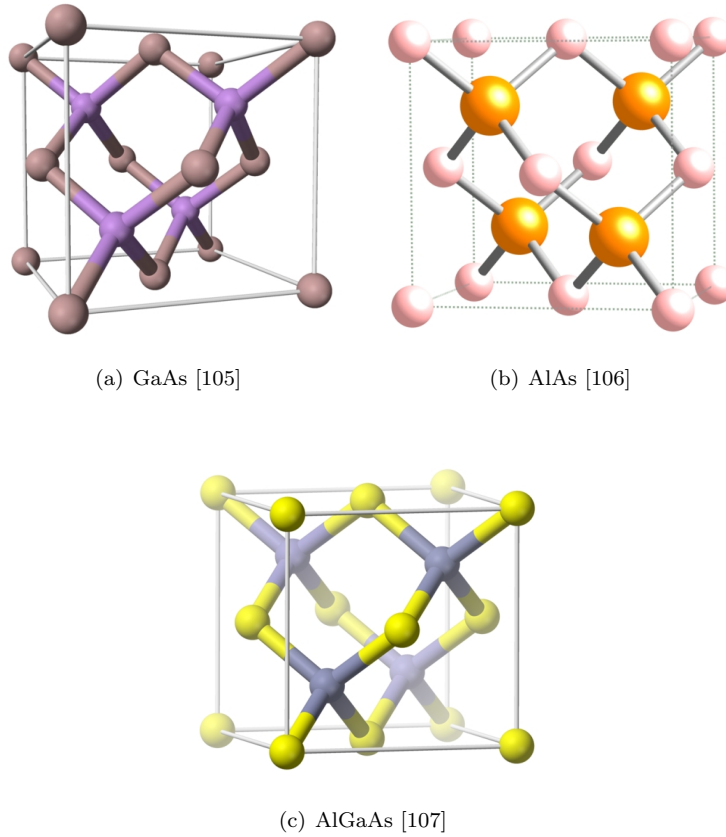


Figure 4.1.1: Scheme of the cubic cells of GaAs, AlAs and AlGaAs

Fabricating heterojunctions of high-quality demands use of materials with almost perfectly matching lattice constants as well as the symmetry of the nets. The alloy system of $GaAs$ and $Al_xGa_{1-x}As$ is the most common along III-V heterostructures due to the pretty good match of lattice constants between two compounds. The lattice parameter mismatch between $GaAs$ and $Al_xGa_{1-x}As$ is less than 0.15% at room temperature [108]. Lattice constants as well as thermal expansion coefficients for bulk materials are presented in table 4.1.

Parameter	$GaAs$	$Al_xGa_{1-x}As$
Lattice constant a (\AA)	5.6533	$5.6533+0.0078x$
Thermal expansion coefficient α_{th} ($\times 10^{-6} \text{ } ^\circ C$)	6.4	$6.4-1.2x$

Table 4.1: Lattice constants and thermal expansion coefficients of studied semiconductors

Even small lattice mismatch between two adjacent layers or growth-related imperfection sums up in a heterostructure consisting of large number of layers, leading to the strain accumulation. Above some critical thickness this strain relaxes, forming misfit dislocations - a characteristic cross-hatch pattern. The presence of dislocations in heterostructures can be attributed to one of the following, fundamental mechanisms:

- Lattice mismatch (different lattice constants of two materials)
- Coefficient of thermal expansion mismatch (different coefficients of thermal expansion of two materials, introducing additional strain with changing the temperature)
- Growth-related defects (mainly arising from surface contamination)

Having alternating layers of two materials with different surface energy, the layers with higher surface energy tend to pile up in islands in order to lower the energy.

As the perfect misfit dislocation is regarded a plain edge dislocation, with the Burger's vector located at the interface between two materials. This dislocation is the most beneficial, as it results in relaxation of the strain at minimum dislocation line energy. Such a strain relaxation should take place on, so called, glide plane (plane spread by the Burger's vector and the line vector), which for zinc-blende structure is the $\{111\}$ plane - not so favourable to grow on for most semiconductor films. Most of the semiconductors, including GaAs and AlAs, grow on $\{001\}$ planes and this is their interface. Whereas for the pure edge and screw dislocations an angle between the Burger's vector and the line vector are 90° and 0° , respectively, dislocations in heterojunctions grown on $\{001\}$ planes are mixed dislocations. In this case the angle between the Burger's vector and the dislocation line θ and the angle between the Burger's vector and the line in the plane of interface, being perpendicular to the dislocation line ϕ , are equal $\theta = \phi = 60^\circ$. These dislocations are often called the 60° dislocations [109].

It is worth to mention that it has been showed that for some materials, for example Ge_xSi_{1-x} , Ge/Si and GaAs/Si grown on Si(001), the increase of the film thickness [110] or concentration of Germanium [111] entailed change of the dislocation character from being 60° to 90° .

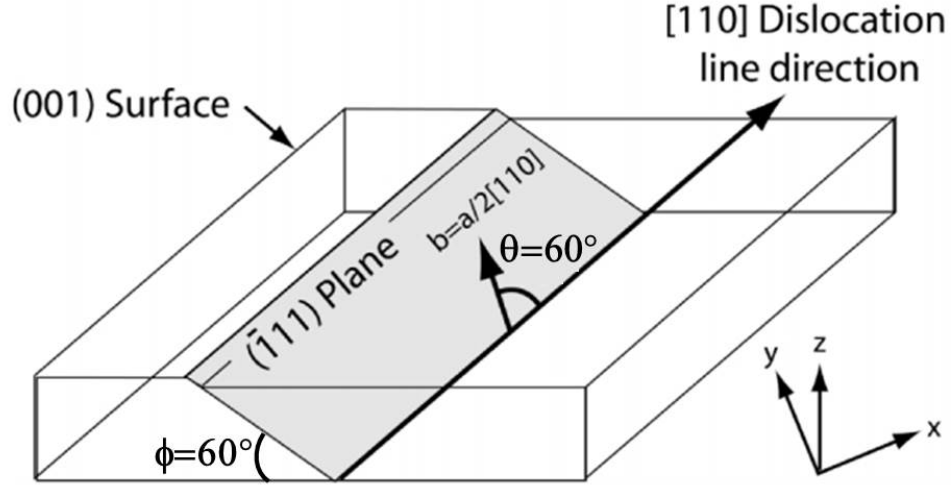


Figure 4.1.2: A scheme of the geometry of a 60° dislocation (source:[109]).

First attempts to calculate the critical thickness were undertaken by Frank and van der Merwe in 1949 [112], however, the explanation of physics behind formation of the cross-hatches and calculation of critical thickness that are currently standard models were described by J. W. Matthews and A. E. Blakeslee in 1974 [113]. They used TEM and SEM to examine $GaAs/GaAs_{0.5}P_{0.5}$ grown epitaxially on GaAs(001), with lattice mismatch of 1.8%, and observed cross-hatches arising in the directions parallel to the $\{110\}$ and $\{1\bar{1}0\}$. In order to calculate the critical thickness they considered two dislocation line forces: F_ϵ – imposed by the misfit strain and F_l – the tension in the dislocation line, which are given by:

$$F_\epsilon = \frac{2G(1+v)}{(1-v)}bh\epsilon\cos\theta \quad (4.1.3)$$

$$F_l = \frac{Gb^2}{4\pi(1-v)}(1 - v\cos^2\phi)(1 + \ln\frac{h}{b}) \quad (4.1.4)$$

Where G is the shear modulus of the substrate and the film, v is the Poisson ratio, b is the magnitude of the dislocation Burger vector, $f = (a_s - a_f)/a_f$ is the misfit strain with a_s and a_f being the lattice constants of the substrate and the film respectively. The strain can have maximum value $\epsilon_{Max} = 0.5f$ and for $F_{\epsilon_{max}}$ we can distinguish two regimes:

- $F_{\epsilon_{max}} < 2F_l$ - the interfaces between layers will be coherent
- $F_{\epsilon_{max}} > 2F_l$ - movement of the dislocations, which will result in reduction of the strain and destruction of the coherence of the interfaces between layers.

Solving $F_{\epsilon_{max}} = 2F_l$ for h will give us the critical thickness h_c :

$$h_c = \frac{b}{2\pi f} \frac{(1 - v\cos^2\theta)(1 + \ln\frac{h_c}{b})}{(1 + v)\cos\phi} \quad (4.1.5)$$

Using this equation for calculating critical thickness of AlAs film grown on GaAs substrate at $T = 600^\circ C$ (where the Poisson ratio of AlAs $v = 0.324$ [114], $b = a/\sqrt{2}$ and $\theta = \phi = 60^\circ$), we obtain $h_c \sim 0.5\mu m$. Since in the microcavities we do not deposit a single AlAs layer on the GaAs substrate, but a stack of AlAs/GaAs pairs of layers forming DBRs, it seems to be more relevant to treat AlAs/GaAs DBR as the layer, by using their average lattice constant in order to calculate the critical thickness. With this approach, the resulting critical thickness $h_c \sim 1\mu m$, which is twice as much as in the case of pure AlAs film. If the film is relaxed completely, then the density of misfit dislocations per unit area $\rho_{MD}^{relaxed}$ multiplied by $b\cos\phi$ equals the misfit strain [115]:

$$\rho_{MD}^{relaxed} b\cos\phi = f \quad (4.1.6)$$

For films with thicknesses exceeding the critical thickness h_c , the equilibrium linear misfit dislocation density depends on the film thickness and can be defined as [116]:

$$\rho_{MD}^{eq} = \frac{f}{bcos\phi} \left(1 - \frac{h_c}{h} \right) \quad (4.1.7)$$

The actual density of misfit dislocations is almost always lower than that given by the equation and $\rho^{actual} \leq \rho_{MD}^{eq} < \rho_{MD}^{relaxed}$. The degree of strain relaxation R can be calculated as:

$$R = \frac{\rho_{MD}^{actual}}{\rho_{MD}^{relaxed}} \quad (4.1.8)$$

For a GaAs/AlAs $4\mu m$ thick film we obtain:

$$\rho_{MD}^{relaxed} \sim 3.6/\mu m \quad (4.1.9)$$

$$\rho_{MD}^{eq} \sim 2.7/\mu m$$

which is much higher than the measured density of misfit dislocations $\rho^{actual} \sim 1.5/\mu m$, giving the degree of strain relaxation $R = 42\%$.

Another approach for calculating the critical layer thickness h_c was proposed by R. People and J.C. Bean [117] in 1985. They assumed that only the energy balance determines occurrence of the misfit dislocations, not mechanical balance like in the Matthews-Blakeslee model.

In this model the critical layer thickness can be calculated by equating the strain energy density and the energy density associated with an isolated screw dislocation:

$$h_c \simeq \left(\frac{1-v}{1+v} \right) \left(\frac{1}{16\pi\sqrt{2}} \right) \left[\frac{b^2}{a(x)} \right] \left[\left(\frac{1}{f^2} \right) \ln \left(\frac{h_c}{b} \right) \right] \quad (4.1.10)$$

where $a(x)$ denotes the bulk lattice constant of the film with x being the aluminium content in $Al_xGa_{1-x}As$ in our case.

The People-Bean model is seen as more accurate in case of the structures with low misfit ($f < 0.5\%$), grown on high-quality substrates.

Using the material parameters relevant to our structures, the critical thickness obtained via this model is calculated as $h_c \sim 50\mu m$.

The two values of the critical thickness, obtained via applying different models, show a striking discrepancy. For that reason we did not rely on the results of the above calculations during the sample design process, but rather systematically varied sample growth parameters.

4.1.1 Impact of microcavity QWs on the disorder phenomenon

The number of quantum wells in a microcavity structure plays a crucial role in forming polaritons. It is important to have a high number of quantum wells, as they increase the optical gain and allow achieving the strong coupling between light and matter. Since the coupling strength is proportional to the square root of number of quantum wells $V \sim \sqrt{N_{QW}}$ [118], the number of quantum wells is desirable to be as high as possible. However, on the other hand, the lattice mismatch between quantum well and the microcavity spacer introduces additional strain to the structure, which may lead to a further build-up of misfit dislocations, and therefore number of quantum wells should be carefully selected. In order to operate properly, the quantum wells must have energy gap smaller than the energy gap of the surrounding material and the barriers

between neighbouring wells should be thick enough in order to avoid overlap of carriers' envelope functions. Another important issue impacting the quality of quantum wells is the growth condition. Quantum wells are affected by disorder coming mainly from the fluctuations of the width and alloy in quantum wells. Such a disorder results in the, so called, inhomogeneous broadening, enhancing the light scattering and leading to the broadening of exciton linewidth and shifting the emission peaks towards lower energies [119, 120]. In InGaAs/GaAs quantum wells the main mechanism of forming inhomogeneous broadening is the indium segregation effect, caused mainly by the different binding energies between GaAs and InAs [121]. This effect relies on the exchange of Ga and In atoms between the substrate and epilayer, so the most weakly bound group III element (In in this case) segregates at the alloy surface and the free energy of the system can be minimized [122]. During this experiment we were using InGaAs/GaAs quantum wells microstructures with indium fraction 4% and 6%, corresponding to the lattice mismatch of 0,2% and 0,4% respectively.

4.1.2 Disorder in polaritonic systems

The impact of structural disorder on optical properties in microcavity structures has been the subject of intensive studies over the past years [123, 124, 125, 126, 127, 128, 129, 130]. Due to the presence of disorder, which breaks the in-plane translational invariance, the k vector is no longer a good eigenstate [131] and polaritons can scatter in all directions.

The structural disorder in microcavities was first revealed in resonant Rayleigh scattering measurements (RRS) [125], which is the coherent component of the secondary emission, occurring only due to disorder [132] and in microcavities it appears in the form of ring pattern in the angular distribution of RRS emission. Since it is a coherent scattering, the ring emission is structured in a speckle pat-

tern. Bright speckles appear in symmetric pairs (with the angle 180° between two paired speckles) and are aligned along the axes $[110]$ and $[1\bar{1}0]$ - the same as directions of cross-hatches [130]. The RRS ring from work of M. Abbarchi et al. [130] can be seen in figure 4.1.3.

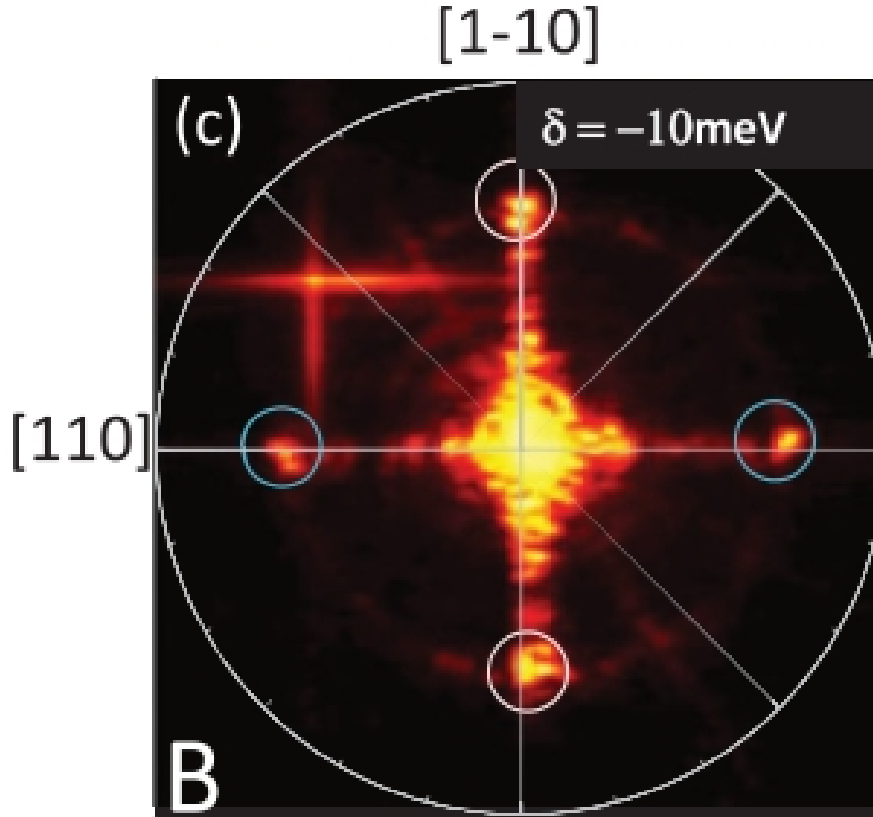


Figure 4.1.3: RRS image of a λ GaAs/AlAs microcavity sample with one $In_{0.07}Ga_{0.93}As$ QW with $Q=740$, as measured by M. Abbarchi et al. (source: [130]).

The polariton condensate in the potential landscape modified by disorder can be a very interesting system for studying. In such a system, due to the interplay between the disorder potential, flow of polaritons and decay of the non-equilibrium condensate, quantized vortices may occur spontaneously [4]. Photonic disorder also allows stable vortex solutions in large pump spot OPOs contrary to the homogeneous samples, where due to the $y \rightarrow -y$ symmetry only pairs of vortex-antivortex solutions are allowed, which are not stable unless the

pump spot is small enough [133]. Another interesting phenomenon is the co-existence of non-equilibrium condensates with long-range spatial coherence in non-equilibrium polariton BEC in CdTe [2] and in OPO in GaAs microcavities [60]. Disorder in polaritonic potential landscape strongly influences the formation of 2D macroscopically occupied polariton states [134]. It was observed by Sanvitto et al. [128] that the disorder govern fluctuations give rise to localization in the polariton distribution. This behaviour can be detected via the measurements of signal emission of the polariton OPO. Their measurements showed that OPO signal was affected by partially ordered fluctuations in the photonic potential. The observed signal consisted of localised emissions mainly aligned along $[110]$ and $[1\bar{1}0]$ directions. The polariton condensate signal, in the presence of strong disorder, breaks up into localized modes emitting at different energies [67]. It was also observed that in case of polariton condensates formed under non-resonant excitation the real space distribution of the signal is also affected and local maxima arise as the result of polariton trapping by the polaritonic potential disorder [60]. Although microcavities with photonic disorder are interesting systems to explore, for studying many physical phenomena, where observing propagation of polaritons over large distances is crucial, disorder is not desirable.

4.2 Experiment

During this work, we have studied many different MBE grown microcavity structures produced in the National Centre for III-V Technologies in Sheffield. In order to show suppression of strain, six of them will be discussed in this thesis.

The motivation of this work was to eliminate cross-hatches from the MBE grown microcavity structures in order to obtain good quality samples with suppressed disorder, allowing observing a propagation of polaritons over large distances. In first part of this section, we investigate microcavity samples, containing AlAs/GaAs DBRs (widely used in microcavity polaritons studies). Large energy fluctuations in photoluminescence measurements as well as cross-hatch pattern on the surface, visible through the Nomarski microscope imaging, clearly indicate stress relaxation. In the second part, we show that reduction of aluminium content in DBRs and reduction of indium content in QWs lead to suppression of strain relaxation.

4.2.1 AlAs/GaAs microcavity structures

Two microcavity samples, containing AlAs/GaAs DBR layers will be discussed in this section. Both samples were grown with rotation, except for the final 2.5 periods of the lower DBR and the lower part of the cavity – up to first quantum well. The growth interruption was introduced in order to form a cavity wedge. Description of the two samples, named VN2181 and VN2160 and the schematic layer structures are given in table 4.2.

VN2181 is a $3/2\lambda$ GaAs/AlAs microcavity sample, grown on GaAs substrate, followed by 200nm GaAs buffer layer and 30 layers of 70.1nm thick AlAs, alternating with 30 layers of 59.5nm thick GaAs layers, forming bottom DBRs.

GaAs cavity spacer was grown with 6 10nm thick 6% InGaAs quantum wells, positioned in the antinode of the cavity mode and separated by a 58.9nm thick GaAs barrier. The top part of the sample is formed by DBRs consisting of 25 alternating layers of AlAs and GaAs of the same thicknesses as in the lower DBRs.

The second sample, VN2160, is a λ GaAs/AlAs microcavity also grown on GaAs substrate, covered by 200nm GaAs buffer. It consists of GaAs cavity, containing 1 8nm thick 4% InGaAs quantum well and surrounded by 21/23 pairs of 69.3 nm thick AlAs and 58.6 nm thick GaAs layers forming DBRs at the top and the bottom, respectively. The images from Nomarski microscope of two AlAs/GaAs microcavities are shown in fig. 4.2.1 and demonstrate a clear evidence of strain relaxation in form of perpendicular cross-hatches. It is also easy to notice, that sample VN2181 has more dense distribution of lines than VN2160, which is expected, since VN2181 has more DBRs and more quantum wells with higher indium content, leading to formation of larger disorder. Surface oval defects visible in both Nomarski micrographs are Ga droplets deposited in the microcavity by the gallium cell during the MBE growth [135]. These point-like defects do not contribute to cross-hatch disorder, but they result in local surface modulation and create zero-dimensional polariton states of narrow linewidths [136, 137]. In later samples they were eliminated by increasing the cell tip temperature and out-gassing.

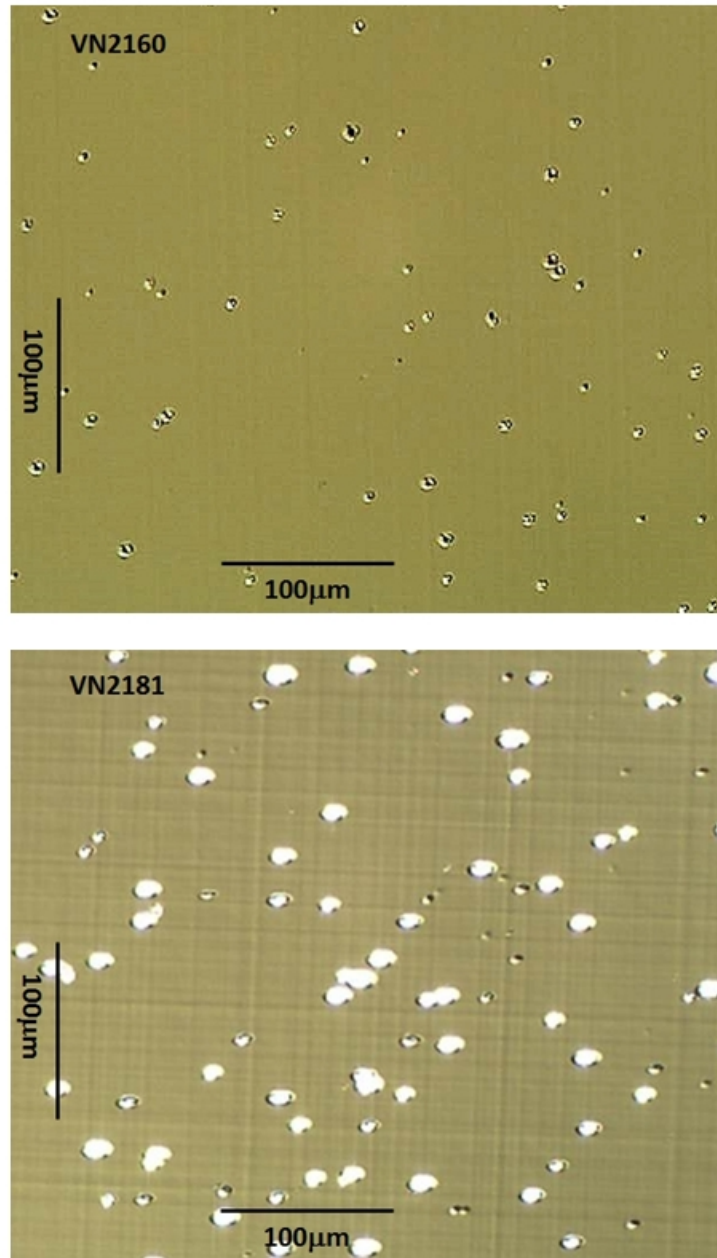


Figure 4.2.1: Nomarski microscope images of the strain relaxed AlAs/GaAs samples VN2160 and VN2181.

Figure 4.2.2 shows images from resonant transmission of samples VN2160 and VN2181. The laser was tuned to be in resonance with $k = 0$ state and transmission was measured for both samples.

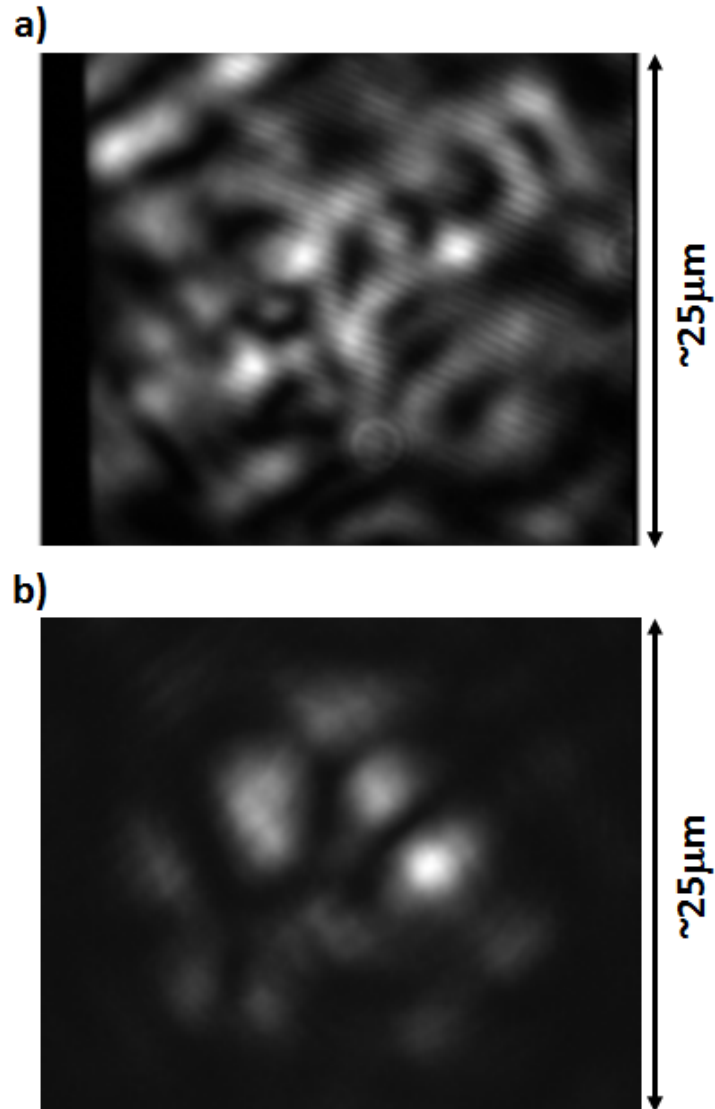


Figure 4.2.2: Resonant transmission images from samples with photonic potential disorder a) VN2160, b) VN2181

All the AlAs/GaAs samples studied by us exhibited strain relaxation in the form of cross-hatches, and therefore they are not good candidates for studying

polariton fluid propagation.

There are few possibilities allowing reducing the stress, and hence disorder in semiconductor microcavities. First one was proposed by A. Mazuelas et al. [138], and it relies on doping GaAs/AlAs distributed Bragg reflectors with C or C and Be. This method is, however, not useful for studying polaritons, since it causes high free carrier absorption, which reduces the lifetime of polaritons, and therefore also the length of propagation is reduced. Another way of reducing strain in microcavity is to use strain-compensating AlP layers into the centre of the low index AlAs layers of the DBRs, which for the concentration of P $x = 1.5\%$ in $AlAs_{0.985}P_{0.015}$ alloy reduces the cross-hatches density by an order of magnitude [139].

In this work we propose reduction of the strain between the epilayer and the substrate through reducing the aluminium content in the AlAs/GaAs structure. We also demonstrate the positive influence of decreasing the number of quantum wells in the microcavity on the suppression of strain.

4.2.2 AlGaAs/GaAs microcavity structures with reduced aluminium content

In this section 85% aluminium *AlGaAs/GaAs* samples with different number of quantum wells will be investigated. Since the number of quantum wells in the microcavity structure introduces additional strain, the first step in order to test the possibility of decreasing misfit dislocations was to fabricate a bare microcavity sample – the sample without embedded quantum wells. We tested 5 bare cavity samples with varying number of DBRs: 15/15, 20/20, 23/23, 23/27 and 27/27 lower/upper $Al_{0.85}Ga_{0.15}As/GaAs$ DBR periods. First three samples showed no evidence of cross-hatching and the last one, with the highest number of DBR periods revealed the very weak beginning of the surface pattern formation. Results obtained with bare $Al_{0.85}Ga_{0.15}As/GaAs$ samples were

very promising and encouraging to further work on designing the microcavity samples with reduced disorder.

$Al_{0.85}Ga_{0.15}As/GaAs$ samples with embedded 1, 3 and 6 quantum wells will be presented and their details can be found in table 4.2.

VN2502 is a 1λ $Al_{0.85}Ga_{0.15}As/GaAs$ sample with 23/27 DBR repeats with thicknesses of $Al_{0.85}Ga_{0.15}As$ and $GaAs$ equal to 69.2nm and 58.3nm respectively. Inside the cavity 1 4% InGaAs quantum well is embedded on the antinode.

Sample called VN2503 is very similar to the previous one, except that it has 2λ cavity with 3 4% InGaAs quantum wells embedded, one well in one antinode. The last sample - SF0450, is also a 23/27 DBR repeats sample, but this time with 6 6% InGaAs quantum wells, located three per antinode in a $3\lambda/2$ cavity.

The surface images taken with the Nomarski microscope are presented in figure 4.2.3. It can be clearly seen, that in case of images from samples with one and three quantum wells, the surface of the structure, which was unrelaxed as a bare microcavity, remains free of any cross-hatches. Sample SF0450, consisting of six quantum wells reveals the presence of the structural relaxation, showing that the number of embedded quantum wells has a strong influence on the quality of the structure and increasing this number leads to the relaxation of the structure, reflected in the appearance of the surface cross-hatches.

There is a huge difference in the observation of OPO photoluminescence in unrelaxed sample, compared to the relaxed one. Figure 4.2.4 shows the measurements of OPO from two samples, allowing seeing variation in the polariton distribution in highly disordered system and in a system where mechanical disorder is suppressed. In figure 4.2.4a particles are confined in the potential minima, corresponding to the alignment of the cross-hatches. We can see that their segregation in the form of net is evident. By contrast, figure 4.2.4b shows a homogeneous polariton distribution in the OPO signal over a distance of the

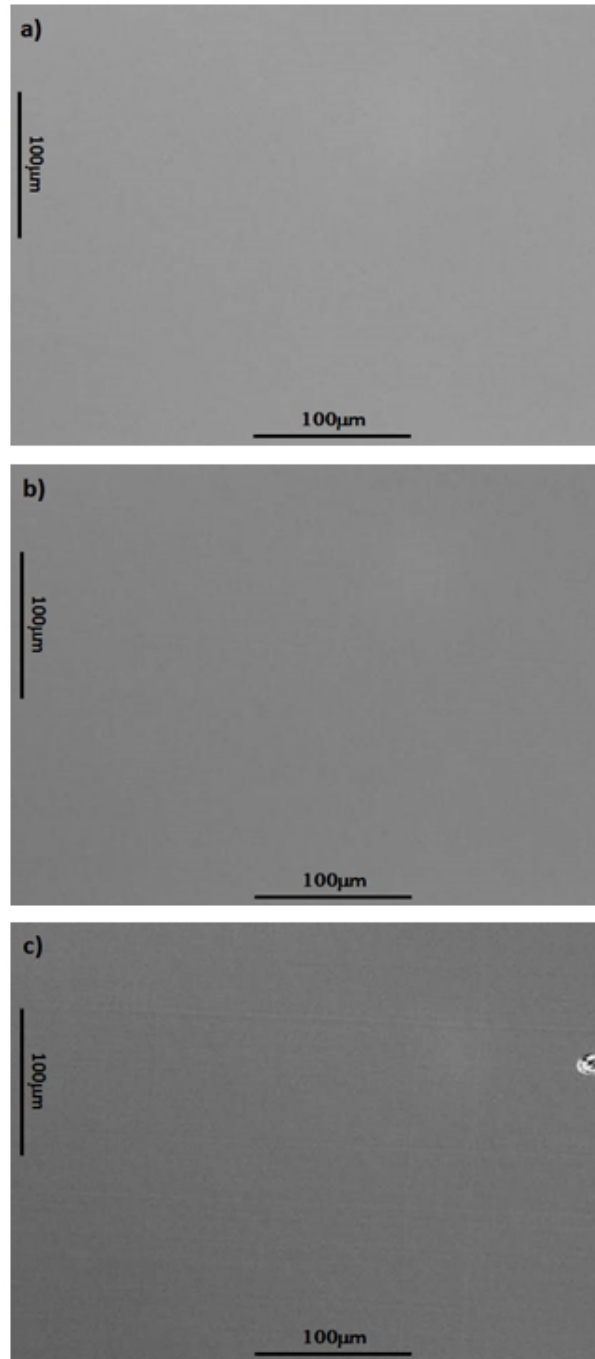


Figure 4.2.3: Nomarski microscope surface imaging of the $Al_{0.85}Ga_{0.15}As/GaAs$ microcavity samples with a) one (VN2502), b) three (VN2503) and c) six (SF0450) InGaAs quantum wells.

order of $100\mu\text{m}$ and no sign of any cross-hatching-like segregation.

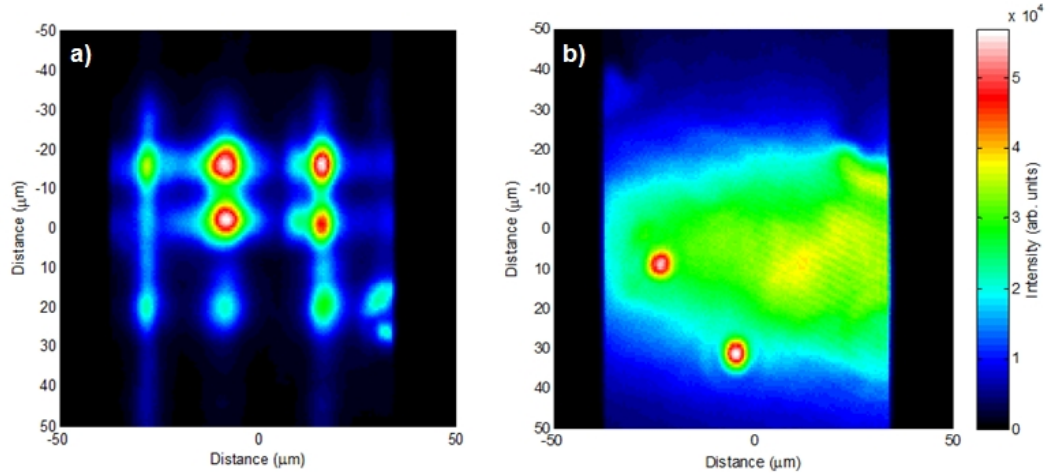


Figure 4.2.4: OPO condensate images of a) relaxed (the most strained VN2181 sample chosen) and b) unrelaxed microcavity samples.

Sample	DBRs layers	DBR pairs (upper/bottom)	QWs (number x In content)	Width of QW	Length of cavity	Relaxed
VN2181	<i>AlAs/GaAs</i>	25/30	6 x 6%	10nm*	$3/2\lambda$	YES
VN2160	<i>AlAs/GaAs</i>	21/23	1 x 4%	8nm	λ	YES
VN2502	<i>Al_{0.85}Ga_{0.15}As/GaAs</i>	23/27	1 x 4%	10nm	λ	NO
VN2503	<i>Al_{0.85}Ga_{0.15}As/GaAs</i>	23/27	3 x 4%	10nm	2λ	NO
SF0450	<i>Al_{0.85}Ga_{0.15}As/GaAs</i>	23/27	6 x 6%	10nm*	$3/2\lambda$	YES

Table 4.2: Details of the microcavity structures used in cross-hatching disorder suppression studies.

*quantum wells are located 3 per antinode and they are separated by a 10nm thick GaAs barriers

4.3 Conclusions

In this chapter we studied AlGaAs/GaAs microcavity structures with two different composition of Al in DBR layers and varying number of InGaAs quantum wells embedded inside the cavity. The samples were characterized with the Nomarski microscope in order to examine the level of strain relaxation, revealing itself by formation of the cross-hatch pattern on the surface of the structure. The magnitude of disorder was also shown in resonant transmission images and the effect of disorder on polaritons propagation was illustrated by OPO condensate images.

First experiments with the GaAs/AlAs structures showed a dense cross-hatching pattern in the Nomarski microscope images as well as a very strong localization of the polaritons in the OPO measurements, indicating a high polaritonic potential disorder. Although in the structure with only one quantum well this behaviour was much weaker than in case of the structure with six quantum wells, it was still very significant.

In the next part of the chapter, we proposed to fabricate the sample with reduced content of Al in order to reduce disorder. At this time the experiments were taken with $Al_{0.85}Ga_{0.15}As$ structures with six, three and one InGaAs quantum wells. The measurements showed that the structures with one and three quantum wells are free of the cross-hatches in Nomarski microscope images and the OPO photoluminescence shows a homogeneous propagation of polaritons over large distances. In case of the structure with six quantum wells, we observed start of the formation of cross-hatches, which is in agreement with the expectations that the increase of the number of quantum wells increases the internal disorder.

Chapter 5

Suppression of Zeeman splitting in non-equilibrium polariton condensate

5.1 Background

Polaritons, formed by heavy-hole excitons, can have two allowed spin projections ± 1 on the structure growth z-axis. Unlike in the bulk structures, where light and heavy holes are degenerate, in quantum well structures degeneration of light and heavy holes at $k = 0$ is lifted. This is due to the quantum confinement in the direction of the structure growth axis in the latter. As a result, energy levels of the heavy holes lie closer to the bottom of the well than light-hole levels, and hence the ground state excitons in quantum wells are heavy-hole excitons. In case of 6% InGaAs quantum wells, considered in this chapter, the splitting between light- and heavy-holes is 26meV [140]. By applying additional in-plane strain this splitting can be further increased or decreased, depending whether the strain is compressive or tensile. The total exciton angular momentum J has projections ± 1 and ± 2 on the structure axis

(figure 5.1.1), however, because photon spin can be only $-1, 0, +1$, to fulfil spin conservation rule, only excitons with spin projections ± 1 can be optically excited. As they do couple to light, they are called bright states, as opposed to excitons with spin projection ± 2 , called dark states, which are not coupled to the photonic modes.

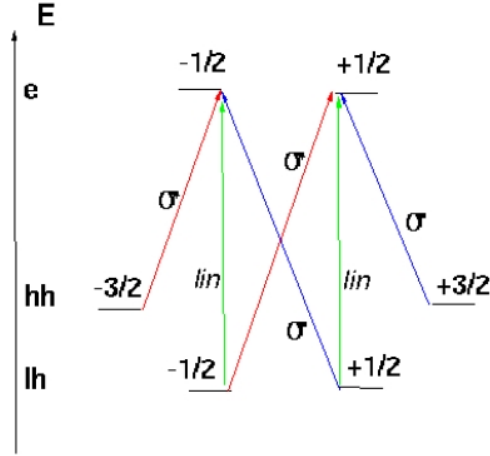


Figure 5.1.1: Polarisation of optical transitions in zinc-blend semiconductor quantum wells. Red, blue and green lines show $\sigma+$, $\sigma-$ and linearly polarized transitions, respectively” (source: [141]).

Excitons, being complex particles follow the spin-relaxation mechanism, and therefore they lose their polarization after some period of time. It has been shown, that the main mechanism responsible for this relaxation in case of the quantum confined excitons in non-magnetic semiconductors is the Bir-Aronov-Pikus mechanism. It allows us neglecting the dark states, hence thinking of exciton as of two level system and describe it by 2×2 spin density matrix, analogical to the spin density matrix for electrons [141].

5.1.1 Spin Meissner effect in equilibrium BEC of polaritons

Owing to the exchange effects, polariton-polariton interactions are strongly spin anisotropic and one can describe polaritons in terms of the strength of the interparticle interactions between polaritons with parallel α_1 and antiparallel

α_2 spin projections. Values of α_1 and α_2 parameters play a very important role in determining the nature of the state of polariton gas. For the equilibrium BEC the phase diagram of a uniform polariton gas in the coordinates of interaction constants α_1 and α_2 can be seen in figure 5.1.2 (both figure and its analysis comes from [142]). Here, depending on the relative strength and sign of these parameters, exciton-polaritons may condense in real or in reciprocal space and the polarization of this condensate may be either linear or circular [143], [2].

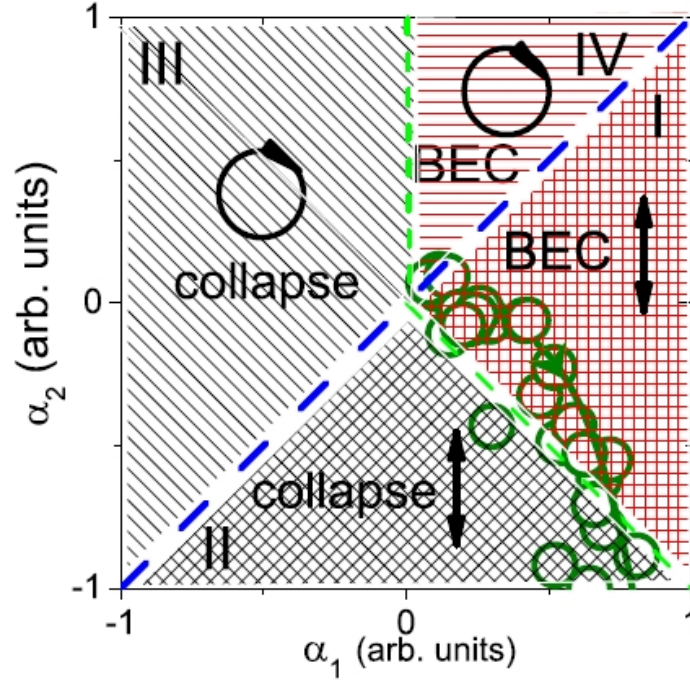


Figure 5.1.2: Dense hatch denotes linear polarization, rare hatch - circular polarization of the polariton gas. Red regions correspond to the reciprocal space condensation, whereas black regions to real space condensation. The circles show the values of interaction constants measured at $400\mu W$ excitation intensity for different values of the exciton-photon detuning. Calculated values of the interaction constants are shown by line. The arrow points the direction, where detuning changes from negative to positive [142].

Free energy of the exciton polaritons, which should be minimized at equilib-

rium, can be expressed in an infinite planar cavity at $T = 0$ as:

$$E_F = -\mu N + \frac{\alpha_1 + \alpha_2}{4} N^2 + (\alpha_1 - \alpha_2) S_z^2 \quad (5.1.1)$$

where μ stands for the chemical potential, N is the concentration of polaritons and S_z is defined via the circular degree of the condensate as $\rho_c = 2S_z/N$. We can distinguish different regions of the α_1, α_2 diagram, concerning the sign of α_1 , $\alpha_1 + \alpha_2$ and $\alpha_1 - \alpha_2$:

- if $\alpha_1 - \alpha_2 > 0$, then free energy is minimized for $S_z = 0$ therefore, polaritons in this region are linearly polarized. Such a situation is depicted as a dense hatched region in fig. 5.1.2. The energy shift of the polariton gas can be found by minimizing of the free energy over concentration:

$$E_{lin} = \mu = \frac{\alpha_1 + \alpha_2}{2} N \quad (5.1.2)$$

and minimum of the free energy is achieved for one of the extreme value of the polariton concentration N , depending on the sign of $\alpha_1 + \alpha_2$

- if $\alpha_1 - \alpha_2 < 0$, then free energy is minimized for $S_z = \pm N/2$ and, therefore, the polariton gas is circularly polarized. This situation is depicted as rare hatched regions in fig. 5.1.2. Polariton energy is shifted by:

$$E_{circ} = \mu = \alpha_1 N \quad (5.1.3)$$

In this case the free energy is minimized depending on the sign of α_1

In the absence of external magnetic field, there is equal number of left and right circularly polarized polaritons in the system, as this equality minimizes the energy of the polariton system, thus, without applied magnetic field the system is linearly polarized ($\alpha_1 > \alpha_2$). Applying magnetic field strongly influences excitons in quantum wells, thus also polaritons are affected. We can distinguish two different cases of the polariton system in the presence of magnetic field,

depending on its value. If we apply weak magnetic field, the light emitted by the cavity will no longer be linearly polarized. It will have circularly polarized part, hence will be elliptically polarized. In this region magnetic field only changes the polarization of the emitted light and the shift towards lower energy due to the Zeeman effect is compensated by the blueshift resulting from the polarization. However, with further increasing of the magnetic field, above some critical value, the strength of the magnetic field overcomes the strength of polariton-polariton interactions. At this critical magnetic field the condensate becomes fully circularly polarized and the Zeeman effect can be observed in the emitted light [144]. This behaviour, referred to as spin Meissner effect, has been theoretically predicted to occur in thermal equilibrium Bose-Einstein condensate of microcavity exciton polaritons by Rubo et al. [144].

5.2 Experiment

The suppression of the Zeeman splitting in the presence of magnetic field is a well-known property of equilibrium exciton-polariton condensate in semiconductor microcavities [144]. In this chapter we show experimentally that a similar effect takes place in a non-equilibrium polariton condensate arising from polariton parametric scattering. Although the observed phenomenon is qualitatively similar to the spin Meissner effect, its physical origin is different. We explain this behaviour in terms of a phase synchronization of spin-up and spin-down polarized polariton condensates, resulting from a nonlinear coupling via the coherent pump state.

5.2.1 Sample structure and experimental setup

The object of our studies was a GaAs microcavity sample with three 6% In-GaAs quantum wells. The sample was placed in a cryostat with optical access

and possibility of measurements in magnetic field. The measurements were performed with magnetic field in the Faraday geometry at 12K and we were varying the angle of incident beam (10° or 15°), pump power and magnetic field (between 0 and 5 T). The sample was excited in a region with 6 meV Rabi splitting and near zero detuning between the exciton and cavity mode, by a linearly polarized tunable multimode Ti:sapphire laser, focused to $\sim 30 \mu m$ spot. The laser was tuned to energies 1.8 and 2.6 meV above the energy of the lower polariton branch at $k = 0$, for two different excitation angles: $\Theta \sim 10^\circ$ and $\Theta \sim 15^\circ$, respectively, which corresponded to energies about 1 meV above the lower polariton state at k_p . This allowed us to excite efficiently the parametric scattering for both $\sigma+$ and $\sigma-$ polarized modes.

5.2.2 Magnetophotoluminescence spectra in OPO configuration

Figure 5.2.1 shows normalized spectra of polariton emission at $k \sim 0$, obtained for two incident angles at different magnetic fields and excitation power below and above the threshold of stimulated scattering.

Spectra were recorded for two circular polarizations: $\sigma+$ - associated with the lower energy polariton mode (dashed lines) and $\sigma-$ - associated with the higher energy polariton mode (solid lines) in the magnetic field.

Measured spectra were then fitted with Gaussian functions, which allowed us to detect Zeeman splitting as low as $20 \mu eV$.

We observed superlinear increase of both polarized polaritons with excitation power for all magnetic fields, which was due to the macroscopic occupation of the lower polariton ground $\sigma+$ and $\sigma-$ polarized states, occurring as the result of the stimulated polariton-polariton pairs scattering from the pump [6, 7, 145]. Clearly seen shift in energy of about 1.3-1.5 meV between emission below and above the threshold of stimulated scattering arises from the polariton-polariton interactions between pump, signal and idler states.

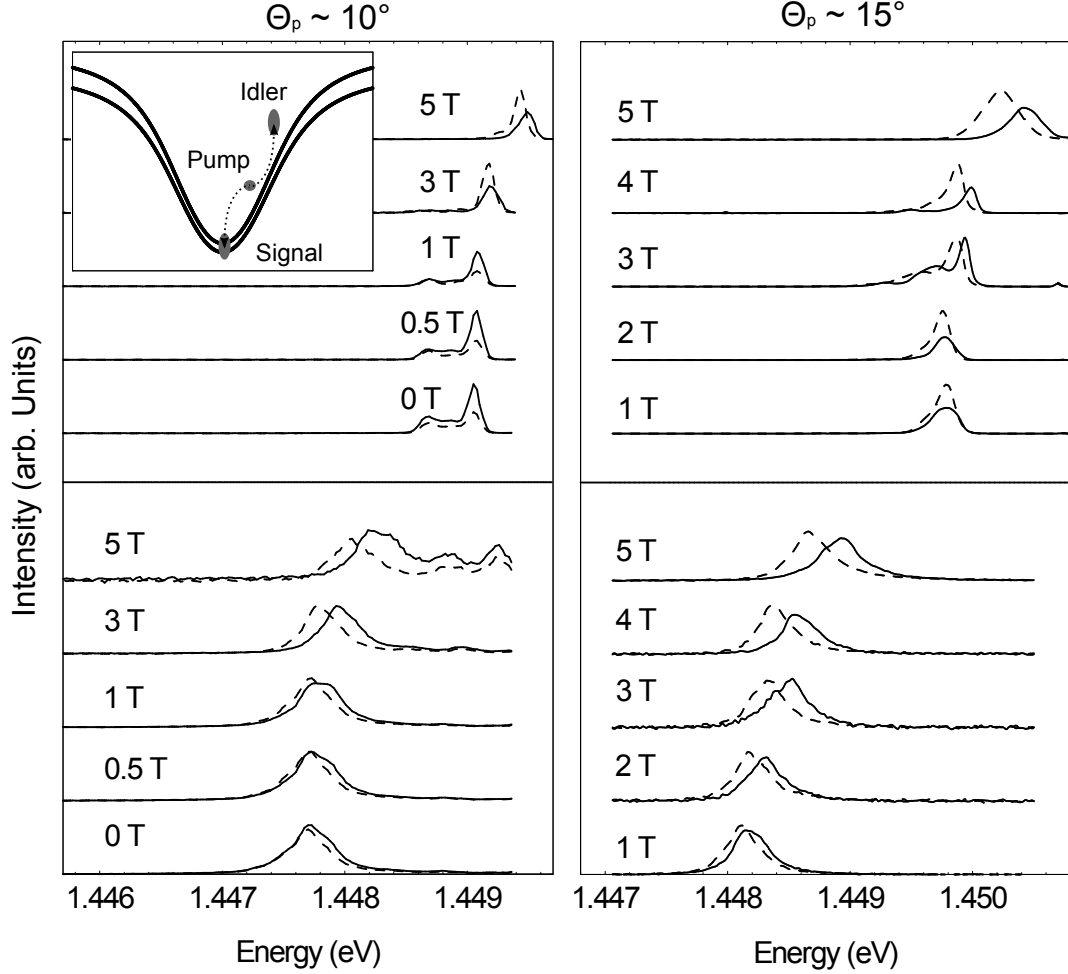


Figure 5.2.1: Spectra of polariton emission at $k \sim 0$ recorded in two circular polarizations, $\sigma+$ (dashed lines) and $\sigma-$ (solid lines), for various magnetic fields below (lower panels) and above (upper panels) the threshold of stimulated scattering. The inset shows a schematic diagram illustrating the polariton levels and the pump, signal, and idler states.

We measured $\sigma+$ and $\sigma-$ polarizations for two angles as a function of pump power and magnetic field, recording the strongest individual modes for both polarizations. The results with splitting between two polarizations are presented in figure 5.2.2.

For the excitation angle 10° , at low magnetic field the splitting between two polarizations first slightly decreases, to fall steeply to zero with further increase of pump power. Similar behaviour can be observed for higher magnetic field, however in this case the splitting is only partially quenched. In turn for the

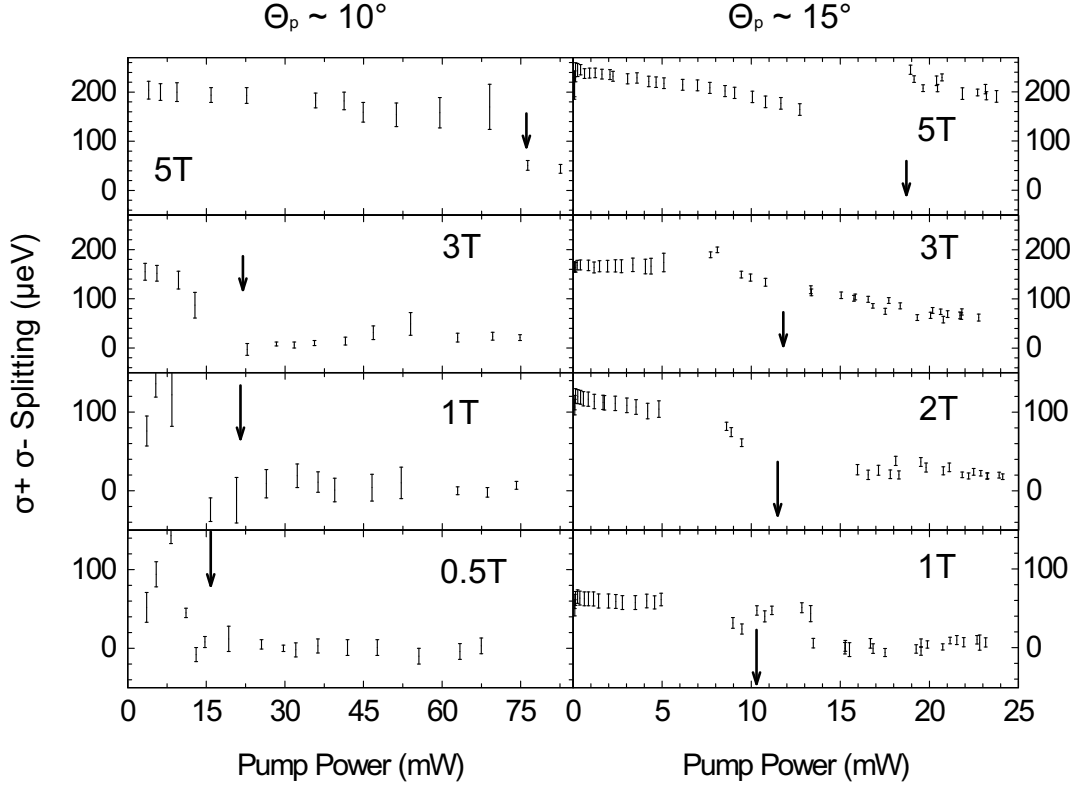


Figure 5.2.2: Dependences of Zeeman splitting on pump power for various fields at both excitation angles. Vertical arrows indicate powers at which onset of stimulated scattering occurs.

larger angle (15°), full quenching was observed for magnetic field below 1 T only, and for 5 T we did not observe any quenching at all.

5.3 Theoretical model

Theoretical model, explaining experimental results, was proposed by T.C.H. Liew and A.V. Kavokin. To explain origin of the observed phenomena, we compared our system with the system of two Josephson coupled polariton condensates described by Wouters [146]. If we have two condensates coupled coherently, then, due to the coherent transfer of polaritons between condensates, their phases may be synchronized. In our experiment, the coherent coupling between two signal states is possible thanks to the polariton-polariton scattering from the pump. When the spin flip of polaritons in signal and idler or

signal and pump states occur at the same time, there is a coherent transfer of signal polaritons between spin-up to spin-down states, which allows a phase locking between these two states, and therefore it is possible to reach the state of a single, elliptically polarized condensate of polaritons. These effects can be described by coupled equations for the polarized pump ($\Psi_{p,\sigma}$), signal ($\Psi_{s,\sigma}$) and idler ($\Psi_{i,\sigma}$) mean fields:

$$\begin{aligned}
 i \hbar \frac{\partial \Psi_{p,\sigma}}{\partial t} = & E_{p,\sigma} \Psi_{p,\sigma} + 2\alpha_1 |X_p|^2 \Psi_{p,\sigma}^* \Psi_{s,\sigma} \Psi_{i,\sigma} \\
 & + f e^{i\omega t} + \alpha_1 |X_p|^2 (|\Psi_{p,\sigma}|^2 + 2|\Psi_{s,\sigma}|^2 \\
 & + 2|\Psi_{i,\sigma}|^2) \Psi_{p,\sigma} + \alpha_2 |X_p|^2 (|\Psi_{p,-\sigma}|^2 \\
 & + |\Psi_{s,-\sigma}|^2 + |\Psi_{i,-\sigma}|^2) \Psi_{p,\sigma} \\
 & + (\Psi_{s,-\sigma}^* \Psi_{s,\sigma} + \Psi_{i,-\sigma}^* \Psi_{i,\sigma}) \Psi_{p,-\sigma} \\
 & + (\Psi_{s,\sigma} \Psi_{i,-\sigma} + \Psi_{s,-\sigma} \Psi_{i,\sigma}) \Psi_{p,-\sigma}^*],
 \end{aligned}$$

$$\begin{aligned}
 i \hbar \frac{\partial \Psi_{s,\sigma}}{\partial t} = & E_{s,\sigma} \Psi_{s,\sigma} + \alpha_1 |X_s|^2 \Psi_{i,\sigma}^* \Psi_{p,\sigma}^2 \\
 & + \alpha_1 |X_s|^2 (|\Psi_{s,\sigma}|^2 + 2|\Psi_{p,\sigma}|^2 \\
 & + 2|\Psi_{i,\sigma}|^2) \Psi_{s,\sigma} + \alpha_2 |X_s|^2 (|\Psi_{p,-\sigma}|^2 \\
 & + |\Psi_{s,-\sigma}|^2 + |\Psi_{i,-\sigma}|^2) \Psi_{s,\sigma} \\
 & + (\Psi_{p,-\sigma}^* \Psi_{p,\sigma} + \Psi_{i,-\sigma}^* \Psi_{i,\sigma}) \Psi_{s,-\sigma} \\
 & + (\Psi_{p,\sigma} \Psi_{p,-\sigma} \Psi_{i,-\sigma}^*),
 \end{aligned}$$

$$\begin{aligned}
 i \hbar \frac{\partial \Psi_{i,\sigma}}{\partial t} = & E_{i,\sigma} \Psi_{i,\sigma} + \alpha_1 |X_i|^2 \Psi_{s,\sigma}^* \Psi_{p,\sigma}^2 \\
 & + \alpha_1 |X_i|^2 (|\Psi_{i,\sigma}|^2 + 2|\Psi_{p,\sigma}|^2 \\
 & + 2|\Psi_{s,\sigma}|^2) \Psi_{i,\sigma} + \alpha_2 |X_i|^2 (|\Psi_{p,-\sigma}|^2 \\
 & + |\Psi_{s,-\sigma}|^2 + |\Psi_{i,-\sigma}|^2) \Psi_{i,\sigma} \\
 & + (\Psi_{p,-\sigma}^* \Psi_{p,\sigma} + \Psi_{s,-\sigma}^* \Psi_{s,\sigma}) \Psi_{i,-\sigma} \\
 & + (\Psi_{p,\sigma} \Psi_{p,-\sigma} \Psi_{s,-\sigma}^*),
 \end{aligned}$$

$$(5.3.1)$$

where α_1 and α_2 are polaritons with parallel and antiparallel spins, respectively, f is a continuous wave, linearly polarized, coherent pump with angular frequency ω , the excitonic Hopfield coefficients are denoted as $X_{m,\sigma}$ and $E_{n,\sigma}$ are bare energies, given by [147]:

$$E_{n,\sigma} = \frac{E_{C,n} + E_{X,\sigma}}{2} - \frac{1}{2}\sqrt{(E_{C,n} - E_{X,\sigma})^2 + 4V^2} \quad (5.3.2)$$

with photon $E_{C,n}$ and exciton $E_{X,\sigma}$ energies defined by:

$$\begin{aligned} E_{C,n} &= \frac{\hbar^2 k_n^2}{2m_C} - \frac{i\Gamma_C}{2} \\ E_{X,\sigma} &= -\sigma g \mu_B B - \frac{i\Gamma_X}{2} \end{aligned} \quad (5.3.3)$$

where $n = s, p, i$, Γ_C and Γ_X are the photon and exciton decay rates, B stands for magnetic flux density, g is the exciton g -factor and μ_B is the Bohr magneton.

Solution to the equations 5.3 can be found numerically, by assuming randomness of the amplitude and phase of all the six states and selecting the intensity of the states to be small. Figure 5.3.1a, presenting a relative phase of $\sigma+$ and $\sigma-$ polarized signal components in a function of time shows, that regardless of the initial value of the phase, after few hundred picoseconds both $\sigma+$ and $\sigma-$ phases lock to one phase difference. To consider locking of the phases, both polarized signal components should have the same energy, to have the Zeeman splitting suppressed. For the simulation from figure 5.3.1a, $\alpha_2 = -0.05\alpha_1$. In the system with no interactions between oppositely polarized spins, when $\alpha_2 = 0$, the phase locking is not observed, which is demonstrated in figure 5.3.1b. Lack of the phase locking is accompanied by remaining of the Zeeman splitting in the system. The last figure from 5.3.1c shows a typical dependence of the pump, signal and idler energies on the intensity of the pump for both polarizations, with $\alpha_2 = -0.05\alpha_1$. The parametric scattering threshold is indicated by the dashed vertical line. It is worth mentioning that the signal blueshift obtained in simulations is about 0.5 meV smaller than the blueshift

experimentally obtained. This may be explained by using simplified model for simulations, which neglect many mechanisms.

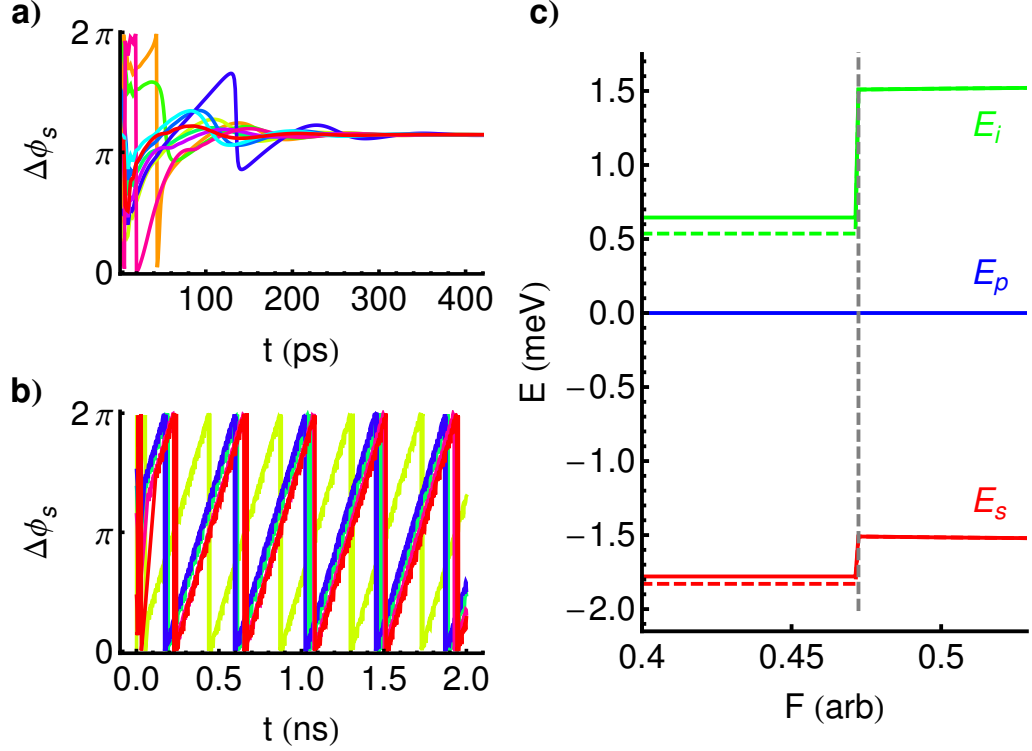


Figure 5.3.1: Time dependence of the relative phase of σ^+ and σ^- polarized signal components for different initial conditions and $\alpha_2 = -0.05_1$, (b) the same as in (a) for $\alpha_2 = 0$ to show that phase locking does not take place. (c) Dependence of the pump, idler and signal energies on the pump intensity ($F = |f^2|$) for σ^+ (dashed lines) and σ^- (solid lines) polarizations with $\alpha_2 = -0.05\alpha_1$. The vertical line indicates the parametric scattering threshold. The dispersion was taken with a Rabi splitting of 6 meV and a cavity photon effective mass $\sim 5 \times 10^{-5}$ of the free electron mass. The photon and exciton linewidths were taken as 0.1 and 0.5 meV, respectively. The pump was taken with an angle of incidence of $\Theta = 10^\circ$ and energy 1 meV above the bare lower polariton energy at the same angle. $B = 1T$.

The model does not take into account, inter alia, inhomogeneous broadening of the exciton, giving rise to higher losses in the idler and population of the incoherent reservoir or partial screening of the exciton resonance at higher pump densities, leading to reduction of the polariton Rabi splitting.

It is clear, therefore, that if there are no interactions between oppositely polarized spins (polaritons with antiparallel spin), the phase locking does not occur and we do not expect suppression of the Zeeman effect. In the case when interactions occur, phase locking takes place and is slightly sensitive to the initial conditions. For non-zero α_2 , the phase locking mechanism is slightly dependent on the pump power. The energy of coupling between coherent cross-polarized polariton modes is proportional to $\alpha_2 N_{coh}$, where α_2 is number of polaritons with antiparallel spin and N_{coh} is the total coherent polariton density in the OPO states, determined by the pump population. If $\alpha_2 N_{coh}$ is larger than the Zeeman splitting below the threshold, then we can observe quenching of the Zeeman splitting above the threshold, resulting from the efficient mode synchronization. From the figures 5.2.1 and 5.2.2 one can see that for larger excitation angle (15°) quenching of the Zeeman splitting occurs at lower magnetic field than in case of smaller excitation angle (10°). We explained this behaviour as a result of decreasing of the coupling strength between $\sigma+$ and $\sigma-$ polarized signal states, due to the depletion of the pump state, laying closer to the excitonic state than at smaller excitation angle, thus being absorbed by the excitonic reservoir [148, 149], which is followed by occurring of quenching of Zeeman splitting at smaller magnetic fields.

5.4 Conclusions

We studied experimentally photoluminescence spectra from a GaAs based microcavity in the OPO configuration. The measurements were taken in the presence of the magnetic field varying between 0T and 5T. Spectra of polaritons emission at $k \sim 0$ were first recorded in two circular polarizations σ^+ and σ^- for different magnetic fields at powers below and above the threshold of stimulated scattering and for two angles of incident beam: 10° and 15° . For both incident angles, we observed quenching of the Zeeman splitting at magnetic field $\sim 1T$. The second part of the experiment was to record the

energy splitting between two circular polarizations σ^+ and σ^- as a function of the pump power for various magnetic fields. The obtained results clearly show that the Zeeman splitting is strongly reduced at high density system, above the threshold for parametric oscillation. The experimental results were explained in terms of the phase synchronization of spin-up and spin-down polarized polariton condensates, resulting from a nonlinear coupling via the coherent pump state, and are in agreement with numerical calculations based on the mean-field coupled mode theory.

Chapter 6

Bloch oscillations of microcavity polaritons

6.1 Background

The first theoretical attempt of understanding the electronic transport in solids was performed by Paul Drude at the beginning of the XXth century. He studied behaviour of materials and developed the classical free- electron model. It describes particles moving ballistically, unless they encounter a scattering centre, when the free-electrons during collision abruptly change their velocity, forgetting about the previous direction of motion. Particles are thus governed by a fully random change of momentum with the mean free time between scattering τ . The most important result of the Drude model is the relation between the electric current density J and the electric field E , given by:

$$J = \left(\frac{ne^2\tau}{m}\right)E = \sigma E \quad (6.1.1)$$

where n is the density of electrons, e – charge of electron, m – its mass and σ is the conductivity. The Drude model describes the transport of carriers in

a solid within a good approximation if they remain close enough to the lower part of the band and the free-electron approach can be used. While the field is higher the carriers can reach the higher parts of the band and the scattering rate is lower. They do not longer behave as free-electrons, which is the natural consequence of the electronic band structure of the crystal at the presence of a static electric field, but they start to oscillate spatially. This phenomenon was first described by F. Bloch and therefore named Bloch oscillations.

The question of Bloch oscillations (BOs) has its origin in studies of the dynamics of electronic wavepackets in periodic potentials by Bloch in late 1920s [150] and by theoretical consideration of crystalline electrons in the presence of the static electric field, undertaken by C. Zener in early 1930s [151]. Zener reached a conclusion that electrons in such an environment change the sign of their real space velocity at the boundary of the first Brillouin zone. This happens due to the Bragg reflections and results in oscillatory motion, not uniform as was believed before. It took over half a century till the phenomenon has been experimentally confirmed in artificial crystals (GaAs/AlGaAs superlattices), due to the requirement of materials with coherence lifetime larger than the oscillation period, necessary in order to observe the Bloch oscillations [152, 153]. Since then, Bloch oscillations have been observed in many other systems including light pulses in photonic crystals [154, 155, 156], cold atoms [157] or atomic Bose-Einstein condensate [158] in optical lattices.

According to Bloch's theorem, dynamics of a Bloch electron in the presence of an external electric field F is given by:

$$\hbar\dot{k} = eF \tag{6.1.2}$$

Assuming that energy of the band is defined by:

$$E_k = -2\cos(kd) \tag{6.1.3}$$

we can easily find the position (x) of the particle as a function of time:

$$\begin{aligned} k &= \frac{eFt}{\hbar} \\ \Rightarrow v(t) &= \frac{2d}{\hbar} \sin(kd) = \frac{2d}{\hbar} \sin\left(\frac{Fdet}{\hbar}\right) \end{aligned} \quad (6.1.4)$$

$$\Rightarrow x(t) = -\frac{2}{eF} \cos\left(\frac{Fdet}{\hbar}\right)$$

where d is the lattice parameter and defines the first Brillouin zone to $2\pi/d$. Let's first consider the motion of the free-electron under the influence of the electric field in the scattering-free system. In this case the momentum, the velocity and the kinetic energy of the electron would increase indefinitely and nothing peculiar could be observed. The behaviour of the electron in the energy band is, however, dramatically different. In the absence of scattering, the particle simply starts at the bottom of the band and accelerated by the electric field travels along the k -vector until it reaches the edge of the first Brillouin zone $k = \pi/d$. In the absence of interband tunnelling, the particle is there reflected to $k = -\pi/d$, where it starts losing the energy and is traveling continuously towards $k = 0$, where the cycle begins again. The sign change of the k -vector at the first Brillouin zone boundary in reciprocal space results in a sign reversal of the velocity. This means that each time the particle reaches $k = \pi/d$, the direction of the propagation changes and thus we can also observe Bloch oscillations in real space. The periodic motion of the particle in both real and reciprocal space is characterized by a time period:

$$\tau_{BO} = \frac{\hbar}{eFd} \quad (6.1.5)$$

The frequency ν_{BO} is related to the time period as:

$$\nu_{BO} = \frac{1}{\tau_{BO}} = \frac{eFd}{\hbar} \quad (6.1.6)$$

This means that electronic wave packet in periodic potential is described by a periodic motion in k-space, characterized by a frequency ν_{BO} proportional to the applied electric field F . The electron, moving back and forth between the boundaries of the first Brillouin zone will be localized in a finite region with the length given by:

$$L = \frac{\Delta}{eF} \quad (6.1.7)$$

where Δ stands for the width of the band. The dynamics of the particle in a 1D periodic potential with the applied static force can be described by the Hamiltonian [159]:

$$H = H_0 + Fx = \frac{p^2}{2m} + V(x) + Fx \quad (6.1.8)$$

where $V(x+d) = V(x)$ describes the periodic potential. Following [159], using tight-binding model the Hamiltonian 6.1.8 can be rewritten as:

$$H(k) = -\frac{\Delta}{2}\cos(kd) + iF\frac{d}{dk} \quad (6.1.9)$$

where

$$E(k) = -\frac{\Delta}{2}\cos(kd) \quad (6.1.10)$$

is the dispersion relation for the field-free case and quasimomentum is given by:

$$k(t) = k_0 - \frac{Ft}{\hbar} \quad (6.1.11)$$

Hamiltonian 6.1.9 may be also rewritten as:

$$\hat{H} = -\frac{\Delta}{2} \cos(\hat{k}d) + F\hat{x} \quad (6.1.12)$$

where \hat{k} and $\hat{x} = id/dk$ are operators satisfying the commutation rule $[\hat{x}, \hat{k}] = i$. The electron group velocity, gained from the applied electric field is given by:

$$v = \frac{1}{\hbar} \frac{\partial E}{\partial k} \quad (6.1.13)$$

Using relation dispersion 6.1.10, we get:

$$v = \frac{d\Delta}{2\hbar} \sin(kd) \quad (6.1.14)$$

We can now replace the operators \hat{x} and \hat{k} with real numbers x and $k = p/\hbar$ and the Hamiltonian 6.1.12 transforms into:

$$H = -\frac{\Delta}{2} \cos(p\delta) + Fx \quad (6.1.15)$$

where $\delta = d/\hbar$. It is now easy to write Hamilton's equations of motion:

$$\dot{x}(t) = \frac{\partial H}{\partial p} = \frac{\Delta\delta}{2} \sin(p\delta) \quad (6.1.16)$$

$$\dot{p}(t) = -\frac{\delta H}{\delta x} = -F$$

and this gives the solution in the form:

$$x(t) = x_0 - \frac{\Delta}{F} \sin \frac{\omega_{BO} t}{2} \sin(\frac{\omega_{BO} t}{2} - p_0 \delta) \quad (6.1.17)$$

$$p(t) = p_0 - Ft$$

where p_0 and x_0 are initial conditions at $t = 0$ and $\omega_{BO} = F\delta$ is the Bloch

frequency. We can also define the mean momentum and the momentum width:

$$\langle p \rangle_t = p_0 - Ft \tag{6.1.18}$$

$$\Delta p_t^2 = \Delta p_0^2$$

As well as the time evolution of the mean position and mean width:

$$\langle x \rangle_t = x_0 - \frac{\Delta}{F} e^{-\Delta p_0^2 \delta^2 / 2} \sin \frac{\omega_{BO} t}{2} \sin \left(\frac{\omega_{BO} t}{2} - p_0 \delta \right) \tag{6.1.19}$$

$$(\Delta x_t)^2 = (\Delta x_0)^2 + \frac{\Delta^2}{2F^2} (1 - e^{-\Delta p_0^2 \delta^2}) \sin^2 \frac{\omega_{BO} t}{2}$$

Equations 6.1.19 show that $\langle x \rangle_t$ and Δx_t are periodic functions of time with the time period defined by the Bloch period ω_{BO} and the amplitude of the oscillation around the mean value depends on the value of the momentum width. Depending on the value of the momentum width, we can distinguish two regimes:

- for narrow Δp_0^2 , when $e^{-\Delta p_0^2 \delta^2} \approx 1$ the response of the system can be labelled as classical Bloch oscillation, with a constant width and an oscillating mean value
- for broad Δp_0^2 , when $e^{-\Delta p_0^2 \delta^2} \approx 0$, the mean value $\langle x \rangle_t$ is almost constant and Δx_t is oscillating. This behaviour is called breathing

The different trajectories in these two cases are shown in figure 6.1.1.

Bloch oscillations are possible only if the mean scattering time τ is larger than the period of Bloch oscillation. Hence, the condition:

$$\frac{edF\tau}{\hbar} > 1 \tag{6.1.20}$$

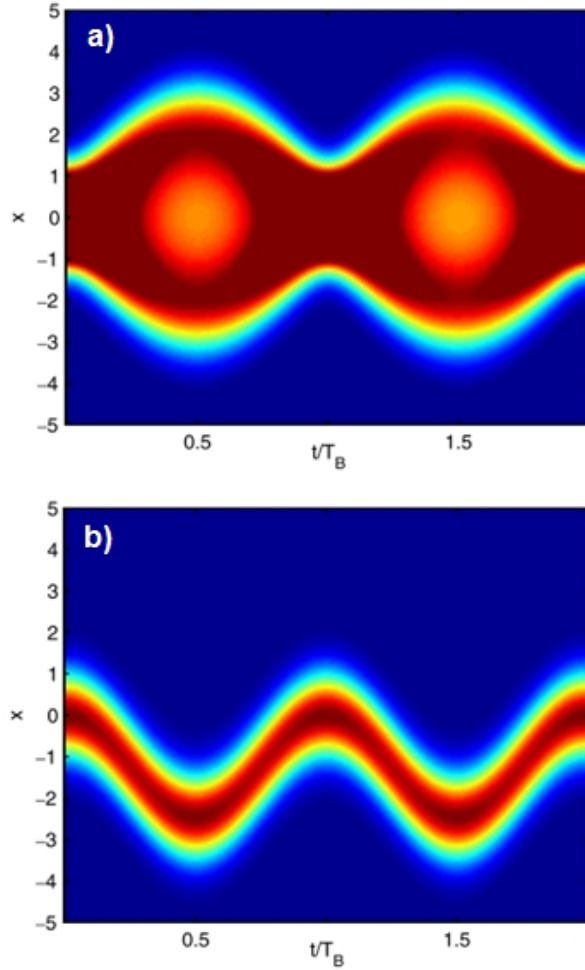


Figure 6.1.1: Particle mean position as a function of time, simulated for different widths of the particle wavefunction momentum distribution of Δp_0 : a) - breathing mode for wide $\Delta p_0 = 5$, b) - oscillatory mode for narrow $\Delta p_0 = 0.02$ (Source: [159]).

must be fulfilled. This condition is very difficult to be met in case of bulk semiconductors, unless a very high electric field is applied. This problem was resolved by fabricating semiconductor superlattices, formed by alternating materials with different bandgap energies. In superlattice structures the lattice period is much larger than in bulk semiconductors and the mean scattering times are longer, due to the electrons confinement, making Bloch oscillations observation possible.

6.1.1 Wannier-Stark ladder

Consider a superlattice of period d , composed of semiconductor coupled quantum wells. Applying an electric field to this superlattice structure induces a tilt of the quantum wells, so the adjacent quantum wells are no longer at the same level. For sufficiently high field translational invariance of the periodic potential is destroyed and electron states become localized, each of them having maximum in a well. These states are called Wannier-Stark states. The energies of the Wannier-Stark states can be easily calculated by finding the eigenstates of the Hamiltonian 6.1.9 through integrating the first-order differential equation [159]:

$$-\frac{\Delta}{2}\cos(kd)\Psi(k) + iF\frac{d\Psi(k)}{dk} = E\Psi(k) \quad (6.1.21)$$

with periodic boundary condition $\Psi(k+d) = \Psi(k)$. Resulting energies of the Wannier-Stark states are then given by:

$$E_n = ndF, n = 0, \pm 1, \pm 2, \dots, \quad (6.1.22)$$

forming the, so called, Wannier-Stark ladder and the corresponding eigenstates are given by:

$$\Psi_n(k) = \langle k | \Psi_n \rangle = \sqrt{\frac{d}{2\pi}} e^{-i[nkd + \gamma \sin(kd)]} \quad (6.1.23)$$

with

$$\gamma = \Delta/2dF \quad (6.1.24)$$

Any superposition of these states is characterized by an oscillatory behaviour

with the Bloch oscillation time period and the energy separation between adjacent states can be given in terms of the Bloch oscillation frequency:

$$\Delta = \hbar\omega_{BO} \tag{6.1.25}$$

Therefore, in the presence of an electric field, the energy spectrum of the electrons is no longer a continuum. Instead, it splits into series of levels with the equidistant energy spacing, which is proportional to magnitude of the applied electric field. The first description of this phenomenon was given by Wannier in 1960 [160], however, for many years both Wannier-Stark ladder and Bloch oscillations remained very controversial topics, mainly since they were seen as inconsistent with other theories like Franz-Keldysh effect or Zener tunnelling, and many claimed that it was not possible to observe such an effect [161, 162, 163, 164, 165, 166]. It was not clear whether any of these phenomena can be observed – a number of attempts have been made in order to find experimental evidence of the Wannier-Stark ladder and for a long time all of them were unsuccessful. For the first experimental evidence of Wannier-Stark ladder, again possible thanks to the development of semiconductor growth techniques, we had to wait till 1988, when the first observations of this phenomena were made in semiconductor superlattices [167], [168].

6.1.2 Landau-Zener tunnelling

The adiabatic approximation of the particle motion, assuming that the particle always stays in the same band, which was considered in this thesis till this moment, does not have to be the only possible scenario. Increasing the acceleration of the particle over the critical value results in the occurrence of the Landau-Zener tunnelling. The particle approaching the edge of the first Brillouin zone at $k = \pi/d$ has a finite probability of tunnelling to the state of

$k = -\pi/d$ in the adjacent band and this probability is given by [169]:

$$P = e^{-\left(\frac{\pi^2}{\hbar^2} \frac{m d E_{gap}^2}{|eF|}\right)} \quad (6.1.26)$$

It was shown in 1977 that the spectrum of Bloch electrons under the influence of electric field is in fact continuous [170], which is essential for the occurrence of the Landau-Zener tunnelling. This discovery implies that the Wannier-Stark ladders are resonances – they are only metastable states with long lifetimes, limited by the probability of tunnelling.

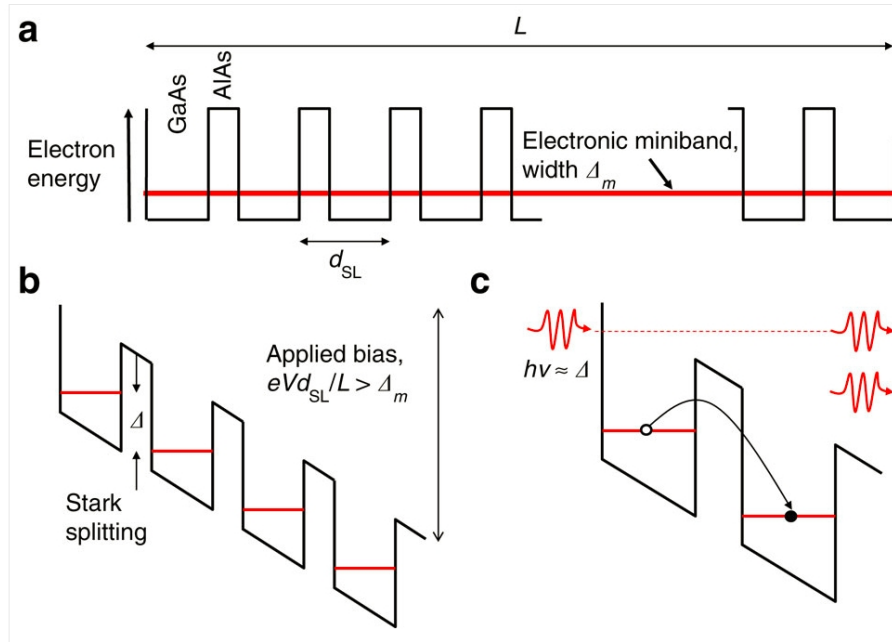


Figure 6.1.2: Electronic energy band structure of the superlattice: a) in the absence of applied electrical field, b) under an applied electric field - formation of Wannier-Stark ladder and c) Landau-Zener tunnelling scheme (Source: [171])

6.1.3 Bloch oscillations in different systems

As already mentioned, the prerequisite for observing the Bloch oscillations is that the coherent propagation time has to be larger than the oscillation period.

It took 60 years till this obstacle could be overcome and Bloch oscillations could be finally observed experimentally for the first time. Since the first observation in superlattice system, they were detected in various systems, all of them characterized by a large spatial and temporal coherence. On top of the requirement of the long coherence time, also the constant force driving the Bloch dynamics is needed. Depending on the system, different ways of accelerating particles were proposed. In case of ultracold atoms the external force can be introduced by using a tunable frequency difference between two counter propagating laser waves creating the optical potential [157] or by use of the gravity [172], [173]. The propagation constants in the systems where photonic Bloch oscillations are expected can be controlled by applying the bias [174], [175], temperature gradient [154], linear increase in the widths and spacing between the waveguides in the array [155], linear gradient in the optical thickness [176] or by bending the waveguides, which results in a linear variation in the refractive index [177].

Recently, the possibility of Bloch oscillations of polaritons has been proposed in a patterned one-dimensional microwires [178]. Since polaritons have long coherence length and their evolution in time can be easily measured, they are good candidates for studying Bloch oscillations. On the other hand, the common presence of structural disorder in the microcavity samples fabricated for studying polaritons, resulting in localization of polaritons, was considered as an obstacle that could hinder or even prevent from observing the phenomenon. Another mechanism, contributing to the damping of Bloch oscillations, is formation of the parametric instabilities of polariton lattices with one-dimensional periodic potentials [179]. However, what is very interesting, is that these two mechanisms, being obstacles on their own, can compensate each other, suppressing the damping of the Bloch oscillations [178].

Flayac et al. showed theoretically that it should be possible to observe Bloch oscillation of polaritons in a $L_x = 100\mu m$ long GaAs microcavity etched in the y-direction (width), causing the energy confinement approximately given by

$E_c = \hbar^2 \pi^2 / 2m^* L_y^2$ where m^* is the effective mass of the polariton.

The potential ramp, acting on the photonic part of the polaritons, could be introduced by changing the lateral size of the wire along the x-axis, so its dependence in the region where Bloch oscillations are expected is given by $L_y(x) \sim L_0/\sqrt{x}$. They indicate different possibilities of producing the periodic potential, needed to open the gap in the polariton dispersion: covering the wire with metallic pattern [88, 89, 180], excitation of a surface acoustic wave [87] or squarewave-like lateral etching [91]. In the work [178] only the first method was investigated, however, it is worth mentioning that from experimental point of view, in reality choosing metal deposition onto the wire is not the most appropriate approach. Metal extensively reduces the lifetime of photons, and thus the lifetime of polaritons is also reduced, which is not desirable. In our experiment we used squarewave-like lateral etching instead, which will be discussed in the next section.

Following [178], the evolution of the polariton system in the periodic potential can be described using one-dimensional time dependent Schrodinger and Gross-Pitaevskii equations:

$$i\hbar \frac{\partial \psi_{ph}}{\partial t} = -\frac{\hbar^2}{2m_{ph}} \frac{\partial^2 \psi_{ph}}{\partial x^2} + U_{ph} \psi_{ph} + \frac{\Omega_R}{2} \psi_{ex} - \frac{i\hbar}{2\tau_{ph}} \Psi_{ph} + P(t) \quad (6.1.27)$$

$$i\hbar \frac{\partial \psi_{ex}}{\partial t} = -\frac{\hbar^2}{2m_{ex}} \frac{\partial^2 \psi_{ex}}{\partial x^2} + U_{ex} \psi_{ex} + \frac{\Omega_R}{2} \psi_{ph} + \alpha |\psi_{ex}|^2 \psi_{ex} - \frac{i\hbar}{2\tau_{ex}} \psi_{ex}$$

Where ψ_{ph} and ψ_{ex} are photonic and excitonic fields, respectively, $m_{ph} = 5 \times 10^{-5} m_{el}$, $m_{ex} = 0.4 m_{el}$ and m_{el} are masses of photon, exciton and free electron, $\Omega_R = 14 meV$ is Rabi splitting, $\tau_{ph} = 40 ps$, $\tau_{ex} = 150 ps$ are lifetimes of photons and excitons and $P(t)$ is a quasi-resonant Gaussian photonic

pump. Polariton-polariton repulsive interactions are hidden in $\alpha = 6E_b a_B^2/S$ with E_b - exciton binding energy, a_B -Bohr radius and S-normalization area. $U_{ph}(x) = -Fx$ and $U_{ex}(x)$ are the accelerating ramp potential, introducing a force $F = 0.2meV/\mu m$ and the squarewave-like potential with period $d = 1.56\mu m$ and amplitude $A = 2meV$.

For the given values, used in simulations, one obtains modification of the polaritons dispersion shown in figure 6.1.3a, with the Energy gap $E_g = 0.75meV$ and the width of the first band $\Delta_1 = 1meV$. The sample was excited with a $2ps$ long pulse focused into a spot with a size of $20\mu m$ and tuned close to the energy of the lower polariton branch at $k = 0$. Under such conditions, the system revealed clear Bloch oscillations both in the real and k-space, with the amplitude $A_{BO} \approx 12\mu m$ and period $T_{BO} \approx 25ps$. The results of these simulations are presented in figure 6.1.3b-c and prove, that from a theoretical point of view observation of Bloch oscillations in polariton system is possible, which was one of the motivations for attempting an experimental realization of this effect.

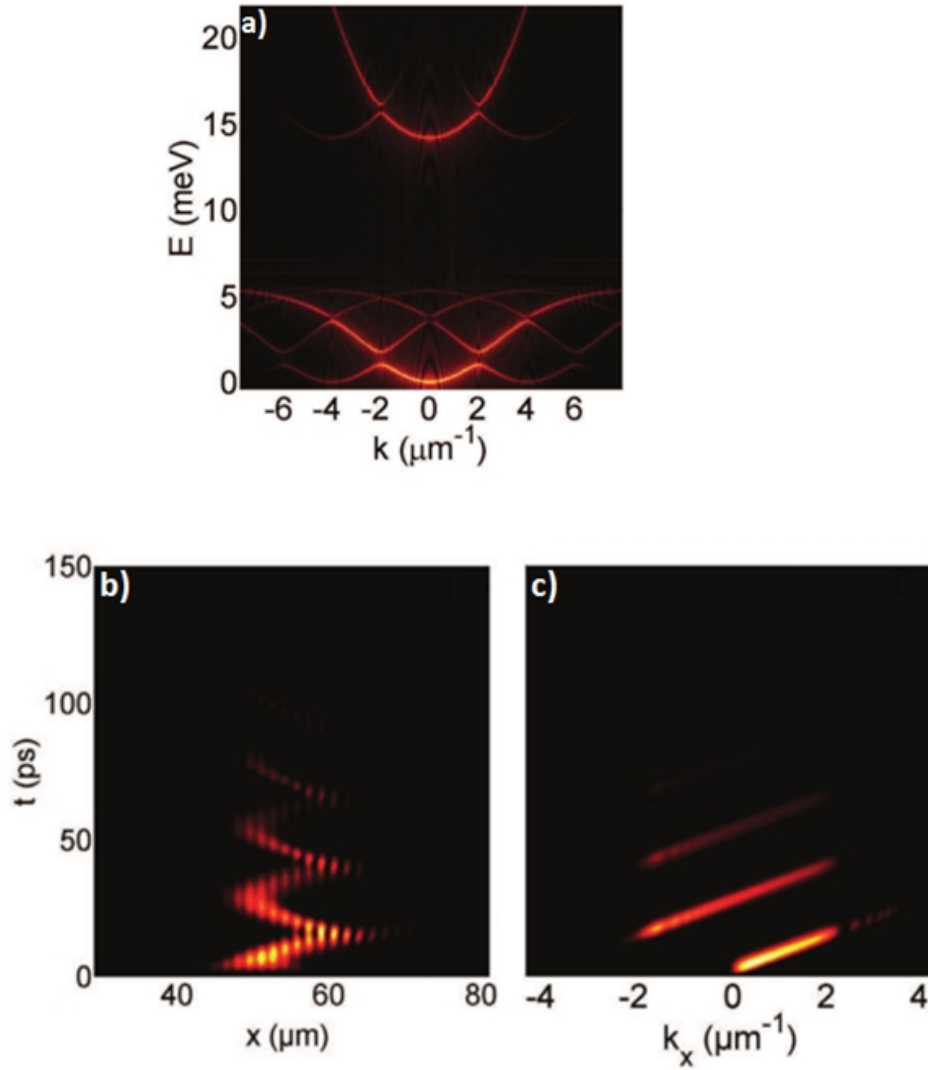


Figure 6.1.3: Bloch oscillations of polaritons in the biased square-wave potential obtained in theoretical studies of Flayac et al. [178]. a) modified polariton dispersion, resulting from the presence of the periodic potential $U_{ex}(x)$, the time dependence of the density probability in real (b) and k -space (c), revealing the presence of the Bloch oscillations and showing the fraction of particles escaping the first Brillouin zone at its edge at each period of oscillations, associated with the Landau-Zener tunnelling

6.2 Structures

Thinking of observing Bloch oscillations of polaritons, first of all we should concentrate on fabricating a sample with a high Q-factor, where the lifetime of polaritons is relatively long. Secondly, we need to introduce the periodic potential, that will open a gap in the polariton dispersion, and finally, an accelerating potential is required, acting on the polaritons with the constant force F .

The sample used in this experiment was designed and grown in Laboratoire de Photonique et de Nanostructures (LPN/CNRS). It is a GaAs/AlGaAs semiconductor microcavity, consisting of 40 pairs of $Ga_5Al_{95}As/Ga_{80}Al_{20}As$ bottom DBRs and 28 pairs of $Ga_5Al_{95}As/Ga_{80}Al_{20}As$ top DBRs separated by a $\lambda/2$ cavity with 3 sets of four 7nm GaAs QWs, resulting in a Rabi splitting of $\Omega_R = 15meV$.

The $120\mu m$ wire-shaped structures were obtained by using electron-beam lithography and reactive ion etching. The shape of the long wires was modified, so the lateral dimension of the structure changes from $\sim 1.5\mu m$ to $\sim 4\mu m$. The width of the middle $40\mu m$ of the wire, where the oscillations are expected to take place, was additionally periodically modulated in the way, that the amplitude V of this periodic modulation is constant, which together with the lateral wire profile provides a constant acceleration of polaritons.

Schematic lateral and periodic modulations with resulting energy profile as well as the scanning electron microscope (SEM) image of one of the studied samples is presented in figure 6.2.1. The fabricated wires were etched to have different periods P and varying potential V , which allowed us to search for Bloch oscillations with different temporal and spatial periods and study how these parameters influence the effect.

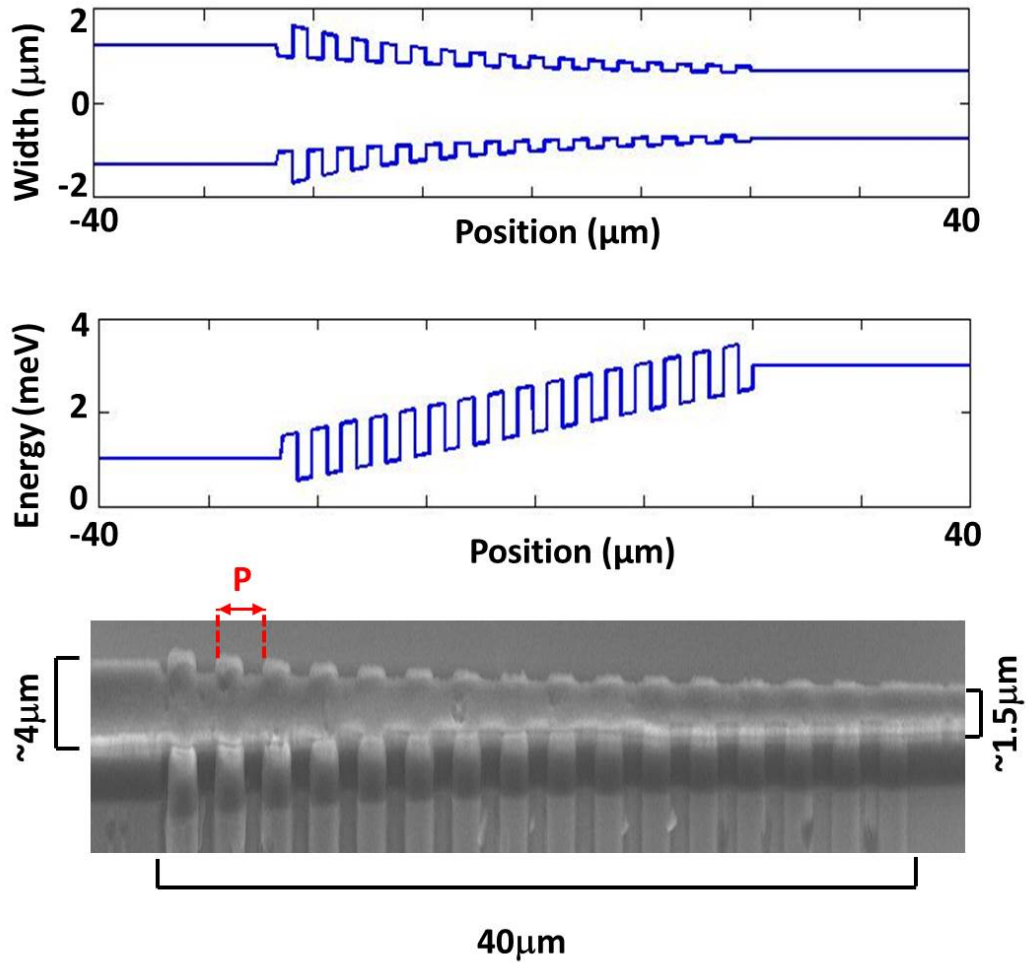


Figure 6.2.1: Microwire polariton structures for the Bloch oscillations studies. a) Scheme of the studied wire - top view, b) corresponding polariton potential profile, c) SEM image of one of the studied structure with characteristic lengths and period P

6.2.1 Wannier-Stark ladder

Before starting the experiment aiming at observing Bloch oscillations, we studied the emission from the structures under non-resonant cw excitation in real and k-space. The aim of these measurements was to observe the gap in the polariton dispersion and to measure the value of the acceleration F , which can be calculated from the tilt of the bands.

Figure 6.2.2a shows the expected gap in the polariton dispersion and the first Brillouin zone (FBZ) for one of the structures with $P = 2.1\mu m$. Figure 6.2.2b shows emission intensity from the structure in energy-position space, where the first band and the energy gap can be clearly seen. The tilt of the band, forming due to the gradient, gives us the acceleration $F = 63\mu eV/\mu m$. In the figure 6.2.2c polariton emission intensity integrated over the whole wire area is presented, for the range of energies corresponding to the first band. Peaks visible in this figure are equidistant. We measured the energy distance between them to be $168\mu eV$, which is almost exact expected value for this structure, calculated as $F * P = 63\mu eV/\mu m * 2.7\mu m = 170.1\mu eV$. Therefore, we attribute this behaviour to the Wannier-Stark ladder appearance. This, to our knowledge, is the first observation of the Wannier-Stark ladder in a photoluminescence experiment.

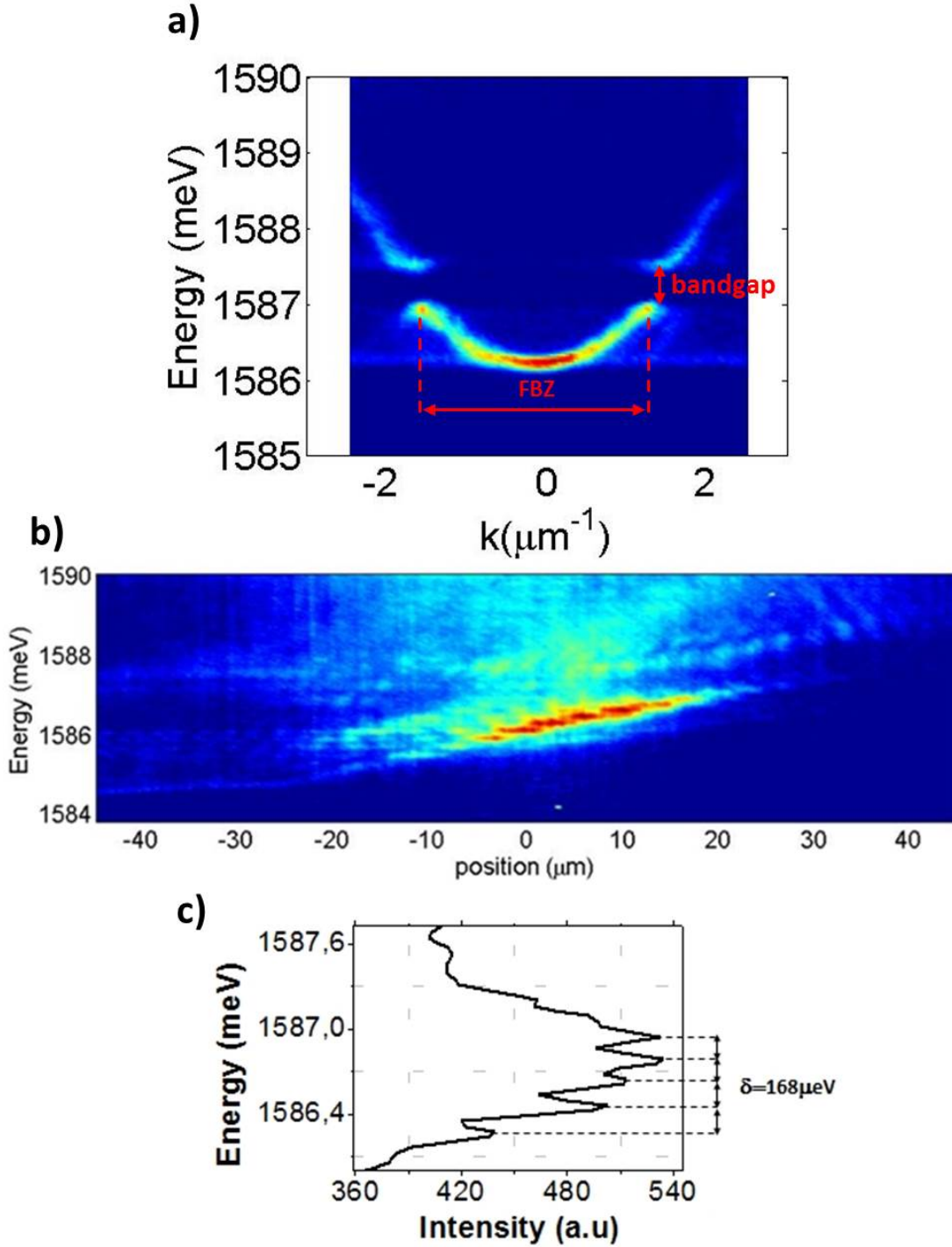


Figure 6.2.2: Emissions from the Bloch oscillator structures, excited non-resonantly. a) Polaron intensity in energy-momentum space with expected gap and the first Brillouin Zone $FBZ = 2.99 \mu\text{m}^{-1}$ for the structure with $P = 2.1 \mu\text{m}$, b) energy-real space emission from the structure with $P = 2.7 \mu\text{m}$, showing the band gap, the 1st band and the tilt in concert with the gradient, c) corresponding integrated emission spectrum for energies associated with the 1st band with characteristic, equidistant ($\delta = 188 \mu\text{eV}$) peaks, attributed to the Wannier-Stark ladder.

6.3 Observation of the polariton Bloch oscillations

The method of introducing accelerating potential relying on changing of the lateral size of the wire, proposed in [178], has some limitations preventing from observing the Bloch oscillations.

During the first experiments it turned out that exciting the laterally narrowed periodic wires resonantly does not allow exciting a state with narrow momentum width, thus it is hard to excite a well-defined state and then observe its time evolution. Therefore, we came up with the proposition of non-resonant excitation of periodic wires (without the lateral narrowing). Under non-resonant excitation, energy gradient can be obtained from the local energy blueshift generated by the excitonic reservoir.

The polariton condensate, formed by exciting the sample with the Gaussian pump spot, undergoes a local blueshift, caused by the repulsive interactions with the uncondensed excitons in the reservoir. Since the blueshift is spatially limited by the size of the pump, the consequence of its appearance is that the polaritons are forced to propagate outside of the excitation area - the condensate of polaritons gets accelerated and can propagate ballistically far away from the centre of the pump spot [181]. When the polaritons exit the excitation spot, their velocity remains constant and can be easily measured from the slope of their trajectory through the real space time-resolved measurements [182] (figure 6.3.1).

All the photoluminescence measurements were performed at $\sim 10K$, using a single-mode Ti:sapphire laser for cw measurements and Ti:sapphire laser with 1.4ps pulses at 80MHz repetition rate for the pulsed measurements.

Figures 6.3.2 show the time evolution of the polariton wavepacket versus position on the wire (a) and k-vector (b). These results were obtained by observing

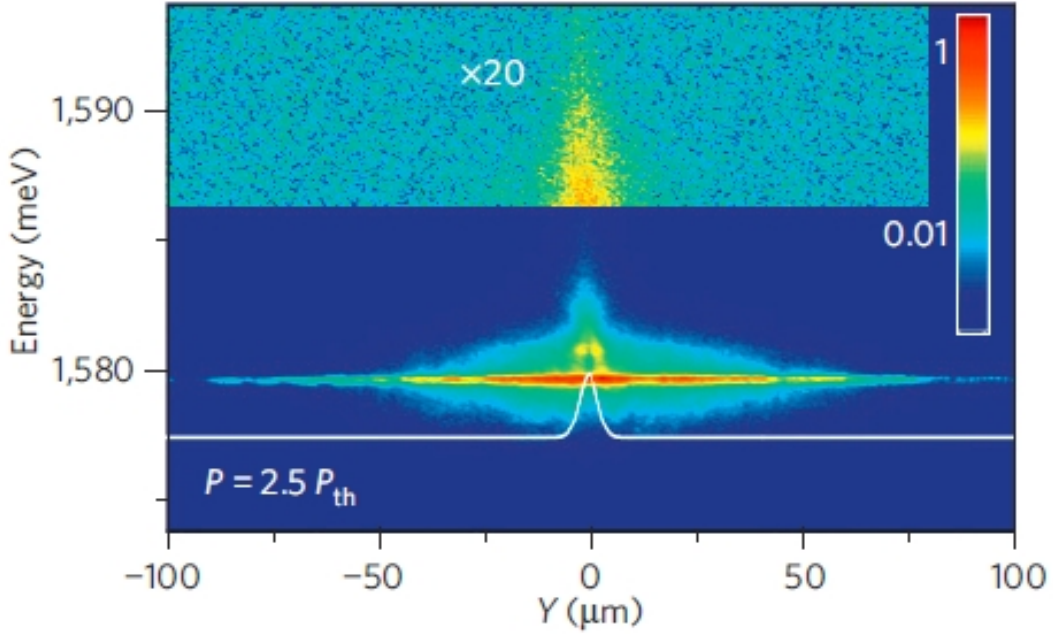


Figure 6.3.1: Real space propagation of non-resonantly excited polaritons along the wire with visible blueshift resulting from the repulsive interactions with the reservoir (Source: [99]).

polaritons propagating in the periodic wire with $P = 2.7\mu m$ from the condensate excited with a large excitation spot ($20\mu m$). Bloch oscillations arise in a region where a strong gradient of optical potential is present.

In k-space these oscillations are limited by the span of the 1st Brillouin zone, which for the given period is equal to $\frac{2\pi}{P} = 2.33\mu m^{-1}$, in accordance with the measured k-space width value. In the figure 6.3.2b the area corresponding to the 1st Brillouin zone is marked with black dashed lines. It can be clearly seen that at the boundaries of the permitted range of k-vectors, the signal is reflected from $+k$ to $-k$. The temporal period of the oscillations in reciprocal space is exactly the same as the temporal period in real space and both the spatial and temporal periods of the oscillations increase over time due to the decrease of the accelerating potential gradient. In real space the oscillations correspond to the change of the sign of the speed at the boundaries of the 1st Brillouin zone.

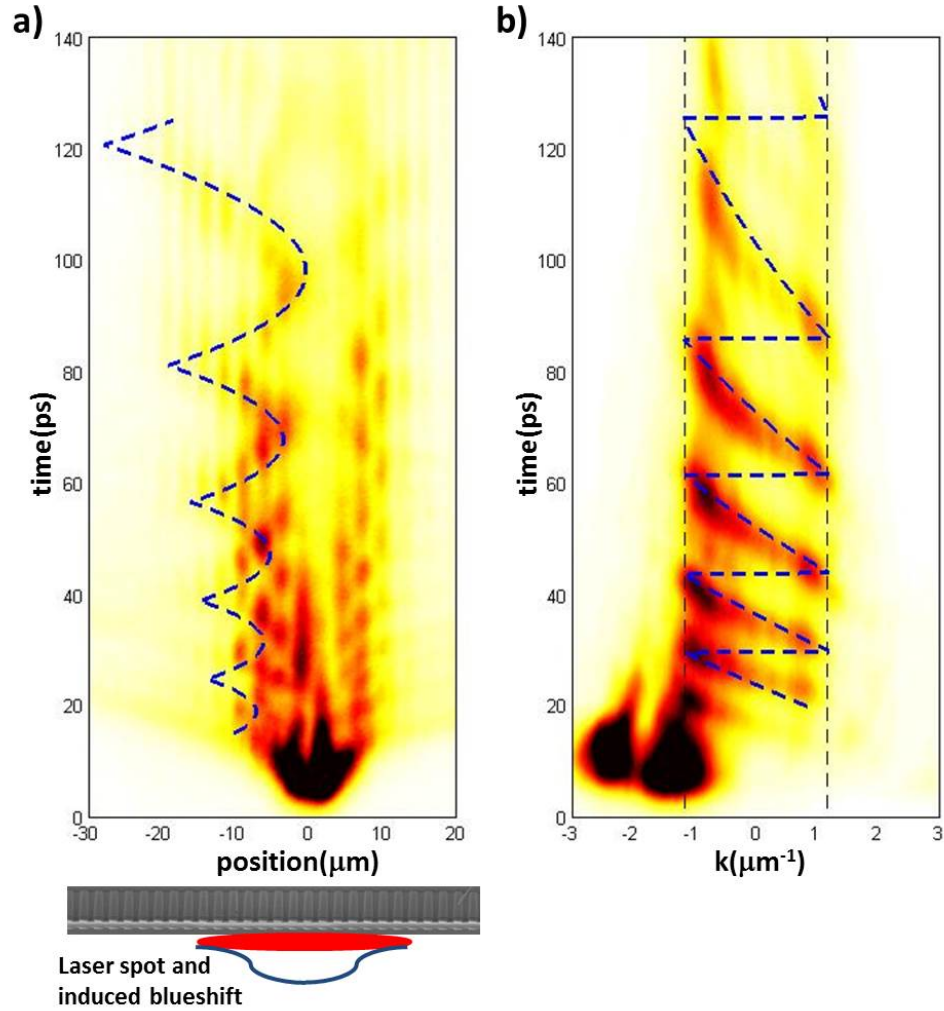


Figure 6.3.2: Emissions from the periodic wire, revealing the Bloch oscillations. a) polariton emission intensity versus time and position, b) polariton emission intensity versus time and k -vector, corresponding to the region on the left side of figure a. Wire, characterized by $P = 2.7\mu\text{m}$, $V = 1\text{meV}$ $m_p = 6.1 * 10^{-5}$, was excited non-resonantly with $P \approx 5P_{th}$ with a large laser spot. The blue dashed lines in both figures show the simulated trajectories of the wavepacket obtained with the fit parameters $\tau = 80\text{ps}$ and $F_0 = 0.25\text{meV}/\mu\text{m}$. The black dashed lines in b) indicate the boundaries of the first Brillouin zone.

Since the model described at the beginning of this chapter, given by Hartmann [159] and assuming that the force is constant in time is no longer valid,

we propose a simple model, showing that the evolution of the wavevector can be with good approximation given by a simple equation:

$$k(t) = k_0 + \frac{1}{\hbar} \int_{t_0}^t F(t') dt' = \frac{\tau F_0}{\hbar} (e^{-t/\tau} - e^{t_0/\tau}) \quad (6.3.1)$$

where the acceleration decays exponentially $F(t) = F_0 e^{-t/\tau}$ and τ is a decay constant.

The blue dashed lines indicate the trajectories that we modelled for a given wire parameters. The huge advantage of this model is that all but one variables needed for calculating the evolution both in k-space and real space can be obtained via direct measurements and only F_0 has to be fitted. The group velocity was extracted from the band shape, which allowed us to model the real space trajectory. In order to find the change of the energy gradient in time, we measured the time dependence of the energy for $k = 0$ emission, which gave us the result $\tau = 80ps$, corresponding to the decay rate of the acceleration. As we can see, the modelled trajectories are in very good agreement with the measurements.

In figure 6.3.3 we show the trajectories of the modulated wire with $P = 2.7\mu m$. The values of the time period T and width of the oscillation L in real space are shown for the 3 visible oscillations (a,b). These values are plotted in panel d and fitted with the linear function of slope 0.44 in panel d, giving the average velocity of the wavepacket $v_{avg} = 0.88\mu m/ps$. In panel c we can see the energies of the emissions measured at $k = 0$ and at two points close to the edges of the first Brillouin zone. In the figure 6.3.3 c, corresponding to the emission from $k = 0$ (the middle one) the decrease of the energy in time is also showed (red, dotted line) fitted with a decay constant $\tau = 80ps$. The black dashed lines indicate boundaries of the first Brillouin zone, and the red dashed lines show energy corresponding to the wire at low excitation power.

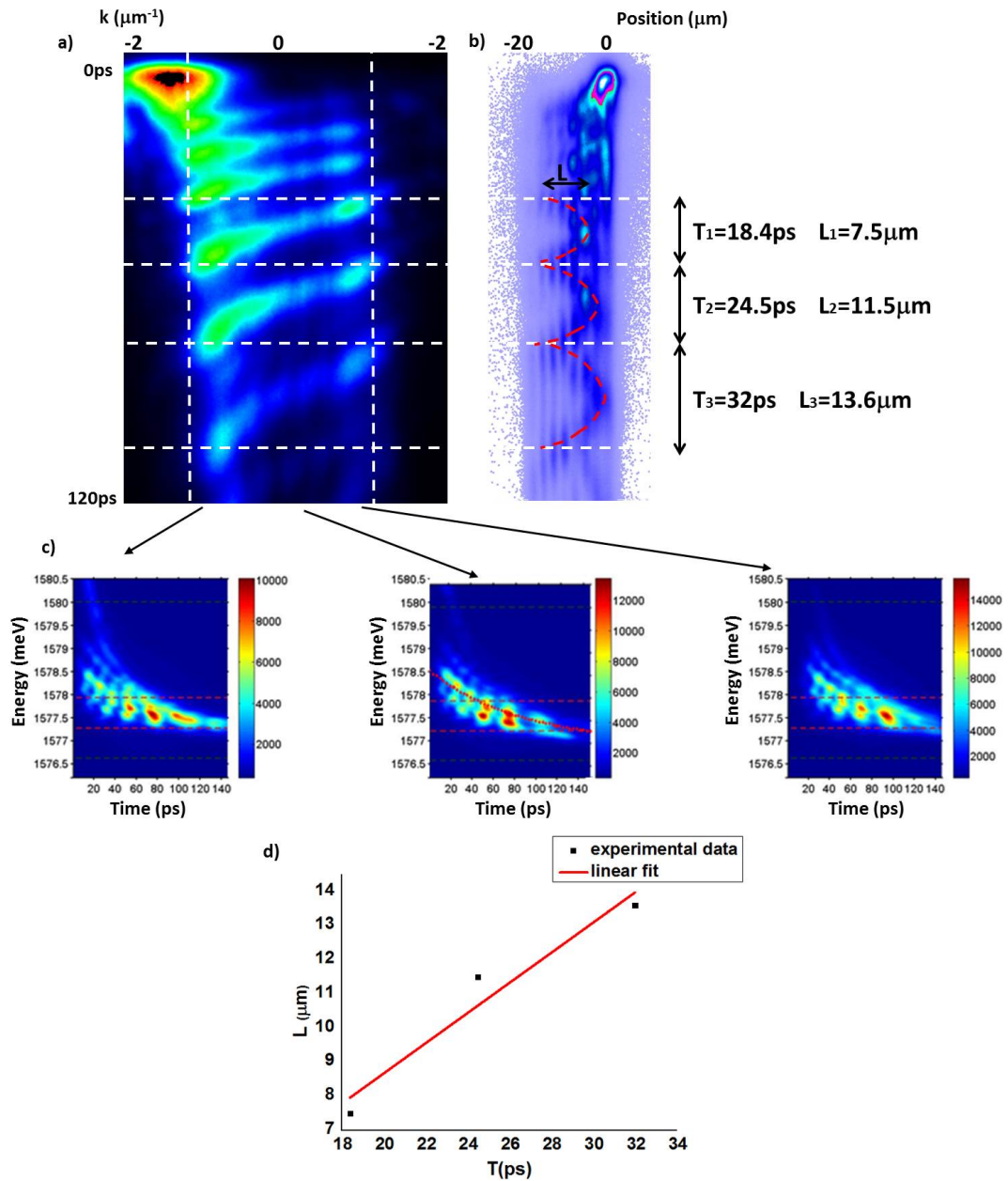


Figure 6.3.3: a) Real and b) k-space emissions from the same wire as 6.3.2 with the values of the time period T and width of the oscillation L in real space. c) Energies of the emissions at $k = 0$ and close to the edges of the first Brillouin zone. Dashed red and black lines correspond to the energies of the wire excited at lower power and to the boundaries of the first Brillouin zone, respectively. The red dotted lines show the energy decay fit with constant $\tau = 80\text{ps}$. d) Dependence of the width of the oscillations in real space vs. time period of a single oscillation.

6.3.1 Bloch oscillations in systems with varying potential period

We have attempted to observe Bloch oscillations in four modulated wires with varying potential period P : $2.7\mu m$, $2.1\mu m$, $1.9\mu m$ and $1.6\mu m$. In the figures 6.3.2 and 6.3.3 Bloch oscillations of $P = 2.7\mu m$ are presented. In the wire with $P = 2.1\mu m$ we were also able to observe this behaviour and the measured trajectories can be seen in figure 6.3.4. If we look at the panel b, where the time evolution of the wavepacket in reciprocal space is presented, we can clearly see, that the oscillations in this case are much wider than for the wire with $P = 2.7\mu m$. This is in accordance with the expectations, since the width of the first Brillouin zone $2k_B$ is determined by the potential period and depends as:

$$2k_B = \frac{2\pi}{P} \quad (6.3.2)$$

Calculated values of the width of the first Brillouin zone are $2.33\mu m^{-1}$ for $P = 2.7\mu m$ and $2.99\mu m^{-1}$ for $P = 2.1\mu m$, which is in a very good agreement with the measured widths of the oscillations in k -space. For the wires with $P = 1.9\mu m$ and $P = 1.6\mu m$ the probability of hopping to the second band was too high and thus the Bloch oscillations could not have been observed.

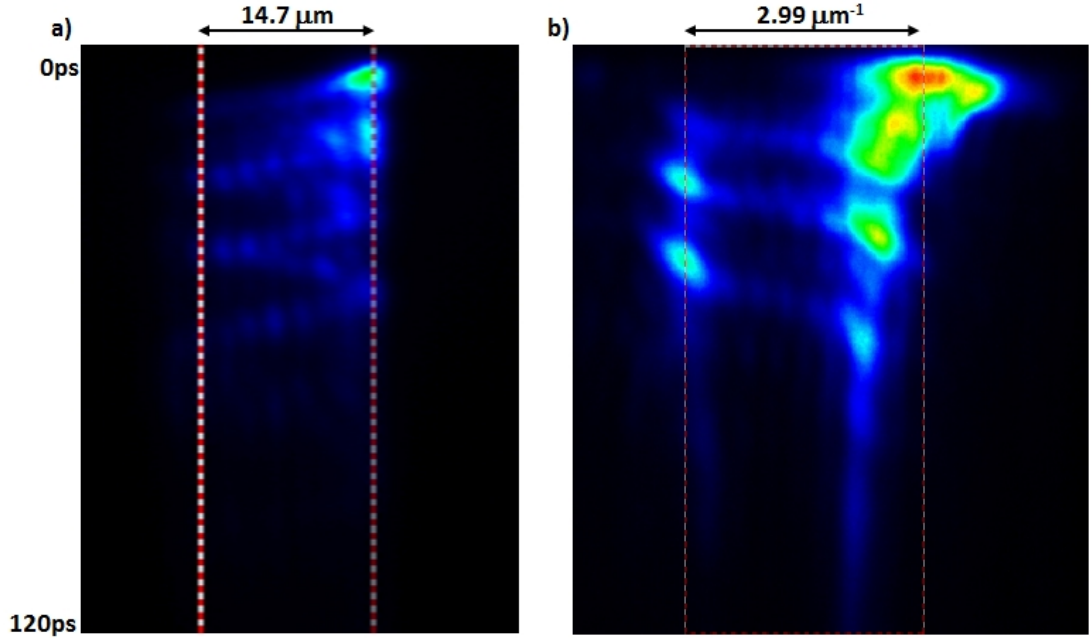


Figure 6.3.4: Emissions from the periodic wire with $P = 2.1\mu m$, revealing the Bloch oscillations. a) Real space emission, b) k-space emission, corresponding to the region on the left side of figure a.

6.3.2 Landau-Zener tunnelling

Recalling the formula 6.1.26 we know that the probability of the Landau-Zener tunnelling decreases with the decrease of the gradient F . Since we assume an exponential decrease of the acceleration, we expect to observe decreasing ratio of the polaritons escaping to the second band over time. Figure 6.3.5 shows the real and reciprocal space emissions of a modulated wire measured outside the area where the oscillations take place. We can clearly see that in every oscillation, some of the particles arriving at the edge of the first Brillouin zone, instead of being Bragg reflected, escape the band and propagate away. The intensity of the signal outside the oscillation region decreases over time until the acceleration of the particles is too low to allow the Landau-Zener tunnelling and all the remaining particles stay inside the region where the oscillations take place.

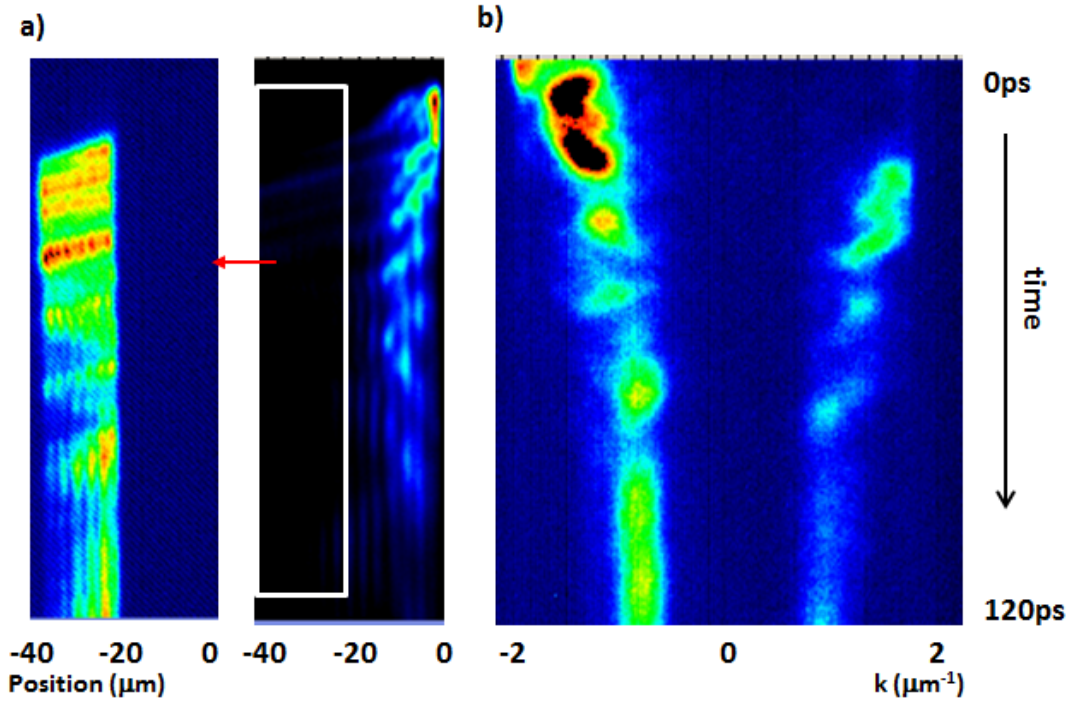


Figure 6.3.5: a) Real space emission from the periodic wire. The left site represents the enhanced signal outside the region of oscillations. b) k-space emission from the region outside the region of oscillations.

6.4 Conclusions

In this chapter we showed experimental results from the 1D polaritonic structures, expected to reveal the Bloch oscillations. We investigated two different kinds of modulated wires. First of them were laterally narrowed wires with etched periodic width modulations. These structures allowed us to observe behaviour associated with the presence of the Wannier-Stark ladder in the photoluminescence measurements, however observation of Bloch oscillations in such structures was not possible, since it was impossible to excite a well define state in this configuration. The second approach proposed in this chapter relied on using the wires which also have modulated periodic width, but in-

stead of introducing the energy gradient by lateral change of the width, we used the wires with constant width and the gradient was induced by the excitonic reservoir produced by non-resonant excitation with a large laser spot. This method allowed us to observe Bloch oscillations in wires characterized by different values of the modulated period P , both in real and k -space. The numerical calculations of the trajectories performed based on the model that we proposed are in agreement with experimental results. At the end of the chapter the phenomenon of the Landau-Zener tunnelling is briefly discussed and indicated in the figure presenting the Bloch oscillations, evidencing that part of the polaritons tunnels to the second band instead of Bragg reflecting at the boundary of the first Brillouin zone.

Summary

This thesis presents result from three different projects on microcavity polaritons, which I conducted during the time of my PhD.

Although at first sight the projects are not fluently connected with each other, they all aim at observing, understanding and explaining physics in this cutting-edge research field.

Significant part of this thesis is dedicated to the sample design – related issues. Chapter 4 discusses origin of the cross-hatch disorder arising from strain relaxation and explains how it affects the potential landscape. We propose how to suppress formation of the disorder in AlGaAs/AlAs microcavities with InGaAs quantum wells embedded in the cavity. By systematic studies of structures with varying Al content in DBRs and different number of quantum wells we demonstrate that cross-hatch disorder can be eliminated by reducing content of aluminium and by decreasing number of quantum wells. The proposed method of suppressing disorder in microcavity samples can have a significant impact on design of microcavity structures that will be used in all experiments and applications where long polariton propagation length is desirable.

In the next chapter the results of magnetophotoluminescence spectra measurements from a GaAs microcavity in the OPO configuration are presented. We experimentally demonstrate presence of the density-dependent renormalization of the Zeeman splitting and that above the threshold for parametric oscillation

the Zeeman splitting is quenched. Moreover we propose a model, based on the mean-field coupled mode equations, which explains the observed phenomena in terms of phase synchronization between spin-up and spin-down polariton condensates, originating in a nonlinear coupling via the coherent pump state.

Finally, results described in chapter 6 demonstrate that it is possible to observe Bloch oscillations in 1D polaritonic structures. By studying two kinds of modulated wires with energy gradient introduced either by changing the lateral size of the wire or from the local energy blueshift generated by excitonic reservoir, we showed many interesting phenomena taking place in such structures. First, we observed equidistant peak visible in the integrated emission spectrum for energies associated with the 1st band. We attribute this behaviour to the occurrence of Wannier-Stark ladder, which, to our knowledge, is the first observation of this phenomenon in a photoluminescence experiment. Next, we observed Bloch oscillations in wires with different values of the modulated period, both in real and k -space. Measured trajectories are in good agreement with obtained from numerical calculations. At the end we indicate that instead of Bragg reflecting at the boundary of the first Brillouin zone, part of the polaritons escape to the second band, which is the evidence of the Landau-Zener tunnelling.

Bibliography

- [1] Weisbuch, C. et al., *Observation of the coupled exciton-photon mode splitting in a semiconductor quantum microcavity*, Phys. Rev. Lett., Vol. 69, No. 23 (1992)
- [2] Kasprzak, J. et al., *Bose–Einstein condensation of exciton polaritons*, Nature 443, 409–414 (2006)
- [3] Amo, A. et al., *Superfluidity of polaritons in semiconductor microcavities*, Nature Phys., 5, 805 (2009)
- [4] Lagoudakis, K.G., Wouters, M., Richard, M., Baas, A., Carusotto, I., Andre, R., Le Si Dang, Deveaud-Pledran, B., *Quantized vortices in an exciton-polariton condensate*, Nature Phys., 4, 706 (2008)
- [5] Amo, A, et al., *Polariton Superfluids Reveal Quantum Hydrodynamic Solitons*, Science, 332, 1167 (2011)
- [6] Savvidis, P.G., Baumberg, J.J., Stevenson, R.M., Skolnick, M.S., Whittaker, D.M. and Roberts, J.S., *Angle- resonant stimulated polariton amplifier*, Phys. Rev. Lett., 84, 1547 (2000)
- [7] Stevenson, R.M., Astratov, V.N., Skolnick, M.S., Whittaker, D.M., Emam-Ismael, M, Tartakovskii, A.I., Savvidis, P.G., Baumberg, J.J., Roberts, J.S., *Continuous wave observation of massive polariton redistribution by stimulated scattering in semiconductor microcavities*, Phys. Rev. Lett., 85, 3680 (2000)

- [8] Baumberg, J.J., et al., *Spontaneous polarization buildup in a room-temperature polariton laser*, Phys. Rev. Lett., 101, 136409 (2008)
- [9] Tinkler, L., Walker, P.M., Clarke, E., Krizhanovskii, D.N., Bastiman, F., Durska, M. and Skolnick M.S, *Design and characterization of high optical quality InGaAs/GaAs/AlGaAs-based polariton microcavities*, Appl. Phys. Lett. 106, 021109 (2015)
- [10] Walker, P., Liew, T.C.H, Sarkar, D., Durska, M., Love, A.P.D., Skolnick, M.S., Roberts, J.S., Shelykh, I.A., Kavokin, A.V. and Krizhanovskii, D.N., *Suppression of Zeeman Splitting of the Energy Levels of Exciton-Polariton Condensates in Semiconductor Microcavities in an External Magnetic Field*, Phys. Rev. Lett., 106, 257401 (2011)
- [11] A. Kronenberger, P. Pringsheim, Z. Phys. 40, 75 (1926)
- [12] I.V. Obreimov, W.J. de Haas, Proc. Acad. Sci. Amsterdam 31, 353 (1928)
- [13] J. Frenkel, Physical Review 37, 17 (1931).
- [14] Ya.I. Frenkel, Phys. Z. Soviet Union 9, 158 (1936)
- [15] Wannier, G., *The structure of electronic excitation levels in insulating crystals*, Phys. Rev., 52, 191, (1937)
- [16] Mott, N.F., *Conduction in polar crystals* Trans Farad. Soc., 34, p. 500 (1938)
- [17] Peter Yu, Manuel Cardona *Fundamentals of Semiconductors: Physics and Materials Properties*, Fourth Edition, Springer 2010
- [18] Shinada, M., Sugano, S., *Interband optical transitions in extremely anisotropic semiconductors*, J. Phys. Soc. Jpn., 21, 10, 1936 (1966)
- [19] Yokoyama, H. et al., *Controlling spontaneous emission and threshold-less laser oscillation with optical microcavities*, Optical and Quantum Electronics, Vol. 24, Issue 2 (1992)

- [20] Abram, I., Robert, I., Kuszelewicz, R., *Spontaneous emission control in semiconductor microcavities with metallic or Bragg mirrors*, IEEE Journal of, Vol. 34, No.1, pp.71-76 (1998)
- [21] Vahala, K. J., *Optical microcavities*, Nature, 324, 6950, pp. 839-846 (2003)
- [22] Kavokin, A.V., et al., *Quantum wells with zero valence-band offset: Drastic enhancement of forbidden excitonic transitions*, Phys. Rev. B, 54, 11078(R) (1996)
- [23] Moreau, E., et al., *Single-mode solid-state single photon source based on isolated quantum dots in pillar microcavities*, Appl. Phys. Lett., 79, 2865 (2001)
- [24] Gerard, J.M., et al., *Enhanced Spontaneous Emission by Quantum Boxes in a Monolithic Optical Microcavity*, Phys. Rev. Lett., 81, 1110 (1998)
- [25] Kiraz, A., et al., *Cavity-quantum electrodynamics with quantum dots*, J. Opt. B: Quantum Semiclass. Opt., 5, 129-137(2003)
- [26] Hennessy, K. et al., *Quantum nature of a strongly coupled single quantum dot-cavity system*, Nature, 445, 896-899 (2007)
- [27] Skolnick, M.S., Fisher, T.A., Whittaker, D.M., *Strong coupling phenomena in quantum microcavity structures*, Semicond. Sci. Technol., 13, 645-669 (1998)
- [28] Savona V, Andreani L C, Schwendimann P and Quattropani, *Quantum well excitons in semiconductor microcavities: Unified treatment of weak and strong coupling regimes*, Solid State Commun. 93 733 (1995)
- [29] Babic, D.I., Corzine, S.W., *Analytic expressions for the reflection delay, penetration depth and absorptance of quarter-wave dielectric mirrors*, IEEE Journal of Quantum Electronics, Vol. 28, No. 2 (1992)
- [30] Bruce, C.F., Ciddor, P.E., *Phase dispersion in multilayer films*, JOSA, Vol. 50, No. 3 (1960)

- [31] Deng, H., Weihs, G., Santori, C., Bloch, J., and Yamamoto, Y., *Condensation of semiconductor microcavity exciton polaritons*, Science (New York, N.Y.), 298(5591), (2002), 199-202. doi: 10.1126/science.1074464
- [32] Butov, L.V. et al., *Towards Bose-Einstein condensation of excitons in potential traps*, Nature, 417, 47 (2002)
- [33] Butte, R., et al., *Transition from strong to weak coupling and the onset of lasing in semiconductor microcavities*, Phys. Rev. B, 65, 205310 (2002)
- [34] Khalifa, A.A., et al., *Electroluminescence emission from polariton states in GaAs-based semiconductor microcavities*, Appl. Phys. Lett. 92, 061107 (2008)
- [35] Ballarini, D., et al., *Transition from the strong- to the weak-coupling regime in semiconductor microcavities: Polarization dependence*, Appl. Phys. Lett., 90, 201905 (2007)
- [36] Shhri, H. Al, Bouarissa, N., Khan, M.J., *Exciton and polariton properties in $Ga_xIn_{1-x}As$ ternary mixed crystals*, Journal of Luminescence, 131, 2153-2159 (2011)
- [37] Tempel J.-S., et al., *Temperature dependence of pulsed polariton lasing in a GaAs microcavity*, New Journal of Physics, 4, 083014 (2012)
- [38] Kavokin, A., Malpuech, G., Laussy, F.P., *Polariton laser and polariton superfluidity in microcavities*, Phys. Lett. A, 306, 187-199 (2002)
- [39] Hopfield, J.J., *Theory of the contribution of excitons to the complex dielectric constant of crystals*, Phys. Rev. 112(5), (1958)
- [40] Deng, H., Haug, H., Yamamoto, Y., *Exciton-polariton Bose-Einstein condensation*, Reviews of Modern Physics, vol. 82, 1489-1537, (2010)
- [41] Pitaevskii, L., Stringari, S., *Bose-Einstein Condensation*, Oxford University Press (2003)

- [42] Bogoliubov, N.N., *On the theory of superfluidity*, J. Phys. (USSR) 11, 23–32 (1947)
- [43] Yamamoto, Y., *Stanford University notes for Bose-Einstein Condensation and Matter-Wave Lasers course*, Chapter 4 *Bogoliubov theory of the weakly interacting Bose gas* (2010)
- [44] Einstein, A., *Quantentheorie des einatomigen idealen Gases*, Sitzungsberichte der Preussischen Akademie der Wissenschaften zu Berlin, pages 261–267 (1924)
- [45] Bose, S.N., *Plancks Gesetz und Lichtquantenhypothese*, Z. Phys., 26:178 (1924)
- [46] Anderson, M.H., Ensher, J.R., Matthews, M.R., Wieman, C.E., Cornell, E.A., *Observation of Bose-Einstein Condensation in a dilute atomic vapor*, Science, 269, 198 (1995)
- [47] Bradley, C.C., Sackett, C.A., Tollet, J.J., Hulet, R.G., *Evidence of Bose-Einstein condensation in an atomic gas with attractive interactions*, Phys. Rev. Lett., 75, 1687 (1995)
- [48] Davis, K.B. et al., *Bose-Einstein Condensation in a gas of sodium atoms*, Phys. Rev., Lett., 75, 3969 (1995)
- [49] Klaers, J., Schmitt, J., Vewinger, F., Weitz, M., *Bose-Einstein condensation of photons in an optical microcavity*, Nature, 468, 545-548 (2010)
- [50] Oosawa, A., Tanaka, H., *Field-induced three-dimensional magnetic ordering in the spin-gap system $TlCuCl_3$* , J. Phys.: Condens. Matter, 11, 265 (1999)
- [51] Nikuni, T., Oshikawa, M., Oosawa, A., Tanaka, H., *Bose-Einstein condensation of dilute magnons in $TlCuCl_3$* , Phys. Rev. Lett., 84, 5868 (2000)
- [52] Demokritov, S.O., et al., *Bose-Einstein condensation of quasi-equilibrium magnons at room temperature under pumping*, Nature, 443, 430 (2006)

- [53] Eisenstein, J.P., MacDonald, A.H., *Bose-Einstein condensation of excitons in bilayer electron systems*, Nature, 432, 691 (2004)
- [54] Snoke, D., *Spontaneous Bose coherence of excitons and polaritons*, Science, 298, 5597, pp.1368-1372 (2002)
- [55] Butov, L.V., Gossard, A.C., Chemla, D.S., *Macroscopically ordered state in an exciton system*, Nature, 418, 751-754 (2002)
- [56] measured in experiment [46], copied from [www.http://en.wikipedia.org/wiki/Bose-Einstein_condensate](http://en.wikipedia.org/wiki/Bose-Einstein_condensate), version from 11 04 2014
- [57] Imamoglu, A., Ram, R.J., Pau, S., Yamamoto, Y., *Nonequilibrium condensates and lasers without inversion: exciton-polariton laser*, Phys. Rev. A, 53, 4250 (1996)
- [58] Deng, H., et al., *Polariton lasing vs. photon lasing in a semiconductor microcavity*, Proc. Natl. Acad. Sci. U.S.A., 100, 15318 (2003)
- [59] Wertz, E., et al., *Spontaneous formation of a polariton condensate in a planar GaAs microcavity*, Appl. Phys. Lett., 95, 051108 (2009)
- [60] Love, A.P.D, et al., *Intrinsic Decoherence Mechanisms in the Microcavity Polariton Condensate*, Phys. Rev. Lett., 101, 067404 (2008)
- [61] Krizhanovskii, D., et al., *Coexisting nonequilibrium condensates with long-range spatial coherence in semiconductor microcavities*, Phys. Rev. B, 80, 045317 (2009)
- [62] Tassone, F., Piermarocchi, C., Savona, V., Quattropani, A. and Schwendimann, *Bottleneck effects in the relaxation and photoluminescence of microcavity polaritons*, Phys. Rev. B 56, 7554 (1997)
- [63] Tartakovskii, A.I., et al., *Relaxation bottleneck and its suppression in semiconductor microcavities*, Phys. Rev. B, 62, R2283 (2000)
- [64] Baumberg J.J., Savvidis P.G., Stevenson R.M., Tartakovskii A.I., Skolnick M.S., Whittaker D.M. and Roberts J.S., *Parametric oscillation in a vertical*

- microcavity: A polariton condensate or micro-optical parametric oscillation*, Phys. Rev. B, 62, R16248 (2000)
- [65] Carusotto I. and Ciuti, C., *Spontaneous microcavity-polariton coherence across the parametric threshold: Quantum Monte Carlo studies* Phys. Rev. B 72, 125335 (2005)
- [66] Skolnick, M.S., et al., *Spatial properties and coherence of the high density phase in the microcavity optical parametric oscillator*, Phys. Stat. Sol. b, 243, no. 14, 3741-3753 (2006)
- [67] Krizhanovskii, D.N., et al., *Dominant Effect of Polariton-Polariton Interactions on the Coherence of the Microcavity Optical Parametric Oscillator*, Phys. Rev. Lett., 97, 097402 (2006)
- [68] Krizhanovskii, D.N., et al., *Self-organization of multiple polariton-polariton scattering in semiconductor microcavities*, Phys. Rev. B, 77, 115336 (2008)
- [69] Baas, A., Karr, J.Ph., Eleuch, H., Giacobino, E., *Optical bistability in semiconductor microcavities*, Phys. Rev. A, 69, 023809 (2004)
- [70] Keeling, J. and Berloff, N.G., *Exciton-polariton condensation*, Contemporary Physics, 52, 131-151 (2011)
- [71] Kapitza, P., Allen, J.F., Misener, A.D., *Going with the flow - superfluidity observed*, Nature, 141, 74-74 (1938)
- [72] Allen, J.F., Misner, A.D., *Flow of liquid Helium II*, Nature, 141, 75 (1938)
- [73] Landau, L., *Theory of the superfluidity of Helium II*, Phys. Rev. B, 60, 356 (1941)
- [74] Wouters, M., Carusotto, I., *Excitations in a nonequilibrium Bose-Einstein condensate of exciton polaritons*, Phys. Rev. Lett., 99, 140402 (2007)
- [75] Utsunomiya, S., et al., *Observation of Bogoliubov excitations in exciton-polariton condensates*, Nature Phys., 4, 700 (2008)

- [76] Krizhanovskii, D.N., et al., *Effect of interactions on vortices in a nonequilibrium polariton condensate*, Phys. Rev. Lett., 104, 126402 (2010)
- [77] Whittaker, D.M., *Vortices in the microcavity optical parametric oscillator*, Superlattices Microstruct., 41, 297 (2007)
- [78] Guda, K., et al., *Spontaneous vortices in optically shaped potential profiles in semiconductor microcavities*, Phys. Rev., B, 87, 081209 (R), (2013)
- [79] Sich, M., et al. *Observation of bright polariton solitons in a semiconductor microcavity*, Nature Photonics, 6, 50-55 (2011)
- [80] Amiri I.S. and Afroozeh A., *Ring Resonator Systems to Perform Optical Communication Enhancement Using Soliton*, Springer (2014)
- [81] Pigeon, S., Carusotto, I., Ciuti, C., *Hydrodynamic nucleation of vortices and solitons in a resonantly excited polariton superfluid*, Phys. Rev. B, 83, 144513 (2011)
- [82] Tanese, D., et al., *Polariton condensation in solitonic gap states in a one-dimensional periodic potential*, Nature Communications, 4, 1749 (2013)
- [83] Cerda-Mendez, E.A, et al., *Exciton-Polariton Gap Solitons in Two-Dimensional Lattices*, Phys. Rev. Lett., 111, 146401 (2013)
- [84] Balili, R., et al., *Role of the stress trap in the polariton quasiequilibrium condensation in GaAs microcavities*, Phys. Rev. B, 79, 075319 (2009)
- [85] Balili, R., et al., *Bose-Einstein Condensation of Microcavity Polaritons in a Trap*, Science, 316, 1007 (2007)
- [86] de Lima, M.M., Jr., et al., *Phonon-Induced polariton superlattices*, Phys. Rev. Lett., 97, 045501 (2006)
- [87] Cerda-Mendez, E.A., et al., *Polariton condensation in dynamic acoustic lattices*, Phys. Rev. Lett., 105, 116402 (2010)

- [88] Kim, N.Y., et al., *GaAs Microcavity Exciton-Polaritons in a Trap*, Phys. Stat. Sol. B, 245, 6, 1076-1080 (2008)
- [89] Lai, C.W., et al. *Coherent zero-state and π -state in an exciton-polariton condensate array*, Nature, 450, 529(2007)
- [90] Kim, N.Y., et al., *Dynamical d-wave condensation of exciton-polaritons in a two-dimensional square-lattice potential*, Nature Physics, 7, 681 (2011)
- [91] El Daif, O., et al., *Polariton quantum boxes in semiconductor microcavities*, Appl. Phys. Lett., 88, 061105 (2006)
- [92] Indrissi Kaitouni, R., et al., *Engineering the spatial confinement of exciton polaritons in semiconductors*, Phys. Rev. B, 74, 155311 (2006)
- [93] Kuther, A., et al., *Confined optical modes in photonic wires*, Phys. Rev. B, 58, 15744 (1998)
- [94] Dasbach, G., et al., *Tailoring the polariton dispersion by optical confinement: Access to a manifold of elastic polariton pair scattering channels*, Phys. Rev. B, 66, 201201 R (2002)
- [95] Bloch, J., et al., *Strong-coupling regime in pillar semiconductor microcavities*, Superlattices and Microstructures, 22, 371 (2007)
- [96] Bayer, M., *Optical modes in photonic molecules*, Phys. Rev. Lett., 81, 2582 (1998)
- [97] Bajoni, D., *Polariton laser using single micropillar GaAs-GaAlAs semiconductor cavities*, Phys. Rev. Lett., 100, 047401 (2008)
- [98] Galbiati, M., *Polariton condensation in photonic molecules*, Phys. Rev. Lett., 108, 126403 (2012)
- [99] Wertz, E., et al., *Spontaneous formation and optical manipulation of extended polariton condensates*, Nature Physics, 6, 860-864 (2010)

- [100] Ferrier, L., et al., *Interactions in confined polariton condensates*, Phys. Rev. Lett., 106, 126401 (2011)
- [101] Panish, M.B., *A thermodynamic evaluation of the simple solution treatment of the Ga-P, and Ga-As systems*, J. Crystal Growth, 27, 6-20 (1974)
- [102] Sturm, C., Tanese, D., et al., *All-optical phase modulation in a cavity-polariton Mach-Zehnder interferometer*, Nature Communications, 5, 3278 (2014)
- [103] Nguyen, H.S, et al., *Realization of a double-barrier resonant tunneling diode for cavity polaritons*, Phys. Rev. Lett., 110, 236601 (2013)
- [104] Adachi, S. *Properties of Aluminium Gallium Arsenide*, INSPEC, 1993
- [105] author: Ben Mills, http://en.wikipedia.org/wiki/Gallium_arsenide, version from 21 02 2014
- [106] author: Ben Mills, http://en.wikipedia.org/wiki/Aluminium_arsenide, version from 21 02 2014
- [107] author: Ben Mills, http://en.wikipedia.org/wiki/Aluminium_gallium_arsenide, version from 21 02 2014
- [108] Adachi, S., *GaAs, AlAs, and $Al_xGa_{1-x}As$: Material parameters for use in research and device applications*, J. Appl. Phys., Vol. 58, No.3 (1985)
- [109] Rockett, A., *The Materials Science of Semiconductors*, Springer, 2007
- [110] Narayan, J., Sharan, S., *Mechanism of formation of 60° and 90° misfit dislocations in semiconductor heterostructures*, Materials Science and Engineering, B IO 261-267 (1991)
- [111] Hull, R., Bean, *Nucleation of misfit dislocations in strained-layer epitaxy in the Ge_xSi_{1-x}/Si system*, J. Vac. Sci. Technol. A, 7 2580 (1989)
- [112] Frank, F. C., van der Merwe, J. H., *One-dimensional dislocations*, Pro-

- ceedings of the Royal Society of London. Series A, Mathematical and Physical Sciences, Vol. 198, No. 1053., pp. 205-216, (1949)
- [113] Matthews, J.W., Blakeslee, A.E., *Defectts in epitaxial multilayers*, Journal of Crystal Growth, 27, 118-125 (1974)
- [114] Krieger, M. and Sigg, H. and Herres, N. and Bachem, K. and Köhler, K., *Elastic constants and Poisson ratio in the system AlAs-GaAs*, Applied Physics Letters, 66, 682-684 (1995)
- [115] Andrews, A. M. and LeSar, R. and Kerner, M. A. and Speck, J. S. and Romanov, A. E. and Kolesnikova, A. L. and Bobeth, M. and Pompe, W., *Modeling crosshatch surface morphology in growing mismatched layers. Part II: Periodic boundary conditions and dislocation groups*, Journal of Applied Physics, 95, 6032-6047 (2004)
- [116] Tsao, J.Y., *Materials Fundamentals of Molecular Beam Epitaxy*, Academic Press, New York (1993)
- [117] People, R., Bean, J.C., *Calculation of critical layer thickness versus lattice mismatch for Ge_xSi_{1-x}/Si strained-layer heterostructures*, Applied Physics Letters, 47, 322 (1985)
- [118] Houdre, R., et al., *Measurement of cavity-polariton dispersion curve from angle-resolved photoluminescence experiments*, Phys. Rev. Lett., Vol. 73, No. 15 (1994)
- [119] Weisbuch, C., Dingle, R., Gossard, A.C., Wiegmann, W., *Optical characterization of interface disorder in GaAs - $Ga_{1-x}Al_xAs$ multi-quantum well structures*, Solid State Commun., 38, 709-712 (1981)
- [120] Schultheis, L., et al., *Optical dephasing of homogeneously broadened two-dimensional exciton transitions in GaAs quantum wells*, Phys. Rev. B, 34, 12, (1986)
- [121] Khazanova, S.V., Vasilevskiy, M.I., *Modelling of the composition segrega-*

- tion effect during epitaxial growth of InGaAs quantum well heterostructures*, Semicond. Sci. Technol., 35, 085008 (2010)
- [122] Massies, J., et al., *Experimental evidence of difference in surface and bulk compositions of $Al_xGa_{1-x}As$, $Al_xIn_{1-x}As$ and $Ga_xIn_{1-x}As$ epitaxial layers grown by molecular beam epitaxy.*, Journal of Crystal Growth, 80, 307 (1987)
- [123] Whittaker, D.M., *What determines inhomogeneous linewidths in semiconductor microcavities?*, Phys. Rev. Lett., 80, 4791 (1998)
- [124] Langebin, W., Hvam, J.M., *Elastic scattering dynamics of cavity polaritons: evidence for time-energy uncertainty and polariton localization*, Phys. Rev. Lett., 88, 047401 (2002)
- [125] Freixanet, T., Sermage, B., Bloch, J., Marzin, J.Y., Planel, R., *Annular resonant Rayleigh scattering in the picosecond dynamics of cavity polaritons*, Phys. Rev. B, 60, R8509 (1999)
- [126] Savona, V., Piermaroccho, C., Quattropani, A., Tassone, F., Schwendimann, P., *Microscopic theory of motional narrowing of microcavity polaritons in a disordered potential.*, Phys. Rev. Lett., 78, 4470 (1997)
- [127] Litinskaia, M., La Rocca, G.C., Agranovich, V.M, *Inhomogeneous broadening of polaritons in high-quality microcavities and weak localization*, Phys. Rev. B., 64, 165316 (2001)
- [128] Sanvitto, D., Krizhanovskii, D.N., Whittaker, D.M., Ceccarelli, S., Skolnick, M.S., *Spatial structure and stability of the macroscopically occupied polariton state in the microcavity optical parametric oscillator*, Phys. Rev. B, 73,241308(R) (2006)
- [129] Gurioli, M., Bogani, F., Cavigli, L., Gibbs, H., Khitrova, G., Wiersma, D.S., *Weak localization of light in a disordered microcavity*, Phys. Rev. Lett., 94, 183901 (2005)

- [130] Abbarchi, M., et al., *Discretized disorder in planar semiconductor microcavities: Mosaicity effect on resonant Rayleigh scattering and optical parametric oscillation*, Phys. Rev. B, 85, 045316 (2012)
- [131] Malpuech, G., Solnyshkov, D., *Chapter 9: Disorder effects on exciton-polariton condensates*, Exciton Polaritons in Microcavities – New Frontiers, Springer (2012)
- [132] Shchegrov, A.V., Bloch, J., Birkedal, D., Shah, J., *Theory of resonant Rayleigh scattering from semiconductor microcavities: Signatures of disorder*, Phys. Rev. Lett., 84, 3478 (2000)
- [133] Marchetti, F.M., Szymańska, M.H., Tejedor, C., Whittaker, D.M., *Spontaneous and triggered vortices in polariton optical-parametric-oscillator superfluids*, Phys. Rev. Lett., 105, 063902 (2010)
- [134] Krizhanovskii, D.N., Whittaker, D.M., Skolnick, M.S., Lagoudakis, K.G., Wouters, M., *Chapter 5: Coexisting polariton condensates and their temporal coherence in semiconductor microcavities*, Exciton Polaritons in Microcavities – New Frontiers, Springer (2012)
- [135] Kawada, H., Shirayone, S., Takahashi, K., *Reduction of surface defects in GaAs layers grown by MBE*, J. Cryst. Growth 128, 550 (1993)
- [136] Zajac, J.M., Langbein, W., *Polariton states bound to defects in GaAs/AlAs planar microcavities*, Phys. Rev. B, 85, 165309 (2012)
- [137] Zajac, J.M., Langbein, W., *Structure and zero-dimensional polariton spectrum of natural defects in GaAs/AlAs microcavities*, Phys. Rev. B, 86, 195401 (2012)
- [138] Mazuelas, A., Hey, R., Jenichen, B., Grahn, H.T., *Alternating Be and C doping for strain compensated GaAs/AlAs distributed Bragg reflectors*, Appl. Phys. Lett., 70, 2088 (1997)
- [139] Zajac, J.M., Clarke, E., Langebin, W., *Suppression of cross-hatched po-*

- lariton disorder in GaAs/AlAs microcavities by strain compensation.*, Appl. Phys. Lett., 101, 041114 (2012)
- [140] Ochalski, T.J., et al., *Photoreflectance studies of InGaAs/GaAs/AlGaAs single quantum well laser structures*, Acta Physica Polonica A, 94, 463 (1998)
- [141] Kavokin, A.V., Baumberg, J.J., Malpuech, G. and Laussy, F.P., *Microcavities*, Oxford University Press (2002)
- [142] Vladimirova, M. et al., *Polariton-polariton interaction constants in microcavities.*, Phys. Rev. B 82, 075301 (2010)
- [143] I. A. Shelykh et al, *Polariton polarization-sensitive phenomena in planar semiconductor microcavities.*, Semicond. Sci. Techol 25, 013001 (2010).
- [144] Rubo, Y.G., Kavokin, A.V. and Shelykh, I.A. *Suppression of superfluidity of excitonpolaritons by magnetic field*, Physics Letters A, 358, 227–230 (2006)
- [145] A. I. Tartakovskii, D. N. Krizhanovskii, and V. D. Kulakovskii, *Polariton-polariton scattering in semiconductor microcavities: Distinctive features and similarities to the three-dimensional case*, Phys. Rev. B 62, R13 298 (2000).
- [146] Wouters, M., *Synchronized and desynchronized phases of coupled nonequilibrium exciton-polariton condensates*, Phys. Rev. B, 77, 121302(R) (2008)
- [147] F. P. Laussy et al., Phys. Rev. B 73, 035315 (2006)
- [148] D. Sarkar, S.S. Gavrilov, M. Sich, J. H. Quilter, R.A. Bradley, N.A. Gippius, K. Guda, V. D. Kulakovskii, M. S. Skolnick, and D. N. Krizhanovskii, *Polarization Bistability and Resultant Spin Rings in Semiconductor Microcavities* Phys. Rev. Lett. 105, 216402 (2010),
- [149] D. N. Krizhanovskii et al., *Impact of exciton localization on the optical non-linearities of cavity polaritons*, Solid State Commun. 119, 435 (2001)
- [150] Bloch, F., Z. Phys. 52, 55 (1928)

- [151] Zener, C., *A Theory of the Electrical Breakdown of Solid Dielectrics.*, Proc. R. Soc. Lond. A145, 523-529 (1934)
- [152] Feldman, J. et al., *Optical investigation of Bloch oscillations in a semiconductor superlattice*, Phys. Rev. B 46,11 (1992)
- [153] Leo, K. et al., *Observation of Bloch oscillations in a semiconductor superlattice*, Sol. State Commun., 84, 943 (1992)
- [154] Pertsch, T. et al., *Optical Bloch oscillations in temperature tuned waveguide arrays*, Phys. Rev. Lett., 83, 4752 (1999)
- [155] Morandotti, R. et al., *Experimental observation of linear and nonlinear Bloch oscillations*, Phys. Rev. Lett., 83, 4756 (1999)
- [156] G. Malpuech, A. Kavokin, G. Panzarini, and A. Di Carlo, *Theory of photon Bloch oscillations in photonic crystals*, Phys. Rev. B 63, 035108 (2001)
- [157] M. Ben Dahan, E. Peik, J. Reichel, Y. Castin, and C. Salomon, *Bloch Oscillations of Atoms in an Optical Potential*, Phys. Rev. Lett. 76, 4508 (1996)
- [158] D. I. Choi and, Q. Niu, *Bose-Einstein Condensates in an Optical Lattice*, Phys. Rev. Lett. 82, 2022 (1999)
- [159] Hartmann, T., Keck, F., Korsch, H.J., Mossmann, S., *Dynamics of Bloch oscillations*, New Journal of Physics, 6, 2 (2004)
- [160] Wannier, G.H., *Wave functions and effective Hamiltonian for Bloch electrons in an electric field*, Phys. Rev., 117, 432 (1960) and comments
- [161] Zak, J., *Stark ladder in solids?*, Phys. Rev. Lett., 20, 1477 (1968)
- [162] Rabinovitch, A., Zak, J., *Does a Bloch electron in a constant electric field oscillate?*, Phys. Rev., 40 A, 189 (1972)

- [163] Krieger, J.B., Iafrate G.J., *Time evolution of Bloch electrons in a homogeneous electric field*, Phys. Rev. B., 33, 5494 (1986)
- [164] Emin, D., Hart, C.F., *Existence of Wannier-Stark localization*, Phys. Rev. B, 36, 7353 (1987) and comments
- [165] Zhao, X.G., *Bloch electron in a uniform electric field*, Phys. Rev. B., 46, 1305 (1992)
- [166] Bouchard, A.M., Luban, M., *Bloch oscillations and other dynamical phenomena of electrons in semiconductor superlattices*, Phys. Rev. B., 52, 5105 (1995)
- [167] Voisin, P., Bleuse, J., Bouche, C., Gaillard, S., Alibert, C., Regreny, A., *Observation of the Wannier-Stark quantization in a semiconductor superlattice*, Phys. Rev. Lett., 61, 1639 (1988)
- [168] Mendez, E.E., Agullo-Rueda, F., Hong, J.M., *Stark localization in GaAs-GaAlAs superlattices under an electric field*, Phys. Rev. Lett., 60, 2426 (1988)
- [169] Zener, C., *A theory of the electrical breakdown of solid dielectrics*, Proc. R. Soc. Lond. A, 145, 523 (1934)
- [170] Avron, J.E., Zak, J., Grossmann, A., Gunther, L., *Instability of the continuous spectrum: The Nband Stark ladder*, J. Math. Phys., 18, 918 (1977)
- [171] Maryam, W., Akimov, A.V., Campion, R.P, Kent, A.J, *Dynamics of a vertical cavity quantum cascade phonon laser structure*, Nature Comms., 4, 2184 (2013)
- [172] Anderson, B.P., Kasevich, M.A., *Macroscopic quantum interference from atomic tunnel arrays*, Science, 282, 1686 (1998)
- [173] Ferrari, G., Poli, N., Sorrentino, F., Tino, G.M., *Long-lived Bloch oscillations with bosonic Sr atoms and application to gravity measurement at the micrometer scale*, Phys. Rev. Lett., 97, 060402 (2006)

- [174] Dragoman, D., Dragoman, M., *Quantum-classical analogies*, Springer, p.43 (2004)
- [175] Peschel, U., Pertsch, T., Lederer, F., *Optical Bloch oscillations in waveguide arrays*, Opt. Lett. 1;23(21), 1701-3 (1998)
- [176] Sapienza R, et al., *Optical analogue of electronic Bloch oscillations*, Phys. Rev. Lett., 91, 263902 (2003)
- [177] Lenz, G., Talanina, I., Martijn de Sterke, C., *Bloch oscillations in an array of curved optical waveguides*, Phys. Rev. Lett., 83, 963 (1999)
- [178] Flayac, H., Solnyshkov, D.D., Malpuech, G., *Bloch oscillations of an exciton-polariton Bose-Einstein condensate*, Phys. Rev. B, 83, 045412 (2011)
- [179] Gorbach, A.V., Skryabin, D.V., *Parametric instabilities of microcavity polaritons in a periodic potential*, Phys. Rev. B, 82, 125313 (2010)
- [180] Byrnes, T., Recher, P., Yamamoto, Y., *Mott transitions of exciton polaritons and indirect excitons in a periodic potential*, Phys. Rev. B, 81, 205312 (2010)
- [181] Wouters, M., Carusotto, I., Ciuti, C., *Spatial and spectral shape of inhomogeneous nonequilibrium exciton-polariton condensates*, Phys. Rev. B, 77, 115340 (2008)
- [182] Wertz, E., et al., *Propagation and amplification dynamics of 1D polariton condensates*, Phys. Rev. Lett., 109, 216404 (2012)